
Terahertz spectroscopy of graphene and graphene nanostructures

Dissertation
zur Erlangung des Grades
“Doktor der Naturwissenschaften”
am Fachbereich Physik, Mathematik und Informatik
der Johannes Gutenberg–Universität
in Mainz

von:
Ivan Ivanov
geboren in Tschechow
Mainz, 2018



MAX-PLANCK-GESELLSCHAFT



JOHANNES GUTENBERG
UNIVERSITÄT MAINZ

1. Berichterstatter: Prof. Dr. Dmitry Turchinovich
 2. Berichterstatter: Prof. Dr. Peter G. J. van Dongen
- Datum der mündlichen Prüfung: 16.07.2019

Ivan Ivanov

Terahertz spectroscopy of graphene and graphene nanostructures

Max Plank Institute for Polymer Research

Ultrafast Dynamics and THz Spectroscopy Group. Group leader – Dmitry Turchinovich

Molecular Spectroscopy Department. Director – Mischa Bonn

Ackermannweg 10

55128, Mainz

Abstract

At all times, innovative materials have helped to expand the boundaries of technologies. Given the never-ending technological progress, there is an undisputable need for new perspective materials. One of these promising materials is graphene. Its unique electronic properties have given hope for its application in the electronics, optoelectronics and other technologies. Moreover, the advances in the production methods of graphene have introduced others promising materials, such as graphene nanoribbons. In this work, we study the carrier conduction in graphene and graphene nanostructures as perspective materials for the next generation of electronics. To this end, we employ THz time domain spectroscopy. Because of the low photon energy of THz radiation, it is particularly sensitive to the electronic conductivity, which is dominated by charge carriers with low excitation energies. In addition, THz time domain spectroscopy allows measuring conductivity in broad frequency range and in a contact-free manner.

In the first part, we study ultrafast carrier dynamics in a single layer graphene, produced by chemical vapor deposition (CVD). We show that the doped graphene excited with the high-field THz pulse or with the optical pulse exhibit the reduction of its conductivity in THz range. Using a simple thermodynamic picture, we can describe qualitatively and quantitatively the THz conductivity of graphene in this excited state. According to this picture, the energy of the THz field or an optical pulse converts efficiently and quasi-instantaneously into the internal energy of the entire electron population, thus leading to the elevation of its temperature. In this state, carriers have reduced intra-band conductivity due to the decreased chemical potential, which is a result of the conservation of energy and particle number.

In the second part, we have investigated ultrafast charge carrier dynamics in graphene with periodic folds. In CVD-grown graphene, folds occur randomly. In our samples, these folds have been introduced in the ordered, periodic manner using the novel transfer-printing method - GraFold – developed by the group of Prof. G. S. Duesberg in Trinity College, Dublin. We have not observed any tangible change in the background conductivity of the sample. Although, the studies in the optically excited state have demonstrated that the negative photoconductivity in the direction perpendicular to folds is in ca. 1.5 times less than in the

direction parallel to them. One cannot simply explain this initial result just by the filling factor of the folds, which is less than 5%. A possible explanation could be that in photo-excited state this sample exhibit the anisotropic potential landscape that leads to the observed anisotropy of the photoconductivity.

In the third part, we have studied the conductivity in the bottom-up synthesized graphene nanoribbons (GNRs). Using THz studies and transport calculations, we have shown that the edge structure of GNRs play a crucial role in their conductive properties. In particular, we have demonstrated that in GNRs with similar optical properties and band structures, but different edge structures, display different scattering times of the conductive carriers. Moreover, simple alkyl chains, which are usually decorating edges of chemically grown GNRs, also show minor influence on the carrier transport.

Contents

Abstract	v
Contents	vii
Abbreviations	ix
1 Introduction	1
2 Theoretical background	5
2.1 Fundamentals of graphene	5
2.2 Basics of graphene nanoribbons	12
2.3 Conductivity models	16
2.3.1 The Drude model	16
2.3.2 Semi-classical theory of the conductivity	19
2.3.3 The conductivity of quasi-free electrons – Drude-Smith model.....	22
3 Terahertz time-domain spectroscopy	25
3.1 Terahertz generation and detection.....	27
3.1.1 Optical rectification	27
3.1.2 Free-space electro-optic sampling	32
3.2 Experimental setup	36
3.2.1 Terahertz time-domain spectroscopy.....	38
3.2.2 Optical-pump terahertz-probe spectroscopy.....	43
4 Terahertz spectroscopy of Graphene	51
4.1 Terahertz conductivity of graphene	51
4.2 Nonlinear terahertz conductivity of graphene — Thermodynamic model	54
4.3 Photoconductivity of graphene — thermodynamic model	60
4.4 Conclusions.....	68
4.A Appendix: Numerical propagation of terahertz pulse through graphene	68
5 Terahertz spectroscopy of mesostructured graphene – GraFold printing	73
5.1 Description of the sample — GraFold printing	73
5.2 Terahertz spectroscopy of GraFold samples	77
5.3 Conclusions.....	81
6 Terahertz spectroscopy of graphene nanoribbons	83
6.1 Graphene nanoribbons samples	84
6.2 Terahertz conductivity of graphene nanoribbons.....	86
6.3 Electronic structure and transport calculations	92
6.3 Conclusions.....	99

7 Summary and outlook.....	101
Bibliography	103
Acknowledgments.....	119
Publications List	121
Curriculum Vitae	123

Abbreviations

1D	one dimensional
2D	two dimensional
3D	three dimensional
AC	alternating current
AFM	atomic force microscope
AGNR	armchair graphene nanoribbon
ARPES	angle-resolved photoemission spectroscopy
BBO	barium borate
BIBO	bismuth borate
BZ	Brillouin zone
CB	conduction band
CBM	conduction band minima
CGNR	cove graphene nanoribbons
CNT	carbon nanotubes
CVD	chemical vapor deposition
DC	direct current
DFT	density functional theory
DP	deformation potential
DS	Drude-Smith
EO	electro-optic
FTIR	Fourier-transform infrared spectroscopy
FWHM	the full width at half maximum
HAADF	high-angle annular dark-field imaging
HOMO	highest occupied molecular orbital
IR	infrared
LUMO	lowest unoccupied molecular orbital
OD	optical density
OPTP	optical pump terahertz probe
PDMS	polydimethylsiloxane
SEM	scanning electron microscopy

STEM	scanning transmission electron microscopy
TCB	trichlorobenzene
TDS	time domain spectroscopy
TERS	tip-enhanced Raman spectroscopy
TRTS	time resolved transient spectroscopy
UV	ultraviolet
VB	valence band
VBM	valence band maxima
ZGNR	zigzag graphene nanoribbon

Chapter 1

Introduction

The understanding of the dynamics of charge carriers in materials is vital for the fundamental knowledge as well as for technological applications. The way of how electrons lose their energy and momentum to their surroundings crucially defines the performance of for example electronics and solar cells [1].

The preparation of the first graphene film in 2004 by Novoselov and coworkers [2] has foreshadowed the launch of the new highly growing branch of the science of 2D materials [3]–[5]. Resulting from the linear band dispersion, the unique electron transport and optical properties of graphene [6], [7] have given hope for its application in a post-silicon generation of electronics [8] and photonics [9]. It has also been shown that graphene is a perspective material for THz physics that can act as an efficient frequency up-converter in the THz range [10], [11].

Since graphene is 2D material, folds or wrinkles can naturally form in this material. It is especially relevant in the large-area graphene samples that are obtainable by chemical synthesis. The group of Professor Georg Duesberg in Trinity College Dublin has invented the transfer-printing approach of controllable folding in graphene in a patterned manner – so-called GraFold. It is of great importance to study the impact of such patterned formations on the conductive properties of graphene since such a novel approach as GraFold potentially paves the way towards the printable graphene circuits.

In the context of recent advances in the chemical synthesis of low dimensional graphene structures [12], nanometer-sized graphene ribbons come into focus. Given their 1D nature and the large bandgap, resulting from the quantum confinement, graphene nanoribbons are seen as promising materials for the future channel materials in field effect transistors. The bottom-up approach provides nanoribbons with controllable widths, edge structures, and

functionalization. We also study the impact of the edge structure on the conductive properties of graphene nanoribbons in this work.

In view of their technological potential for future electronics, the dynamics of charge carriers in graphene, folded graphene and graphene nanoribbons are studied in this work. The tool of choice that we have used to this end is the THz time-domain spectroscopy that employs short THz pulses to probe the conductive charges in these materials. Due to the very low photon energy of THz radiation, i.e., the electromagnetic wave of 1 THz frequency corresponds to the photon energy of 4.1 meV, it can only induce excitations with low transitions energies. Therefore, THz radiation is particularly sensitive to the electronic conductivity as it is dominated by the charge carriers with low excitation energies, for instance, intraband transitions of conductive electrons and holes in the region near the Fermi level. Another advantage of using THz spectroscopy is the fact that short probing THz pulses comprise a bandwidth of frequencies (in this work it is usually 0.3 – 2.5 THz), thus allowing to retrieve conductive properties in a broad frequency range. In the perspective of the pulsed nature of the THz spectrometry, it is also possible to study the conductivity dynamics upon the system has been perturbed, for instance, by an optical pulse.

Moreover, there are other interesting excitations corresponding to the variety of ultrafast phenomena taking place in condensed matter that also lie in the THz frequency range. For instance, molecular vibrations and phonons of the lattice [13], as well as the spin oscillations [14], can interact effectively with electromagnetic waves of THz frequencies.

This thesis is organized as follows:

In Chapter 2, the basic physics of graphene and graphene nanoribbons is presented. Also, we describe some conductivity models that we used in this work.

In Chapter 3, we will describe the basic principles behind the THz generation and detection. The layout of the THz spectrometer will also be introduced together with types of the experiments one can convey on this setup. The mathematical formulas for the retrieving optical properties from the obtainable on this spectrometer signals are also presented in this chapter.

In Chapter 4, we present experimental studies of the THz photo-physics in graphene. We will demonstrate that the carrier dynamics in graphene is governed by the thermodynamic state of the charge carrier system by introducing the thermodynamic model of conductivity in graphene.

Chapter 5 is dedicated to studies of the impact of the periodic folding in graphene on its conductive properties. Given the 2D nature of graphene, folding is its inevitable ‘property’ that takes place naturally. Here we introduce the invented by the group of Prof. G. Duesberg from Trinity College Dublin approach for the controllable creation of folds in graphene – GraFold. We also show the THz conductivity studies of such samples.

In Chapter 6, we investigate the THz conductivities in graphene nanoribbons with different edge structures. We will try to answer how the edge structure influences the conductive properties of graphene nanoribbons with resembling optical fingerprints.

Chapter 2

Theoretical background

The initial theoretical studies have predicted that graphene (and any 2D crystal) would be thermodynamically unstable [4]. In 2004, Konstantin Novoselov and Andre Geim obsoleted this common knowledge by the experimental discovery of graphene [2] and other free-standing 2D atomic crystals [3]. These works have demonstrated unique transport (high mobility) and optical properties (uniform optical absorption) of graphene that stems from its unique conical band structure. In this chapter, we review the fundamental electronic properties of graphene as well as graphene nanoribbons (GNRs). Also, we introduce the charge carrier transport models we encounter during this work.

2.1 Fundamentals of graphene

Here we summarize the lattice and electronic structure of graphene and some of its optoelectronic properties following refs. [14]–[17].

Graphene is a two-dimensional (2D) lattice of carbon atoms arranged in a hexagonal (honeycomb) structure, as shown in Figure 2.1a. The structure represents a triangular lattice with a basis of two atoms per unit cell. Alternatively, one can see it as composed of the two triangular sub-lattices, marked as *A* and *B*. The lattice primitive vectors can be written as (in the coordinate system shown in Figure 2.1a)

$$\vec{a}_1 = \frac{a}{2}(3, \sqrt{3}), \quad \vec{a}_2 = \frac{a}{2}(3, -\sqrt{3}) \quad (2.1)$$

where $a \approx 1.42 \text{ \AA}$ is the carbon-carbon distance. Using equation $\vec{b}_i \cdot \vec{a}_j = 2\pi\delta_{ij}$ one can find the reciprocal-lattice vectors to be:

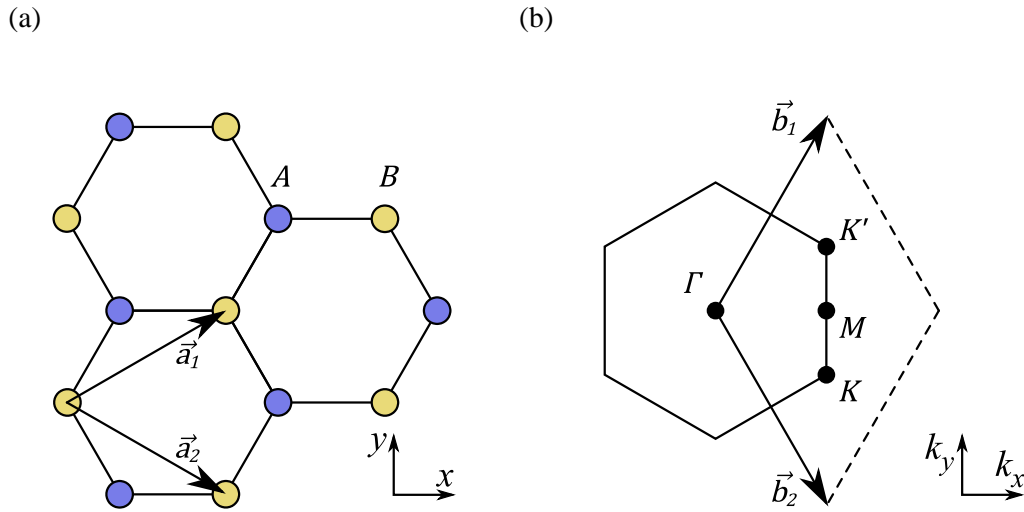


Figure 2.1: Honeycomb lattice (a) and its Brillouin zone (b). The lattice structure of graphene, made out of two interpenetrating triangular lattices (\vec{a}_1 and \vec{a}_2 are the lattice primitive vectors). The corresponding Brillouin zone shows similar honeycomb structure.

$$\vec{b}_1 = \frac{2\pi}{3a}(1, \sqrt{3}), \quad \vec{b}_2 = \frac{2\pi}{3a}(1, -\sqrt{3}) \quad (2.2)$$

The resulting reciprocal lattice of graphene is therefore also a honeycomb structure rotated by 90° relative to the real-space lattice. The Brillouin zone (BZ) of graphene is shown in Figure 2.1b.

The building blocks of graphene lattice - carbon atoms - have four valence electrons. Three of these electrons form sp^2 bonds between neighboring carbon atoms. The residual p_z orbital overlaps with p_z orbitals of the neighboring atoms forming a weak π -bonds with bonding (π) and anti-bonding (π^*) states. These states form the conduction and valence bands of the graphene by merging of p_z orbitals of all carbon atoms in the lattice. One carbon atom gives one electron to fill these bands. Thereby, intrinsic graphene has a fully occupied valence band and a completely empty conduction band [14]–[16] or in other words the Fermi level lies between these bands.

The electronic band structure of graphene was first calculated by Wallace in 1947 [18] within the tight-binding framework. The tight-binding Hamiltonian for electrons in graphene considering electron hopping to the nearest-neighbor atom (and with on-site energy set to zero) has the form

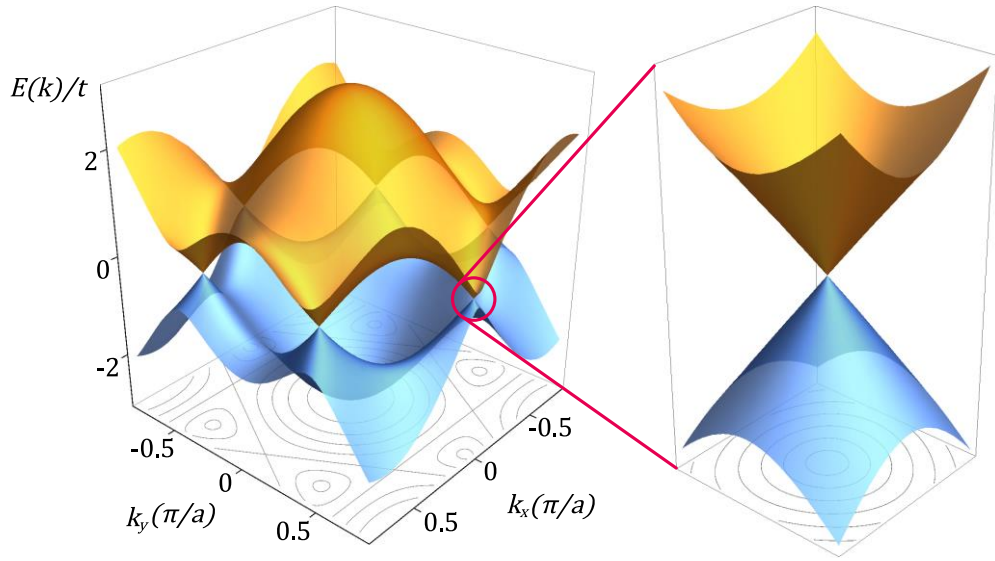


Figure 2.2: The electronic dispersion of the honeycomb lattice calculated within tight-binding approximation. (left) Energy spectrum (in units of t). (right) Zoom in of the energy bands close to one of the Dirac points. The valence and conduction band are shown in blue and yellow correspondingly. This graph is obtained by plotting Eq. (2.4) in Wolfram Mathematica 11.

$$\hat{H} = -t \sum_{i,j,\sigma} (a_{i,\sigma}^\dagger b_{j,\sigma} + h. c.) \quad (2.3)$$

where $a_{i,\sigma}$ ($a_{i,\sigma}^\dagger$) annihilates (creates) electron with spin σ ($\sigma = \uparrow, \downarrow$) on site i of sublattice A and $b_{j,\sigma}$ ($b_{j,\sigma}^\dagger$) annihilates (creates) electron on site j of sublattice B . The nearest-neighbor hopping energy t (hopping between different sublattices) amounts to ≈ 2.8 eV.

The energy bands derived from this Hamiltonian have the form [18]

$$\begin{aligned} \varepsilon_{\pm}(\vec{k}) &= \pm t \sqrt{3 + f(\vec{k})}, \\ f(\vec{k}) &= 2 \cos(\sqrt{3}k_y a) + 4 \cos\left(\frac{\sqrt{3}}{2}k_y a\right) \cos\left(\frac{3}{2}k_x a\right) \end{aligned} \quad (2.4)$$

where the plus sign applies to the upper (π^* or conduction) and the minus sign the lower (π or valence) band. It is clear that the dispersion is symmetric around zero energy. In Figure 2.2, we show the band structure of graphene given by (2.4). In the same figure, we also show a zoom-in of the band structure near the point where conduction and valence band touch each other. This is the so-called Dirac point that is located in the point K at the corner of the

graphene BZ. There are two physically inequivalent Dirac points in BZ (Figure 2.1b) and the following two vectors give their positions in the space of wave vectors:

$$\vec{K} = \frac{2\pi}{3a} \left(1, \frac{1}{\sqrt{3}}\right), \quad \vec{K}' = \frac{2\pi}{3a} \left(1, -\frac{1}{\sqrt{3}}\right) \quad (2.5)$$

Dirac points are of particular importance for the physics of graphene since the dispersion of electrons has a peculiar conical shape in the low energy limit near these points (zoom-in shown in Figure 2.2). The mathematical expression for this conical dispersion near Dirac points can be obtained by Taylor expansion of the full band structure (2.4) by substituting $\vec{k} = \vec{K} + \vec{q}$, with $|\vec{q}| \ll |\vec{K}|$ [18], this results in:

$$\mathcal{E}_{\pm}(\vec{q}) = \pm \hbar v_g |\vec{q}| + O[(q/K)^2], \quad (2.6)$$

where \vec{q} is the wave vector measured relatively to the Dirac point and v_g is the group velocity of the electron, given by $v_g = 3|t|a/(2\hbar)$, with a value of $\approx 1 \times 10^6$ m/s. Since one gets the same expression for the energy of electrons near K' , then one can say that electrons near Dirac points are degenerate with the degeneracy of 2, this is so called valley degeneracy. Subsequently, we will use simply \vec{k} to denote the wavevector measured relatively to the K (or K') point in graphene, unless it is stated otherwise.

The most striking difference between electron with the conical dispersion (2.6) and the free electron is that its group velocity does not depend on the energy or momentum (or rather quasi-momentum since we are speaking about electrons in the crystal lattice). Indeed, the dispersion law of a free electron is proportional to the square of its momentum: $\mathcal{E}(\vec{k}) = (\hbar k)^2/(2m)$, where m is the mass of electron. Thereby for free electrons, we have $v_g = \hbar k/m = \sqrt{2\mathcal{E}/m}$ and hence the group velocity changes substantially with energy. While in graphene, this value is constant and in the literature it usually referred to as Fermi velocity of graphene, i.e., $v_g \equiv v_{\mathcal{F}}$.

The dispersion relation also defines a density of states, and one can show that the density of states near Dirac points in graphene is a linear function of energy. Indeed, using the transition from the integration over the space of wavevectors to the integration over energies (for an arbitrary function $Q(\vec{k})$) one can derive the density of states for the electrons in the crystal. This transitions can be often found in the text books on solid state physics [19] and has the form:

$$\nu \int \frac{d\vec{k}}{(2\pi)^n} \mathcal{Q}(\vec{k}) = \int d\mathcal{E} g(\mathcal{E}) \mathcal{Q}(\vec{k}(\mathcal{E})), \quad (2.7)$$

here n is the dimensionality of the space, ν is the degeneracy of states and $g(\mathcal{E})$ is the density of states. For the conduction band in graphene near Dirac points, we write the integral in (2.7) as (we omit the function $\mathcal{Q}(\vec{k})$ to write it in the compact form):

$$\nu \int \frac{d\vec{k}}{(2\pi)^2} = \nu \int \frac{k dk}{2\pi} = \nu \int \frac{\mathcal{E}}{\hbar v_{\mathcal{F}}} d\left(\frac{\mathcal{E}}{\hbar v_{\mathcal{F}}}\right) = \int d\mathcal{E} \frac{\nu \mathcal{E}}{2\pi(\hbar v_{\mathcal{F}})^2} = \int d\mathcal{E} g(\mathcal{E}). \quad (2.8)$$

Thereby we get the expression for the density of states $g(\mathcal{E}) = \nu|\mathcal{E}|/2\pi(\hbar v_{\mathcal{F}})^2$, here ν is the degeneracy. In graphene, it equals 4 as a result of degeneracies of the spins and valleys. The absolute value of energy means that the same expression can be obtained for the negative energy, i.e., for the valence band. Thus, one finally writes the expression for the density of states near Dirac points in graphene:

$$g(\mathcal{E}) = 2|\mathcal{E}|/\pi(\hbar v_{\mathcal{F}})^2 \quad (2.9)$$

The dispersion (2.6) is akin to that of the ultra-relativistic massless particles like photons ($\mathcal{E} = pc \equiv \hbar kc$) with only one difference of the speed of light being equal to the Fermi velocity of graphene. A particle being ultra-relativistic implies that its energy comes mostly from its momentum (not the rest mass) or in the case of the massless particles exclusively due to it. Thereby, in the vicinity of K and K' points in wave vector space one can rewrite the tight-binding Hamiltonian in the low-energy approximation as Dirac Hamiltonian:

$$\hat{H}_{\mathcal{D}} = \hbar v_{\mathcal{F}} \begin{pmatrix} 0 & k_x - ik_y \\ k_x + ik_y & 0 \end{pmatrix} = \hbar v_{\mathcal{F}} \vec{\sigma} \cdot \vec{k} = v_{\mathcal{F}} \vec{\sigma} \cdot \vec{p} \quad (2.10)$$

where $\vec{\sigma}$ is a 2D vector of Pauli matrices. The eigenfunctions of this Hamiltonian in wave vector space read:

$$\psi_{h,e}(\vec{k}) = \frac{1}{\sqrt{2}} \begin{pmatrix} e^{i\theta_{\vec{k}}/2} \\ \pm e^{-i\theta_{\vec{k}}/2} \end{pmatrix} \quad (2.11)$$

where $\theta_{\vec{k}} = \arctan(k_y/k_x)$ is the polar angle of the vector \vec{k} . The minus (plus) stands for the state in the valence (conduction) band, i.e., hole (electron) state. The latter expression is for the states near the point K' , the expression for the states near the point K can be obtained by

complex conjugation of Eq. (2.11). The Dirac approximation shown above is valid for energies $|\mathcal{E}| \lesssim 0.5t \approx 1.4$ eV and thereby provides an excellent framework to describe transport and optical phenomena in graphene.

As an example, one can show using the expression of eigenstates (2.11) that graphene has a uniform inter-band optical conductivity, which has also been experimentally observed [6]. Following ref. [17], we introduce the optical light via the vector potential $\vec{A}(t) = \vec{A}e^{-i\omega t}$, i.e.

$$\vec{E}(t) = -\frac{1}{c}\frac{\partial\vec{A}}{\partial t} = \frac{i\omega}{c}\vec{A}. \quad (2.12)$$

Thus, the resulting Dirac Hamiltonian in the presence of an electric field of an incident light reads as

$$\hat{H} = v_F\vec{\sigma}\left(\vec{p} - \frac{e}{c}\vec{A}\right) = \hat{H}_D + \hat{V}, \quad (2.13)$$

where

$$\hat{V} = -\frac{v_F e}{2c}\vec{\sigma}\vec{A} = -\frac{iev_F}{2c}\vec{\sigma}\vec{E} \quad (2.14)$$

is the Hamiltonian of the electron-photon interaction. The factor 1/2 in the Eq. (2.14) is required since the common expression for the complex-valued oscillating electric field is

$$\vec{E}(t) = \text{Re}(\vec{E}e^{-i\omega t}) = \frac{1}{2}(\vec{E}e^{-i\omega t} + \vec{E}^*e^{i\omega t}) \quad (2.15)$$

and we take only the first term. This interaction induces transitions from the valence band into the conduction band for the states with the same wave vector \vec{k} . The matrix element describing this process is

$$\langle\psi_h(\vec{k})|\hat{V}|\psi_e(\vec{k})\rangle = \frac{ev_F}{2\omega}(E_y \cos\theta_{\vec{k}} \mp E_x \sin\theta_{\vec{k}}). \quad (2.16)$$

Here minus (plus) correspond to K (K') valley. The averaging of the square of this matrix element over possible momentum angles gives

$$|M|^2 = \overline{|\langle\psi_h(\vec{k})|\hat{V}|\psi_e(\vec{k})\rangle|^2} = \frac{e^2v_F^2}{8\omega^2}|\vec{E}|^2, \quad (2.17)$$

here we assume that the field lies in the plane of the graphene, i.e., the photon propagates perpendicular to the graphene plane. The probability of the absorption per unit of time can be obtained from the lowest order of perturbation theory [20]:

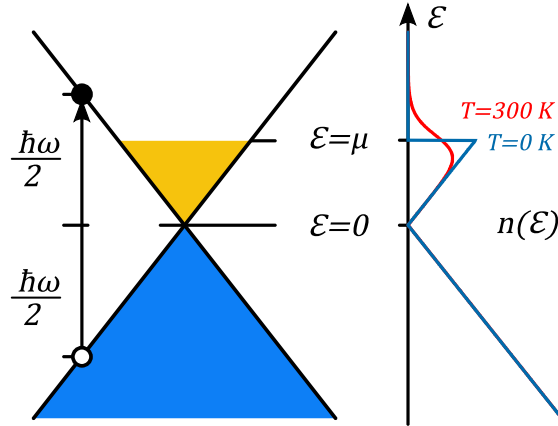


Figure 2.3: (left) The diagram showing the direct optical transition in graphene electronic structure near the Dirac point. (right) the occupancy of the states at absolute zero and at the room temperature.

$$P = \frac{2\pi}{\hbar} |M|^2 g\left(\frac{\hbar\omega}{2}\right), \quad (2.18)$$

here $g(\mathcal{E})$ is the density of states (2.9) taken at $\mathcal{E} = \hbar\omega/2$ which is obvious from the Figure 2.3. By substituting Eq. (2.9) and (2.17) in (2.18) one obtains

$$P = \frac{e^2}{4\hbar^2\omega} |\vec{E}|^2 \quad (2.19)$$

Thus, the absorption energy per unit of time reads:

$$W_a = P\hbar\omega = \frac{e^2}{4\hbar} |\vec{E}|^2 \quad (2.20)$$

The flux of the incident light is [21]

$$W_i = \frac{c}{4\pi} |\vec{E}|^2 \quad (2.21)$$

Finally, one can calculate the absorption coefficient in graphene:

$$\eta = \frac{W_a}{W_i} = \frac{\pi e^2}{\hbar c} \approx 2.3\% \quad (2.22)$$

The value of the optical absorption coefficient in graphene is frequency independent for photon energies within the boundaries of the Dirac approximation we used earlier, i.e., $\hbar\omega \lesssim t \approx 2.8$ eV. We note, that for the case of the non-intrinsic graphene with non-zero chemical potential the vertical optical transitions are forbidden for the photon energies lower than the double chemical potential ($\hbar\omega < 2\mu$), so-called Pauli blocked. That takes place due to either an occupied state in the conduction band or an empty state in the valence band.

Moreover, for sufficiently high finite temperatures, when the smearing of the Fermi edge is substantially broad in the band, the occupancy of the states has to be taken into account (see Figure 2.3). Nonetheless, graphene shows this uniform value for the broad range of photon energies in the visible frequency range at room temperatures, making this material extremely attractive for the photo-physics applications. In addition, one has to keep in mind that the absorption of 2.3% is provided by the one atom-thick material, which is a huge number.

In conclusion, we have reviewed the major electronic properties of graphene. The honeycomb symmetry of the graphene lattice provides the unique physics of the electrons in this material that can be approximated with the picture of massless Dirac fermions. The linear dispersion law and massless nature of the electrons in graphene are the most distinguishing features of it that leads to its unique optical and transport properties.

2.2 Basics of graphene nanoribbons

Due to the linear and gapless electronic band structure and the resulting unique electronic and optical properties of graphene, it has found a lot of applications in optoelectronics [9], [22]. Owing to its unique conical band structure, the charge carriers in graphene behave akin to massless particles giving rise to exceptionally high DC (direct current) charge carrier mobilities up to $350,000 \text{ cm}^2\text{V}^{-1}\text{s}^{-1}$ [23]. As it has been already mentioned in the previous section, the conical and gapless electronic band structure results in a broadband absorption spectrum [24], [25] making graphene advantageous for numerous applications. However, the absence of the gap in the band structure of graphene hinders its applications in such fields as, e.g., photovoltaics [26] or field effect transistors [27], [28], which could otherwise benefit from its transport properties.

On the other hand, nanometer-wide graphene structures, such as graphene nanoribbons (GNRs) [14] or carbon nanotubes (CNTs) [29], undergo bandgap opening as a result of quantum confinement of the electrons [14], [30].

Well-known CNTs have been under intense study after the work by Iijima that had been published in 1991 [31]. This work served as a take-off for the big branch of science and technology, and the worldwide scientific community recognized this work as the first discovery of CNTs. The curious historical remark is that the first pictures of CNTs were

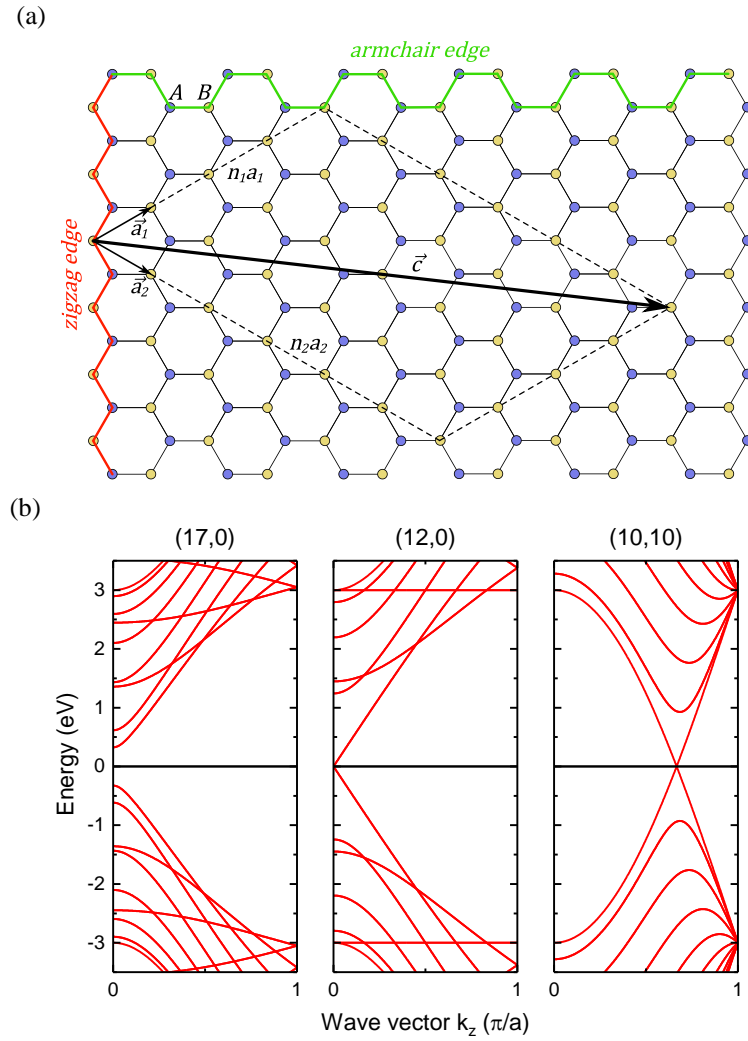


Figure 2.4: (a) A piece of a honeycomb lattice displaying possible armchair and zigzag edges together with the lattice vectors \vec{a}_1 , \vec{a}_2 and the chiral vector $\vec{c} = n_1\vec{a}_1 + n_2\vec{a}_2$ of the (4, 6) tube. (b) The band structures of (17, 0), (12, 0) and (10, 10) tubes. The first and the second CNTs are rolled up along \vec{a}_1 , i.e., alongside the zigzag edge, resulting in a semiconductor and a semimetal type of band structure respectively, with the band gap (and band crossing in the semimetal) located in the Γ point. The third CNT is rolled up along the armchair edge with the band crossing in $\vec{k}_z = 2\pi/3a$ and displays a semimetal type of band structure. The data have been obtained using an online tool located at <https://nanohub.org/resources/cntbands-ext> [165], [166]. The calculations use the tight binding approximation that accounts electron hopping only to the nearest neighbor atoms, with hopping energy of 3 eV and carbon-carbon spacing of 1.42Å.

published in 1952 (almost 40 years earlier than Iijima's work!), but it did not get international publicity as the work was published in a Soviet journal [32].

The CNT is essentially a rolled graphene sheet [4]. It is rolled up in such a way that graphene lattice vector $\vec{c} = n_1\vec{a}_1 + n_2\vec{a}_2$ becomes the circumference of the tube (Figure 2.4a). This

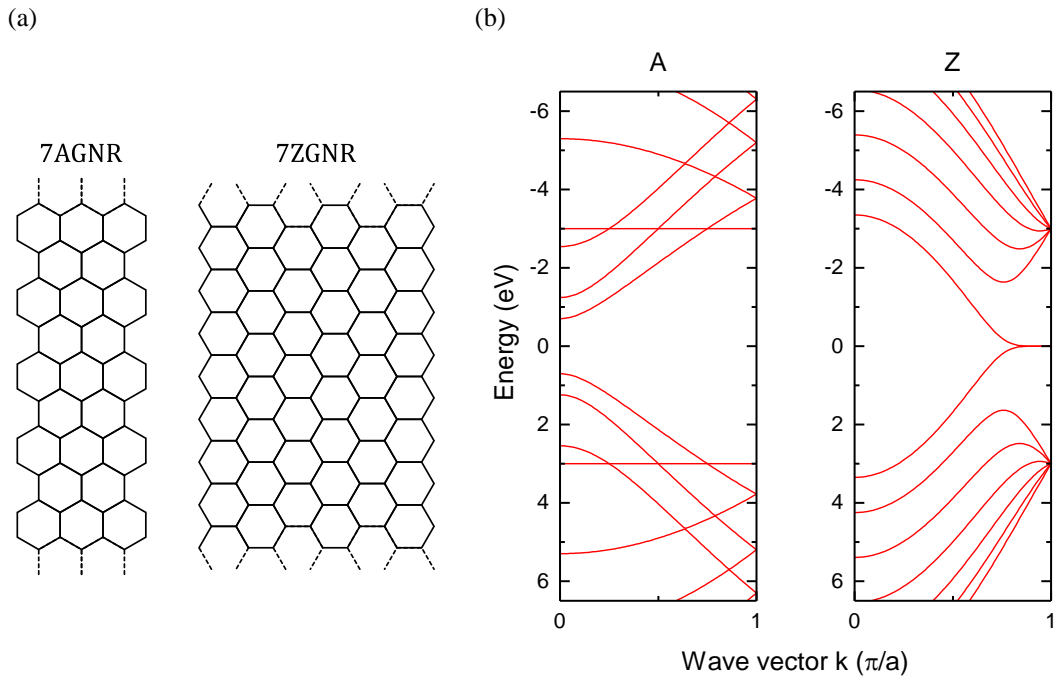


Figure 2.5: An example of two types of GNRs – armchair, and zigzag. (a) The lattice structure of 7AGNR and 7ZGNR. (b) Their corresponding band structures. The data were obtained using an online tool located at <https://nanohub.org/resources/cntbands-ext> [165]. The calculations use the tight binding approximation accounting only the nearest neighbor hopping (with energy of 3 eV) and carbon-carbon spacing of 1.42Å.

circumferential vector \vec{c} , which is usually denoted by the pair of integers (n_1, n_2) is called the chiral vector and uniquely defines a particular tube as well as its properties, e.g., the band structure [29] (Figure 2.4b).

GNRs are another example of the graphene nanostructures. Unlike CNTs, where circumferential vector or chirality defines the electronic properties, the width and especially the edge structure of the GNR play a crucial role in its electronic properties [33]. For instance, a GNR with a zigzag edge (Figure 2.4a, highlighted with red) or simply ZGNR (Figure 2.5a) has semi-metallic band structure (no bandgap) that persist until a relatively wide width of the GNR. Naturally, in the limit of infinitely wide ZGNR, it approaches the band structure of graphene – which is also a semi-metal. Importantly, the charge density is strongly localized near the zigzag edge due to a flat band (Figure 2.5b) that creates a peak in the density of states. This non-negligible edge state can survive even in GNRs with less developed zigzag edges [33]. This fact highlights the crucial and definitive role of the edge in GNRs electronic properties. On the other hand, a GNR with an armchair edge (Figure 2.4a, highlighted in green) or AGNR is semiconductor-like with a non-vanishing band gap in the dispersion (Figure 2.5b).

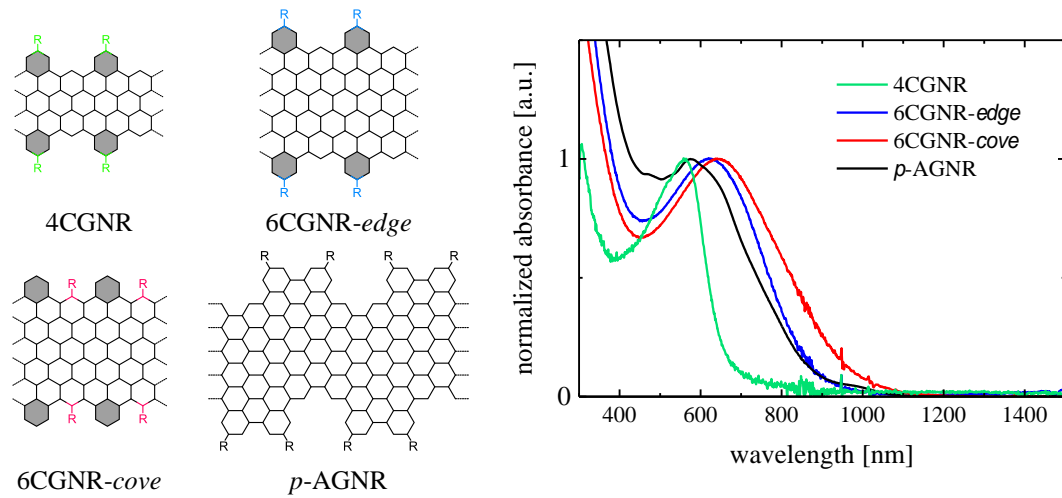


Figure 2.6: (left) Four different chemically synthesized GNRs with various edge structure, widths, and alkyl chain position. (right) Optical densities of GNRs samples shown in the left. Characterization has been performed on the suspensions of GNRs in 1,2,4-Trichlorobenzene. Adapted with permission from *J. Am. Chem. Soc.* 2017, 139, 7982–7988 [129]. Copyright (2017) American Chemical Society.

However, the bandgap, in this case, reduces with the increasing width of the GNR – and once again it collapses to the gapless and linear graphene band structure in the limit of very wide GNR.

In general, one cannot say straightaway what band structure, i.e., metal- or semiconductor-like, characterizes any particular GNR structure. Figure 2.6 shows several GNRs with different edge structures and widths together with the optical density (OD) measured in these structures. The OD here gives an approximate experimental indication of the bandgap widths. In the general case, one has to resort to numerical calculations of the band structure.

The gap and specifically the curvature of the bands in GNRs (and in CNTs as well) renders the conduction properties of the carriers as that of massive particles. The consequences of this are observed in OD spectra (Figure 2.6, right) that is dominated with a characteristic exciton peak – a bound electron-hole pair. The massive particles tend to bind more. Particularly for excitons, the mass of a charge defines the binding energy [34], i.e., $E_B = \mu e^4 / 2\hbar^2 \epsilon^2$, here μ is the reduced mass of an electron-hole pair.

The field of the study of GNRs is very rapidly growing, and substantial progress has been achieved in its fabrication methods. It has started from the top-down approaches like the actual slicing of the graphene monolayer into GNRs using lithography [35], [36], or unzipping of carbon nanotubes [37], [38] and culminated in the bottom-up chemical synthesis of GNRs

[12], [39], [40]. The pioneer of the latter approach is the group of Prof. Müllen from the Max Planck Institute for Polymer Research in Mainz, and they are our close collaborators who have provided us with the samples.

The bottom-up chemical synthesis has a series of benefits. It allows producing a macroscopic amount of identical GNRs with a defined edge structure that is determined by the chemical synthesis protocol. Thus, it is possible to engineer a particular type of GNR where, for instance, the width of a nanoribbon can be controlled with atomic precision, whereby the electronic bandgap and related optical properties can be tuned. Moreover, the edge structure can also be customized, providing a way towards predictable band structure of the GNR.

One synthesizes GNRs in a liquid thus the final product is a dispersion of the GNRs in a solvent. Due to this specificity, these GNRs have functional alkyl chains attached to the specific atom sites, in an ordered and periodic manner (Figure 2.6, left). These chains render the solubility of the GNRs, and one can choose a specific chain.

2.3 Conductivity models

In this thesis, we investigate the conductivity of an ensemble of carriers. It is vital to understand the basic mechanisms behind these processes. In this part, we will describe the most common conductivity models that apply to the investigated materials. We note that some of these models have a phenomenological interpretation, i.e., the model describes the observed phenomena without the necessity to rely on the corresponding fundamental microscopic origin of the processes.

2.3.1 The Drude model

The simplest model that describes the complex-valued conductivity of the charge carriers in the presence of an accelerating electric field is the Drude model. The model or rather its version that was initially proposed by Paul Drude in 1900 [41], [42] describes the conductivity of electron gas in metal and regards it as a classical gas (i.e., the Maxwell-Boltzmann distribution describes its equilibrium state) of charged particles experiencing a diffusive motion. Here we will describe it in a more general way as with time it proved to be relevant to numerous types of materials. This part summarizes the material presented in Ref. [19], [43].

The Drude model bears close similarity to the classical kinetic theory of gases. Thereby, the major assumptions of the Drude model are:

- Between collisions, an electron (and generally speaking a charge carrier) does not interact with the lattice and other electrons. These are known as *free electron* and *independent electron* approximations.
- Collisions are instantaneous events that abruptly alter the velocity of an electron.
- An electron experiences a collision with the rate of $1/\tau$. The time τ is known as the relaxation time or the mean free time and it is taken to be independent of electron's position and velocity.
- Electrons are assumed to achieve thermal equilibrium with their surroundings only through collisions.

Following these assumptions, one can say that once an external driving field \vec{E} is removed, the system (a metal) reaches its equilibrium i.e., the state with zero average momentum $\langle \vec{p} \rangle = 0$ of electrons, within the average time τ . The rate equation describing this process is

$$\frac{d\langle \vec{p} \rangle(t)}{dt} = -\frac{\langle \vec{p} \rangle(t)}{\tau} \quad (2.23)$$

In the presence of the external (in general time-dependent) electric field $\vec{E}(t)$, the equation of motion reads as

$$\frac{d\langle \vec{p} \rangle(t)}{dt} = -\frac{\langle \vec{p} \rangle(t)}{\tau} - e\vec{E}(t) \quad (2.24)$$

The current density of these moving electrons is given by $\vec{J}(t) = -Ne\langle \vec{p} \rangle(t)/m$, where N is the electron density; m is the electron mass, and $-e$ is its charge. For the external electric field oscillating with angular frequency ω , i.e., $\vec{E}(t) = \vec{E}_0 e^{-i\omega t}$, the resulting solution of the equation of motion gives the expression for the frequency dependent complex conductivity (also referred to as Drude conductivity, see Figure 2.7):

$$\hat{\sigma}_{Drude}(\omega) = \frac{\vec{J}}{\vec{E}} = \frac{Ne^2\tau}{m} \cdot \frac{1}{1 - i\omega\tau} \quad (2.25)$$

Within the Drude picture, electrons move in the crystal with average thermal velocity $\langle v_{th} \rangle$, which can be evaluated from the Maxwell-Boltzmann distribution as $\langle v_{th} \rangle = \sqrt{3k_B T/m}$

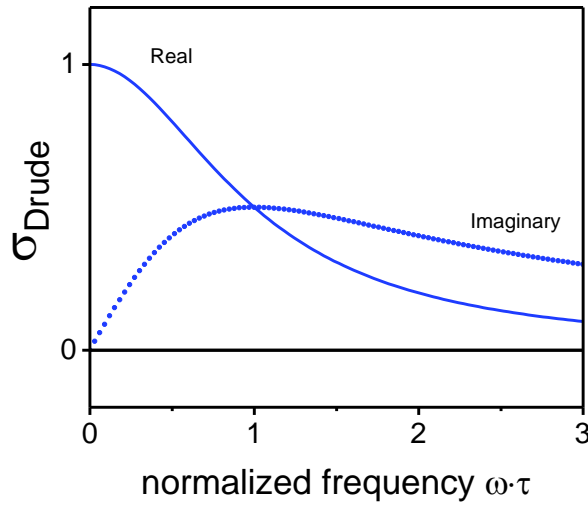


Figure 2.7: Drude conductivity as a function of normalized frequency (i.e., angular frequency times scattering time). The real and the imaginary part cross each other at the point $\omega\tau = 1$.

(mean square velocity [44]). The mean free path of electrons between two consecutive collisions can be then evaluated as $l = \langle v_{th} \rangle \tau$.

Later Sommerfeld refined this picture [45]. Within this framework, electrons obey not classical but quantum statistics, i.e., Fermi-Dirac distribution. Resulting conductivity of a metal is then due to electrons located in the phase space near the Fermi surface. Other electrons lying deeper below the Fermi level stay unperturbed by the external electric field. Even though electrons in this picture are quantum particles, not classical ones, the frequency dependent conductivity has the same expression (2.25). The only difference is that the free path of an electron has to be evaluated now as $l = v_F \tau$.

The impact of the periodic structure of the material (i.e., the conductivity of Bloch electrons), broadly speaking, can be incorporated in the term of the effective mass. Thereby, one can write the complex Drude conductivity (sometimes it is also called Drude-Sommerfeld) as

$$\hat{\sigma}_{Drude}(\omega) = \frac{Ne^2\tau}{m^*} \cdot \frac{1}{1 - i\omega\tau} \quad (2.26)$$

This equation works well for semiconductors (like GNRs) where effective mass appears naturally for the conductive charges near the band extrema which are described by quasi-free electron dispersion law $\mathcal{E}(\vec{p}) = p^2/(2m^*)$. The electrons in graphene have a different dispersion. Thereby the derivation of the conductivity in graphene demands a more general

approach – semi-classical theory. This nevertheless leads to a qualitatively similar spectral shape of the conductivity as in (2.25) or (2.26).

2.3.2 Semi-classical theory of the conductivity

The semi-classical approach is a more general way to describe electron dynamics in the crystal. It treats electron of the crystal as Bloch electrons while describes the current-driving electromagnetic field classically.

The Bloch theory extends the free electron theory of Drude and Sommerfeld to the case where the periodic potential of the lattice is present. The momentum of the Bloch electron is the quasi-momentum – it corresponds to a wave vector in the first BZ. The dispersion of the electron now has no quadratic dependency on its quasi-momentum (except in some cases) like in free-electron case, for instance in graphene it has a linear form near K and K' points.

The semi-classical Boltzmann equation [19], [44] for the AC (alternating current) conductivity of the isotropic and three-dimensional medium (in the relaxation time approximation) reads:

$$\hat{\sigma}(\omega) = \nu e^2 \int \frac{d\vec{k}}{(2\pi)^3} \cdot \frac{v^2(\vec{k})}{3} \cdot \frac{1}{1/\tau(\mathcal{E}(\vec{k})) - i\omega} \cdot \left(-\frac{\partial f(\mathcal{E})}{\partial \mathcal{E}} \right) \quad (2.27)$$

where ν is the degeneracy, $\vec{v}(\vec{k})$ is the carrier band velocity, $\tau(\mathcal{E}(\vec{k}))$ is the energy-dependent relaxation time, f is the Fermi distribution function. The carrier nature now expressed via its dispersion $\mathcal{E}(\vec{k})$, in particular, the carrier velocity is calculated now as $\vec{v}(\vec{k}) = \hbar^{-1} \partial \mathcal{E}(\vec{k}) / \partial \vec{k}$. The number three in the denominator under the squared velocity reflects the isotropic nature of the three-dimensional medium.

We would like to note the importance of the negative derivative of the Fermi–Dirac distribution function in (2.27). This function is a peak shape function (Figure 2.8) that peaks at the Fermi level with a width of a few times $k_B T$ (at finite temperatures). It takes practically zero value outside of this finite region thereby once again highlighting the fact that only electrons with energies near Fermi level contribute to the conductivity of the material.

One can show that in the approximation of free electrons the expression (2.27) can be reduced to the classical Drude-Sommerfeld expression for three-dimensional metals. In this case $v^2 = 2\mathcal{E}/m$ and using substitution (2.7), one can rewrite (2.27) as

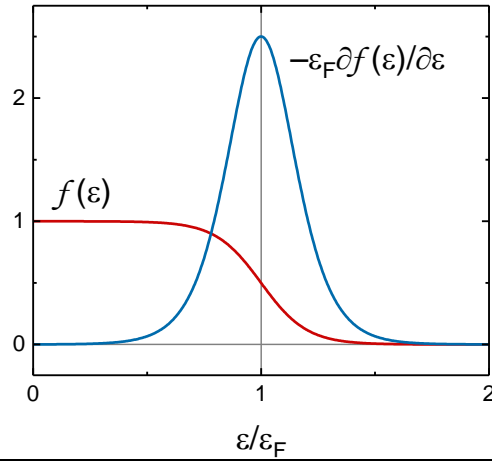


Figure 2.8: The equilibrium distribution function of particles obeying the Fermi–Dirac statistics (red line) and its negative derivative with respect to energy (blue line, normalized to $1/\varepsilon_{\mathcal{F}}$). The plotted functions correspond to the state with $k_{\mathcal{B}}T/\varepsilon_{\mathcal{F}} = 0.1$

$$\hat{\sigma}(\omega) = \frac{2e^2}{3m} \int d\varepsilon g(\varepsilon) \cdot \varepsilon \cdot \frac{1}{1/\tau(\varepsilon) - i\omega} \cdot \left(-\frac{\partial f(\varepsilon)}{\partial \varepsilon} \right) \quad (2.28)$$

In the Sommerfeld picture of metals, the Fermi level (measured from the bottom of the conduction band) ranges from a few to tens of electron-volts. Thus, at room temperature ($k_{\mathcal{B}}T = 0.026$ eV), the edge of the Fermi distribution can be approximated as a step and thereby $-\partial f(\varepsilon)/\partial \varepsilon \approx \delta(\varepsilon - \varepsilon_{\mathcal{F}})$, where $\varepsilon_{\mathcal{F}}$ is the Fermi level. This allows us to evaluate the integral (2.28):

$$\hat{\sigma}(\omega) = \frac{2e^2}{3m} g(\varepsilon_{\mathcal{F}}) \cdot \varepsilon_{\mathcal{F}} \cdot \frac{1}{1/\tau(\varepsilon_{\mathcal{F}}) - i\omega} \quad (2.29)$$

The density of states for the free fermions evaluated at the Fermi level is $g(\varepsilon_{\mathcal{F}}) = (3/2)N/\varepsilon_{\mathcal{F}}$. Thus, the expression for the conductivity simplifies to the familiar Drude model:

$$\hat{\sigma}(\omega) = \frac{Ne^2}{m} \cdot \frac{1}{1/\tau(\varepsilon_{\mathcal{F}}) - i\omega} \quad (2.30)$$

The carriers in graphene are 2D massless Dirac fermions, i.e., they have linear dispersion $\mathcal{E}(\vec{k}) = \hbar v_{\mathcal{F}} |\vec{k}|$. The notable difference of carriers in graphene from the massive carriers is that their velocity magnitude is independent from their momentum

$\vec{v}(\vec{k}) = \hbar^{-1} \partial \mathcal{E}(\vec{k}) / \partial \vec{k} = v_{\mathcal{F}} \vec{k} / |\vec{k}|$. As it was stated before, this assumption is valid for the carriers in the vicinity of Dirac points. The semi-classical Boltzmann equation for the AC conductivity in graphene reads as:

$$\begin{aligned} \hat{\sigma}(\omega) &= v e^2 \int \frac{d\vec{k}}{(2\pi)^2} \cdot \frac{v^2(\vec{k})}{2} \cdot \frac{1}{1/\tau(\mathcal{E}(\vec{k})) - i\omega} \cdot \left(-\frac{\partial f(\mathcal{E})}{\partial \mathcal{E}} \right) = \\ &= \frac{v e^2 v_{\mathcal{F}}^2}{2} \int \frac{d\vec{k}}{(2\pi)^2} \cdot \frac{1}{1/\tau(\mathcal{E}(\vec{k})) - i\omega} \cdot \left(-\frac{\partial f(\mathcal{E})}{\partial \mathcal{E}} \right) \end{aligned} \quad (2.31)$$

The two in the denominator under the squared velocity reflects the two-dimensional nature of graphene.

In general, one cannot simplify the Fermi distribution in graphene as a step function as the Fermi level is comparable with the thermal energy. To calculate this integral one has to use the explicit expression of Fermi-Dirac distribution and to have knowledge of the energy dependence of the scattering time. The latter is often not that explicit. For now, we calculate the conductivity in graphene assuming that the scattering time is a constant or changes subtly for the carrier energies around chemical potential. To this end, we perform the integration in (2.31) by replacing the integral over momentum with the integral over energy using identity (2.7) and the expression for the density of states in graphene (2.9). The negative derivative of the Fermi-Dirac distribution reads as:

$$-\frac{\partial f(\mathcal{E})}{\partial \mathcal{E}} = -\frac{\partial}{\partial \mathcal{E}} \frac{1}{\exp\left(\frac{\mathcal{E} - \mu}{k_B T}\right) + 1} = \frac{1}{k_B T} \cdot \frac{\exp\left(\frac{\mathcal{E} - \mu}{k_B T}\right)}{\left(\exp\left(\frac{\mathcal{E} - \mu}{k_B T}\right) + 1\right)^2} \quad (2.32)$$

where μ is the chemical potential and k_B is Boltzmann constant. Using (2.32) and performing the integration over the energies one can finally write the conductivity in graphene as

$$\hat{\sigma}(\omega) = \frac{2e^2}{\pi \hbar^2} \cdot k_B T \cdot \ln\left(2 \cosh\left(\frac{\mu}{2k_B T}\right)\right) \frac{1}{1/\tau - i\omega} \quad (2.33)$$

The latter expression repeats the spectral shape of the complex Drude conductivity with the only difference in the pre-factor. In the limit of the thermal energy being lower than the chemical potential, i.e., a degenerate electron gas, this pre-factor simplifies to $\mu e^2 / \pi \hbar^2$. Given that in graphene $\mu = \hbar v_{\mathcal{F}} \sqrt{\pi N}$, one can thus say that the conductivity is proportional to \sqrt{N} .

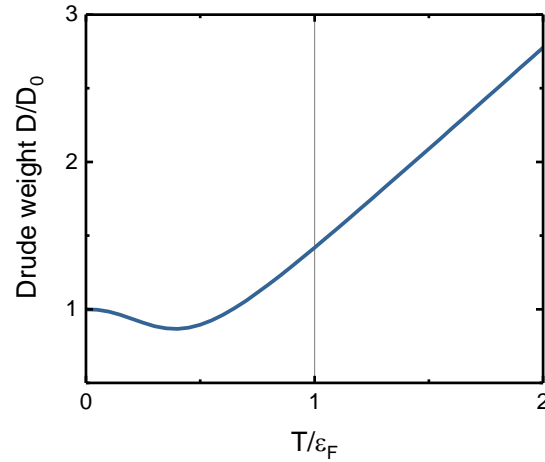


Figure 2.9: Normalized Drude weight as a function of normalized to the Fermi energy temperature in graphene.

This differs from the normal Drude conductivity (2.25) of a 3D metal where it is a linear function of the carrier density N .

Often in the literature, the value $(2e^2/\hbar^2) \cdot k_B T \cdot \ln(2 \cosh(\mu/2k_B T))$ is called the Drude weight \mathcal{D} [46]–[48]. It is temperature and chemical potential dependent or simply temperature dependent (as the chemical potential is also temperature dependent) as it is shown in Figure 2.9. This fact highlights the importance of the electron temperature for the conductivity properties of graphene. One finally writes the complex conductivity in graphene in a compact form:

$$\hat{\sigma}(\omega, T) = \frac{\mathcal{D}(T)}{\pi} \cdot \frac{1}{1/\tau - i\omega} \quad (2.34)$$

2.3.3 The conductivity of quasi-free electrons – Drude-Smith model

In the previous sections, we have described the conductivities of the carriers in a continuous medium within the assumption that upon every scattering event the momentum is random. These models do not account for the possible persistence of the momentum that takes place at, for instance, crystal boundaries. A criterion for this to occur is that the carrier mean-free path l becomes greater than the dimension L of the material, i.e. $v_F \tau > L$. In cases when this process dominates the carrier dynamics, one should employ models accounting for this process.

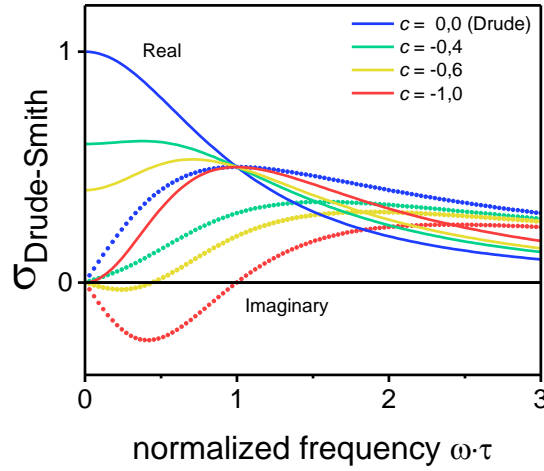


Figure 2.10: Drude-Smith complex-valued conductivity as a function of normalized frequency (i.e., angular frequency times scattering time) for a few values of the backscattering parameter c . Solid and dotted lines correspond to the real and imaginary parts of the conductivity, respectively. Notably, Drude-Smith conductivity reduces to Drude conductivity of free carriers with parameter $c = 0$.

An extension to the Drude model accounting for the restricted motion of the carriers has been proposed by Smith [49], in which a carrier retains part of its initial velocity upon scattering. Smith's generalization of the Drude model is given by:

$$\hat{\sigma}_{DS}(\omega) = \hat{\sigma}_{Drude}(\omega) \left(1 + \sum_{p=1}^{\infty} \frac{c_p}{(1 - i\omega\tau)^p} \right) \quad (2.35)$$

The coefficient c_p represents here the fraction of the electron's original velocity that is retained after the p -th collision. For elastic collisions the parameter c_p is the expectation value $\langle \cos \theta \rangle$, for scattering angle θ . If the carrier's momentum is randomized then $c_p = 0$, while if it is completely backscattered then $c_p = -1$. It is commonly assumed that the persistence of velocity is retained only for the first scattering event so the infinite summation is truncated at the first term ($p = 1$), for the sake of simplicity here one writes c_1 simply as c . Figure 2.10 shows the Drude-Smith (DS) conductivity predicted by expression (2.35) for a variety of values of the backscattering parameter c .

Chapter 3

Terahertz time-domain spectroscopy

Terahertz spectroscopy is ideally suited for measurements of the ultrafast dynamics in three subsystems of a solid: charges (free, bound), lattice (phonon modes) and the spin – because characteristic time scales of these phenomena lie in the sub-picosecond time scale. The THz range is loosely defined between 100 GHz and 30 THz [50], thus in this frequency range one can perform the spectroscopy in the unique regime of $\omega\tau \approx 1$, where ω is the angular frequency of the electromagnetic wave, and τ is the ultrafast (sub-)picosecond dynamics of charge, lattice, and spin.

Historically, the development of the technology of THz sources and detectors had two major approaches – from the optics side, descending from higher frequencies – and the electronics side, climbing up from lower frequencies. Unfortunately, the performance in both cases was unsatisfactory and demanded complex technology. In the electronics, for instance, with reaching that high frequency it becomes not beneficial exploiting waveguides as electromagnetic radiation experiences inevitable losses. Thus, it requires using the expensive waveguides of the highest quality. Using the incoherent optical detectors for THz radiation is also cumbersome as it requires using cryogenic temperatures to minimize the loss of the detecting THz radiation in the thermal noise (1 THz corresponds to the photon energy of only 4.1 meV, much lower than thermal energies at room temperature, for which $k_B T \cong 26$ meV). The THz spectroscopy boom was spurred by the development of laser-based ultrafast coherent sources and invention of the coherent detection scheme, which we will explain further in the text.

THz time-domain spectroscopy (THz-TDS) is based on the generation and coherent detection of freely propagating short electromagnetic pulses of THz radiation, which are used for probing a material of interest. The probe THz pulse is essentially an electromagnetic surge of few picoseconds long and typically containing frequencies in the 0.1-3 THz range, see Figure

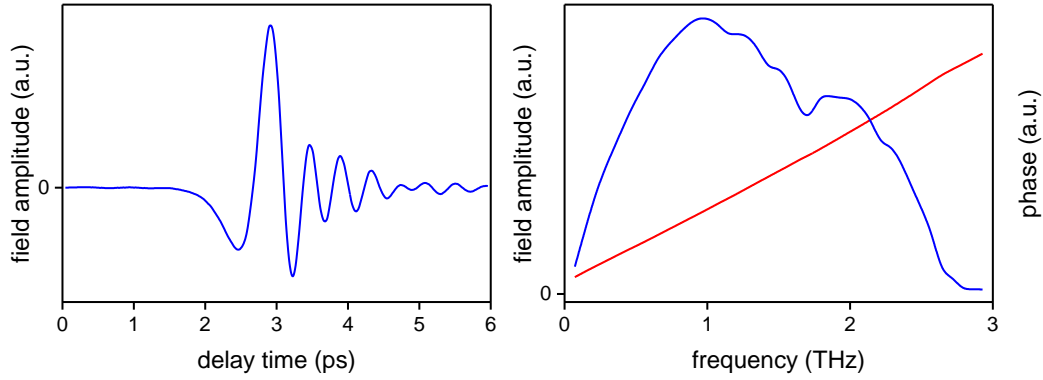


Figure 3.1: The electric field in THz pulse in time-domain together with its phase and frequency spectra. The data have been obtained in ZnTe-based setup employing optical-rectification for the pulse generation and free-space electro-optic sampling for its detection.

3.1. The pulse is sensitive to mobile charge carriers as well as quasi-free charges like bound excitons and polar phonon modes. THz spectroscopy provides access to electronic properties on the sub-picosecond timescales without applying physical contacts to the samples (since it employs free propagating pulses). The latter is particularly beneficial for studies of the nanostructured systems such as GNRs, where applying contacts would inevitably modify the intrinsic electronic properties of GNRs. Another advantage of THz spectroscopy is that the employed coherent detection scheme allows recording the strength of electric field of the THz waveform in time, thus providing information not only on the amplitude of transmitted probe pulse but also on its phase. Applying a Fourier transformation to these recorded traces in the time domain allows extracting electronic properties of the samples as a function of frequency. The Fourier transformation implies that the reported properties are complex valued. There are three equivalent ways to represent this information in the form of complex-valued refractive index $\hat{n}(\omega)$, the permittivity $\hat{\epsilon}(\omega)$ and the conductivity $\hat{\sigma}(\omega)$, where $\omega = 2\pi f$ is the angular frequency of the oscillation probe field (f here is the ordinary frequency measured in THz). All these three quantities are related as [43]

$$\begin{aligned}\hat{\epsilon}(\omega) &= \hat{n}^2(\omega), \\ \hat{\sigma}(\omega) &= -i\hat{n}^2(\omega)\epsilon_0\omega = -i\hat{\epsilon}(\omega)\epsilon_0\omega\end{aligned}\tag{3.1}$$

where ϵ_0 is the vacuum permittivity, thus they represent essentially the same information about optical (or optoelectrical) properties of the material and can be used interchangeably. For instance, the complex refractive index which reads as $\hat{n}(\omega) = n(\omega) + i\kappa(\omega)$ comprises the real part $n(\omega)$, indicating the phase velocity of the propagating probe field, and the imaginary

part $\kappa(\omega)$ (also known as extinction coefficient) indicating the amount of attenuation when the electromagnetic wave propagates through the material. In this thesis, the data obtained with the THz probe is primarily expressed in the form of the complex valued conductivity $\hat{\sigma} = \sigma_1 + i\sigma_2$. The real part σ_1 defines the absorption of the electromagnetic wave in the medium. According to the Ohm's law, the real part of conductivity correlates the conduction current density with the electric field, i.e., $j = \sigma_1 E$. The imaginary part σ_2 is the measure of the phase of the total oscillating current (conduction plus polarization current), relative to that of the driving oscillating field.

In the following sections, we describe the basics of the coherent THz generation and detection as well as the experimental setup used in this thesis.

3.1 Terahertz generation and detection

The generation and coherent detection of broadband THz pulses employ ultrashort (sub 100 fs) near-infrared pulses. All measured data presented in this dissertation were obtained in the experiments where we utilized nonlinear optical effects for generation and detection of THz pulses. The generation is based on the frequency down-conversion using the second-order nonlinear effect known as optical rectification. For detection, we employ the electro-optic (EO) sampling which is based on the phenomenon called the Pockels effect.

There are other techniques utilized for THz generation such as a photoconductive antenna (known as Auston switch) or air-plasma source. There is also a novel approach converting ultrafast spin currents into ultrafast THz-emitting conduction current in ferromagnetic/nonmagnetic metal nanostructures [51]. All of them have their pros and cons, but nonlinear crystals demand a minimum to begin with, as they do not involve using complex electrical equipment to drive those sources and detectors.

In the following two subsections, we describe the basic concepts of THz generation with optical rectification and detection employing EO sampling.

3.1.1 Optical rectification

In this section, we introduce the optical rectification that is utilized for THz pulse generation. To make this phenomenon easier to comprehend we will show its derivation in a simplified form. Optical rectification is a process which is investigated in nonlinear optics – the study of

the phenomena taking place as a result of the modification of the optical properties of a material by the presence of light (or an electromagnetic wave in a broader sense) of higher intensity. To make it clear what nonlinearity means, let us consider how the polarization $P(t)$ of a material depends on the optical field strength $E(t)$. Usually, the optical response of the material in the general case can be described by expressing its polarization as a power series (so-called perturbative representation) in the applied field strength as

$$\begin{aligned} P(t) &= \varepsilon_0(\chi^{(1)}E(t) + \chi^{(2)}E^2(t) + \chi^{(3)}E^3(t) + \dots) \\ &= P^{(1)}(t) + P^{(2)}(t) + P^{(3)}(t) + \dots \end{aligned} \quad (3.2)$$

The quantity $\chi^{(1)}$ is known as the linear susceptibility, while $\chi^{(2)}$ and $\chi^{(3)}$ are the second- and third-order nonlinear susceptibilities, respectively. As is clear from the naming above, in the case of conventional linear optics, one has to consider only the first term, whilst nonlinear optics deals with higher-order terms. According to ref. [52], an order-of-magnitude estimate of these quantities in the common case is as follows. The lowest nonlinear term $P^{(2)}$ is comparable to the linear response $P^{(1)}$ when the applied field strength E is of the order of the characteristic atomic electric field strength $E_{\text{at}} = e/(4\pi\epsilon_0 a_0^2) \approx 5.14 \times 10^{11}$ V/m (where a_0 is the Bohr radius of the hydrogen atom). Thus, the second order susceptibility $\chi^{(2)}$ will be of the order of $\chi^{(1)}/E_{\text{at}} \approx 1/E_{\text{at}} \approx 1.94 \times 10^{-12}$ m/V. Similarly, one can expect $\chi^{(3)}$ to be of the order $\chi^{(1)}/E_{\text{at}}^2 \approx 3.78 \times 10^{-24}$ m²/V². Thereby high order terms become important in the case when sufficiently strong electric fields are present in the material. For the sake of simplicity, the polarization and field in Eq. (3.2) have been taken as scalar quantities. In general, they have to be considered as three-dimensional vector quantities and in such a case $\chi^{(1)}$ is a second-rank tensor, $\chi^{(2)}$ is a third-rank tensor, and so on. We stick to this simple scalar form, as it is useful to grasp what the optical rectification is. The optical rectification is a second-order nonlinear process, and thus we have to consider the second-order term, i.e., $P^{(2)}(t)$, which we denote as $P_{NL}(t)$. Now, let us consider the case of a continuous-wave laser beam incident on a crystal with non-zero second-order susceptibility $\chi^{(2)}$, i.e., on a crystal without inversion symmetry. This beam is essentially a monochromatic electromagnetic wave with the electric field given by:

$$E_{CW}(t) = E_0 e^{-i\omega t} + E_0^* e^{i\omega t} \quad (3.3)$$

This electric field creates the nonlinear polarization $P_{NL} = \varepsilon_0 \chi^{(2)} E_{CW}^2(t)$. Substituting the electric field in the last expression with Eq. (3.3) gives

$$P_{NL}(t) = 2\varepsilon_0\chi^{(2)}E_0E_0^* + (\varepsilon_0\chi^{(2)}E_0^2e^{-2i\omega t} + \text{c. c.}). \quad (3.4)$$

This nonlinear polarization consists of a static contribution (the first term) and a contribution which oscillates at double frequency of the incident wave, i.e., 2ω . The first term in this expression represents a static polarization $P_{OR} = 2\varepsilon_0\chi^{(2)}E_0E_0^*$ created across the crystal and it is responsible for a process named optical rectification. The second term governs a process called second harmonic generation.

Before we proceed further, it is worth discussing why the polarization is so important. The reason that the polarization plays a crucial role in nonlinear optics is that a time-varying polarization can create new components of electromagnetic field essentially appearing as a new source. This phenomenon is governed by a wave equation which has the form

$$\nabla^2 E - \frac{n^2}{c^2} \frac{\partial^2 E}{\partial t^2} = \frac{1}{\varepsilon_0 c^2} \frac{\partial^2 P_{NL}}{\partial t^2}. \quad (3.5)$$

Here $\partial^2 P_{NL}/\partial t^2$ is the source term, n is the linear refractive index and c is the speed of light in vacuum. This equation can be interpreted as a nonhomogeneous wave equation in which (nonlinear) polarization P_{NL} drives the electric field E . Since P_{NL} is proportional to the relative displacement of bound charges in the medium then $\partial^2 P_{NL}/\partial t^2$ is a measure of the acceleration of these charges, thus this equation is in line with the Larmor's law of classical electromagnetism which states that accelerating charges radiate electromagnetic waves.

Now, going back to our point, as it was mentioned in the case of the continuous electromagnetic wave incident on a medium with non-zero second-order susceptibility, the optical rectification creates a static polarization, which thus cannot produce a new electromagnetic wave. However, things change when one employs pulsed electromagnetic waves like the output of femtosecond lasers. Assume that now we have a laser pulse with the electric field which can be described in time as a monochromatic wave modulated by a Gaussian envelope function with FWHM duration τ :

$$E_{pulse}(t) \propto E_0 \exp\left(-4 \ln(2) \frac{t^2}{\tau^2}\right) (e^{-i\omega t} + \text{c. c.}). \quad (3.6)$$

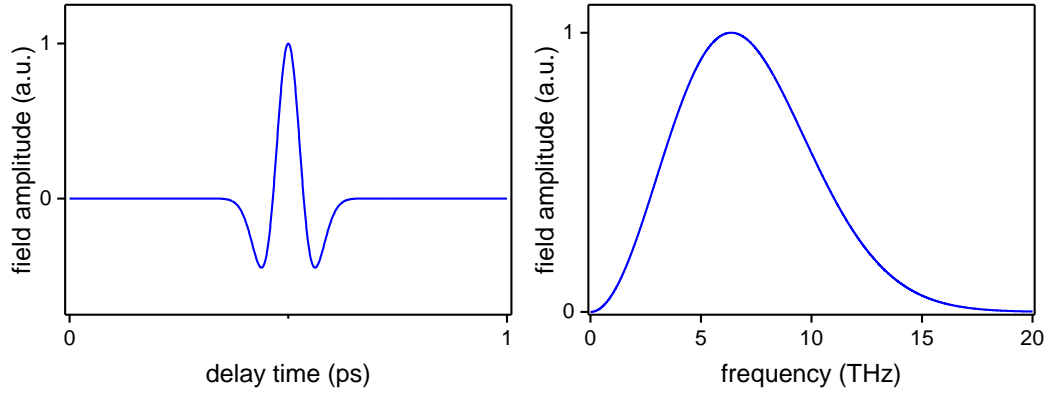


Figure 3.2: THz pulse in time-domain and its spectra generated by 50 fs long electromagnetic pulse within the qualitative theory of optical rectification described in the text.

This electric field creates in the medium a nonlinear polarization $P_{NL}(t) = 2\varepsilon_0\chi^{(2)}E_{pulse}(t)E_{pulse}^*(t)$ which can be rewritten as $P_{NL}(t) = P_{OR}(t) \propto \exp(-t^2/\tau^2)$. This polarization is time dependent and its evolution in time is governed by the envelop function of the incident generating pulse. The ‘non-static’ polarization $P_{OR}(t)$ essentially performs like a time-dependent dipole, which according to classical electrodynamics emits an electromagnetic field (in the far field):

$$\begin{aligned} E_{THz}(t) &\propto \frac{\partial^2}{\partial t^2} P_{OR}(t) \propto \frac{\partial^2}{\partial t^2} \exp(-t^2/\tau^2) = \\ &= \frac{2}{\tau^4} (-2t^2 - \tau^2) \exp(-t^2/\tau^2). \end{aligned} \quad (3.7)$$

The ‘THz’ subscript in the formula above is there for the following reason. If we transform the time domain expression for $E_{THz}(t)$ in the frequency domain using Fourier transformation then it can be shown that this electromagnetic wave indeed contains frequencies in the THz range,

$$E_{THz}(f) \propto f^2 \exp(-(\pi\tau f)^2). \quad (3.8)$$

The generating laser pulses employed in this work have the sub 100 fs duration, thereby if we consider for instance a 50 fs long laser pulse then according to (3.8) the spectrum of the field $E_{THz}(f)$ spans between 0 and 20 THz and has a maximum around 6 THz. Figure 3.2 illustrates this example.

The simplified picture above overestimates the actual frequency range attainable in the laboratory setups, as it does not account for a variety of intricacies taking place during THz

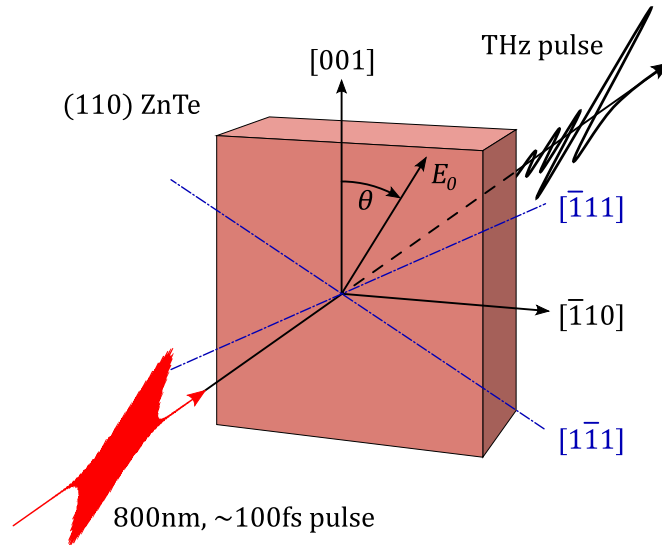


Figure 3.3: Schematic of THz pulse generation via optical rectification of a near IR optical pulse in a ZnTe crystal.

generation via optical rectification. The most impactful one is the phase mismatch between the laser beam $E_{pulse}(t)$ propagating through the nonlinear medium and the generated THz pulse $E_{THz}(t)$ [53]. This process can be simply described as follows. The propagating laser pulse induces the nonlinear polarization at every point of its path through the medium, thus creating multiple sources that emit THz electromagnetic waves with different phases. The laser pulse propagates with the optical group velocity in the nonlinear crystal, corresponding to its wavelength (e.g., 800 nm). At the same time, the THz radiation generated in the crystal, propagates with its own phase velocity corresponding to the specific THz frequency, which is usually lower than the group velocity of the generation laser pulse, creating the phase mismatch between the transient polarization source (generation laser pulse) and the generated THz waves. Upon certain (co-)propagation distance, this leads to negative interference of these THz waves that substantially reduces the output bandwidth of the resulting THz pulse. For instance, the setup used in this work utilizes zinc telluride (ZnTe) crystal for THz generation that usually produces a pulse with a spectrum spanning from 0.2 to 2.5 THz (see Figure 3.1). Additionally, the relative alignment of the polarization and wave vector of generating laser pulse to the crystal axes strongly affect the output magnitude of the THz field. Again, for the example of the ZnTe, the propagation along [001] direction leads to no optical rectification, while the most efficient generation is achieved when laser propagates along of the [110] axis (thus in THz literature it is usually referred as *(110) ZnTe* as the crystal plate is cut along (110)

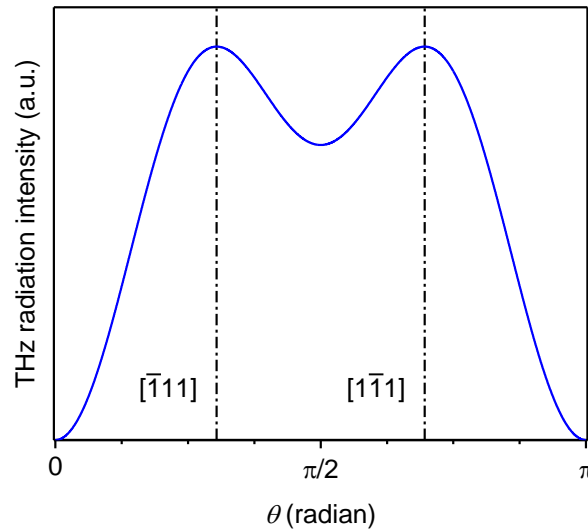


Figure 3.4: The THz field magnitude as a function of the angle between [001] crystal axis and the polarization direction of the sampling near IR pulse (see Figure 3.3).

plane). In this configuration, the output intensity of the THz is further dependent on the angle between field polarization of the generating pulse and [001] axis (see Figure 3.3 and Figure 3.4) as

$$I_{THz}(\theta) \propto \sin^2 \theta (4 - 3 \sin^2 \theta). \quad (3.9)$$

The maximum output emission is achieved when $\theta = \arcsin \sqrt{2/3} \approx 54.7^\circ$, this is illustrated in the Figure 3.4. This corresponds to the cases when the polarization of the generating laser pulse is aligned along the axes $[\bar{1}11]$ or $[1\bar{1}1]$ (see Figure 3.3).

3.1.2 Free-space electro-optic sampling

In this section, we introduce the underlying principles of the coherent detection scheme used in this work known as free-space EO sampling. This phenomenon is based on the Pockels effect – a second-order nonlinear effect taking place in the detection crystal when both THz wave and optical sampling pulse are presented. Similar to the optical rectification it stems from the second-order nonlinear susceptibility. Simply, this effect is the birefringence induced by the electric field of the THz pulse.

In a general case, the induced birefringence depends intricately on the relative alignment of the polarization of the sampling optical and the THz pulses, as well as their orientation to the

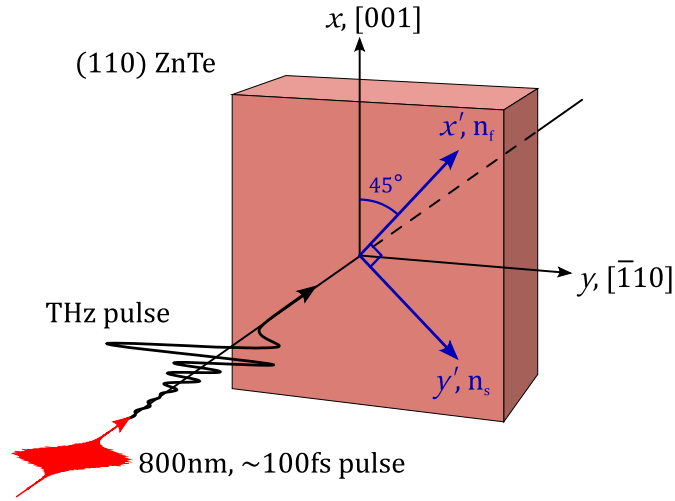


Figure 3.5: Schematic of electro-optic sampling. A THz pulse and optical pulse co-propagate through a ZnTe crystal. The presence of the THz field induces birefringence in the crystal, which changes the polarization of the optical pulse.

crystallographic axes of the detection crystal. Here we describe the detection scheme utilized in this thesis which employs (110) ZnTe plate as a detecting crystal (the same as the generation crystal). In this case, the field-induced birefringence reaches a maximum when both the polarized optical sampling pulse and THz pulses co-propagate perpendicular to the (110) plane and with their polarizations being perpendicular to the [001] axis as shown in Figure 3.5. Here, we define the laboratory frame with x and y axes parallel to [001] and $[\bar{1}10]$ axes respectively (see Figure 3.5).

The induced by the presented THz field fast and slow optical axes x' and y' form a new frame which is rotated in the crystal plane (110) clockwise from the laboratory one at the angle of $\pi/4$. The corresponding induced optical refractive indices n_f and n_s of the fast and slow axes respectively can be written as

$$n_{f,s} \approx n_0 \mp \frac{1}{2} n_0^3 r_{41} E_{THz} = n_0 \mp \delta n. \quad (3.10)$$

Here $n_0 = 2.85$ [54] is the refractive index of the ZnTe at the optical frequency and $r_{41} = 4.1$ pm/V [55] is the EO coefficient of the ZnTe crystal. Therefore, the fast and slow field components of the propagating optical pulse travel with different phase velocities. Because of the difference in phase velocity, one component is retarded relative to the other. This phase retardation changes the polarization state of the so-called emerging optical beam – the one appearing after the crystal.

To quantify this phenomenon, we will use the Jones matrix calculus [56]. This approach is a powerful method in which the electric field vector (or state of polarization) is represented by a two-element column vector, while a 2×2 matrix represents each birefringent crystal plate. Thus, one describes the transmission of light by the multiplication of the input vector with this matrix.

The optical electric field vector of the sampling pulse (Figure 3.5) in the laboratory frame reads as

$$\begin{pmatrix} E_x \\ E_y \end{pmatrix} = E_0 \begin{pmatrix} 0 \\ 1 \end{pmatrix} \quad (3.11)$$

Because the THz induced optical axes oriented at the angle of $\pi/4$ in our laboratory frame, then the transformation of the polarized optical light propagating through ZnTe plate in this frame can be written as

$$\begin{pmatrix} E'_x \\ E'_y \end{pmatrix} = R\left(-\frac{\pi}{4}\right) W_0 R\left(\frac{\pi}{4}\right) \begin{pmatrix} E_x \\ E_y \end{pmatrix} \quad (3.12)$$

Here $R(\psi)$ is the matrix of the clockwise frame rotation at the angle ψ and W_0 is the Jones matrix for a birefringent ZnTe plate which read as

$$R(\psi) = \begin{pmatrix} \cos \psi & \sin \psi \\ -\sin \psi & \cos \psi \end{pmatrix}, \quad W_0 = \begin{pmatrix} e^{in_f kL} & 0 \\ 0 & e^{in_s kL} \end{pmatrix} \quad (3.13)$$

Here $k = \omega/c$ is the optical wave number and L is the thickness of the ZnTe detection crystal. Thus, the emergent optical beam in the laboratory frame writes as

$$\begin{pmatrix} E'_x \\ E'_y \end{pmatrix} = \frac{E_0}{2} \begin{pmatrix} e^{in_f kL} - e^{in_s kL} \\ e^{in_f kL} + e^{in_s kL} \end{pmatrix} = E_0 e^{in_0 kL} \begin{pmatrix} -i \sin \delta\varphi \\ \cos \delta\varphi \end{pmatrix} \quad (3.14)$$

where $\delta\varphi = kL\delta n = kLn_0^3 r_{41} E_{THz}/2$. The right hand side of expression (3.14) contains a Jones vector of the elliptically polarized light with orthogonal components being dependent on the phase factor $\delta\varphi$ which depends linearly on the applied THz field. Thus, this phase factor makes possible measuring experimentally the applied THz field in the following genuinely simple way. The layout of the detection scheme is presented in Figure 3.6.

In this approach, coupled photodiodes detect the incident THz field by comparing the state of the polarization of the optical sampling beam in the case when THz field is absent and, in the case when it is present in the detecting crystal. In the former case, ZnTe crystal acts as a

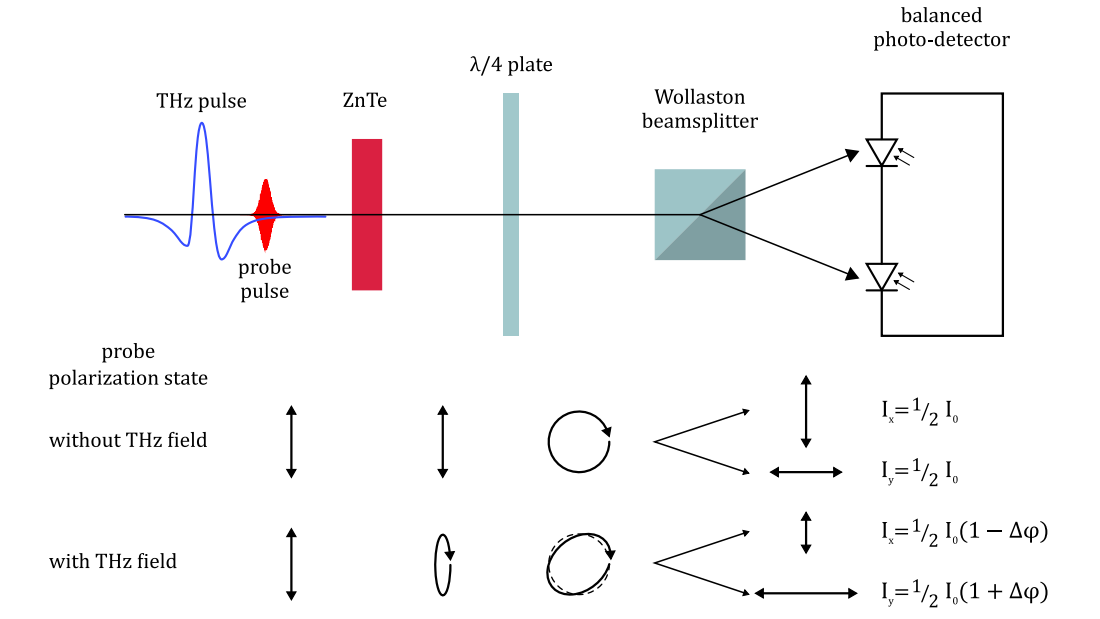


Figure 3.6. Schematic diagram of a typical setup for free-space EO sampling. Probe polarizations with and without a THz field are depicted before and after the polarization optics.

common phase retardation plate. Thus, the propagating sampling pulse acquires additional phase without changing its polarization:

$$\begin{pmatrix} E'_x \\ E'_y \end{pmatrix} = E_0 e^{in_0 kL} \begin{pmatrix} 0 \\ 1 \end{pmatrix} \quad (3.15)$$

In the latter case (with a THz pulse in the detecting crystal), the sampling pulse becomes elliptically polarized (Eq. 3.14).

The detecting laser pulse, upon its propagation through the ZnTe crystal, travels through the quarter-wave plate and the Wollaston beam splitter or prism (see Figure 3.6). The former brings additional phase retardation to the optical field components, essentially transforming linearly polarized light into circularly one. The Wollaston prism splits these components into two separate channels that are detected in the balanced photo-detector. Using the Jones calculus, one writes the Jones vectors of the optical field upon quarter-wave plate as

$$\vec{E}'' = \begin{pmatrix} E''_x \\ E''_y \end{pmatrix} = \frac{E_0 e^{in_0 kL}}{\sqrt{2}} \begin{pmatrix} -i \cos \delta\varphi - i \sin \delta\varphi \\ \cos \delta\varphi - \sin \delta\varphi \end{pmatrix} \quad (3.16)$$

The Wollaston prism sends the x -component and the y -component of this vector in two separate photodiodes of the detector. The intensity incident upon each photodiode is proportional to the square of the electric field. Using Eq. (3.16), we get

$$I_{x,y} = \frac{I_0}{2}(1 \mp \sin 2\delta\varphi) \approx \frac{I_0}{2}(1 \mp 2\delta\varphi) = \frac{I_0}{2}(1 \mp \Delta\varphi) \quad (3.17)$$

Here I_0 is the intensity of the original optical sampling pulse. We use the small signal approximation, in which $\Delta\varphi = 2\delta\varphi \ll 1$, that is true for most cases of EO sampling. For instance, in the case of ZnTe crystal of 1mm thick, this approximation is valid for the field strengths in the THz pulse that are much less than 27 kV/cm. The difference in intensities on the two photodiodes is then

$$\Delta I = I_y - I_x = I_0\Delta\varphi = I_0kLn_0^3r_{41}E_{THz} \propto E_{THz} \quad (3.18)$$

In a realistic situation, the temporal and spectral resolution of EO sampling is limited by three factors: (i) finite pulse duration of optical probe, (ii) dispersion of nonlinear susceptibility, and (iii) mismatch between the optical group and THz phase velocity [53], [57].

3.2 Experimental setup

The experimental setup used in this thesis is shown schematically in Figure 3.7. A titanium-sapphire mode-locked laser drives the setup. The output of the laser is 40 fs short pulses of 800 nm wavelength. The output splits into three parts: two of them are used to generate and detect THz pulses, and the third to excite (pump) the sample under study. The radiation in the pump beam can be up-converted from the default photon energy of 1.55 eV to 3.1eV using frequency doubling nonlinear crystal, usually beta-barium-borate (BBO) or bismuth-borate (BIBO). The latter has better conversion efficiency and damage threshold compared to the former. Some experiments demand using the pump light of the various colors within ultraviolet (UV), visible and infra-red (IR) ranges. To this end, the pump beam is replaced with the output of the optical-parametric amplifier that is also driven by the same Ti-sapphire laser.

One detects the electric field in the THz pulses by delaying the optical sampling pulse using a motorized optical delay stage I (see Figure 3.7). Changing the delay of the sampling pulse with respect to the arrival of the THz pulse at the detecting crystal allows mapping out the temporal profile of the THz pulse. This is performed through several detection cycles of the electric field in a series of THz pulse replicas. To clarify this, the one point (i.e., the amplitude of the electric field) in the THz pulse waveform is acquired in one event of co-propagation of sampling and THz pulses. Then one moves the delay stage I on a specific amount thus delaying the arrival of the sampling pulse and once more performs the detection cycle on another THz

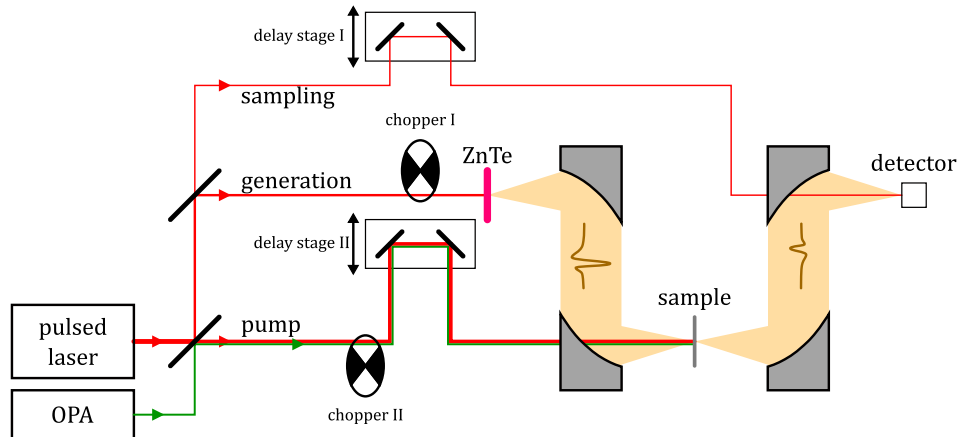


Figure 3.7: A general layout of the THz setup employed in this work. The optical pulse utilized for the sample excitation (pump) comes from the same laser driving THz spectrometer or from an optical parametric amplifier.

pulse. At this moment, another point in the THz pulse is recorded. By repeating these steps one after another, the whole THz pulse is thus recorded. This scheme imposes stability requirements on the output of the laser to ensure that every laser pulse generates the same THz pulse.

We also use a motorized delay stage II (see Figure 3.7) to control the delay of the pump pulse to resolve in time the THz response of the photo-excited samples.

The detector is based on the EO sampling technique described in the previous section. The signal read-out from the balance diodes of the EO detector is performed via a lock-in amplifier. The principle of its work is as follows. A lock-in amplifier performs a multiplication of its input signal with a reference one and then applies an adjustable low-pass filter to the result. Thereby it isolates the signal at the frequency of interest from all other frequency components. To this end, one modulates the input signal at the frequency of the reference signal. In the setup, this is implemented by using optical choppers for the laser pulses, which also set the reference lock-in signal. One utilizes chopper I to record THz signals and chopper II to record modulations of THz signal due to the pump of the sample (see Figure 3.7). By that means, one can also detect weak signals on high-noise backgrounds.

In the following subsections, we are going to introduce the types of experiments, which can be performed on the described THz setup together with the methods of retrieving the optical constants from the measured signals.

3.2.1 Terahertz time-domain spectroscopy

In this experiment, one studies the THz response of a sample in equilibrium (without excitation). The output is usually a complex-valued refractive index or its other forms mentioned at the beginning of this chapter. One chooses the most suitable one to describe the observed response. In this chapter, we briefly describe the experimental procedure and the mathematical approach of deriving the optical constants from this experiment in the most common and relevant cases for this work.

In the experiment, we measure the THz pulse transmitted through the material of interest and compare it with the reference signal. The latter can be a THz pulse propagating through the reference material or just a THz pulse freely propagating through the air.

In the following, we will consider two types of samples one studies in this mode which are a parallel plate or a slab of the material of interest with finite thickness, and a thin film on the substrate. We also provide the formulas for deriving optical constants from the measured reference and sample THz signals.

Thick plane-parallel slab

In the first case, we will consider the propagation of a linearly polarized THz signal through the plane-parallel slab of the dispersive material, i.e., the medium with frequency-dependent complex-valued refractive index (dielectric function, conductivity). Figure 3.8 depicts the propagation of a THz pulse through the free space (dry air or dry nitrogen), the so-called reference signal, and the same THz pulse propagating through the sample with a complex refractive index $\hat{n}_x(\omega) = n_x(\omega) + i\kappa_x(\omega)$. In order to derive this optical property of the sample from the measured time-domain signals, one has to work in the frequency domain. Thus, the Fourier transformation is applied to time-domain signals, and these data are used to obtain optical constants. We will use subscript zero to denote air surrounding the sample, and x for the sample itself. In the following equations, all the parameters are assumed to be frequency-dependent.

The detected reference signal \hat{E}_{ref} and the sample signal \hat{E}_{sam} , according to the Figure 3.8, reads [58]:

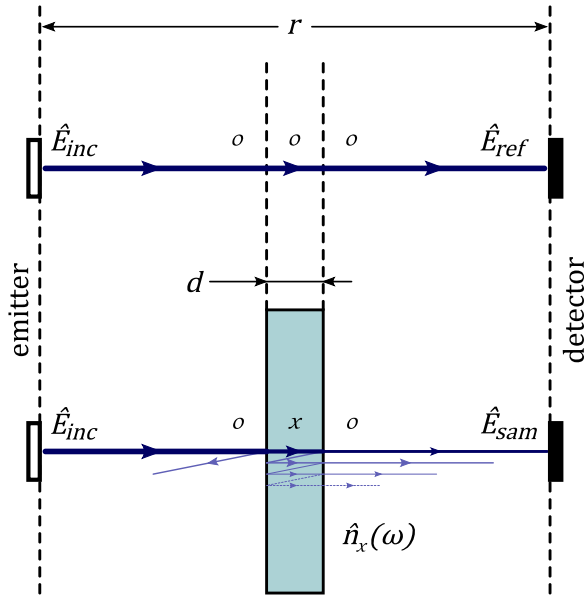


Figure 3.8: Optical paths of the reference and sample signal in the air and a plane-parallel slab.

$$\hat{E}_{ref} = E_{inc} \cdot e^{i\omega r/c} = E_{inc} \cdot e^{i\phi_{free}} \quad (3.19)$$

$$\hat{E}_{sam} = E_{inc} \cdot e^{i\omega(r-d)/c} \cdot \hat{t}_{0x} \cdot e^{i\hat{n}_x \omega d/c} \cdot \hat{t}_{x0} \cdot \widehat{MR}_x = E_{sam} \cdot e^{i\phi_{sample}}$$

where \widehat{MR}_x is a factor that accounts for multiple reflections in the sample slab, which is given by [1]

$$\widehat{MR}_x = [1 + \hat{r}_{0x} \cdot \hat{r}_{x0} \cdot e^{2i\hat{n}_x \omega d/c}]^{-1} \quad (3.20)$$

and \hat{t}_{xy} and \hat{r}_{xy} are Fresnel field transmission and reflection coefficients. Which are given in the case of a normal incidence on the plane boundary between material x and y by [43]:

$$\hat{t}_{xy} = \frac{2\hat{n}_x}{\hat{n}_y + \hat{n}_x}, \quad \hat{r}_{xy} = \frac{\hat{n}_y - \hat{n}_x}{\hat{n}_y + \hat{n}_x} \quad (3.21)$$

The order of indices in (3.21) implies that an electromagnetic wave propagates from medium x into the medium y . The factor \widehat{MR}_x plays a role when the sample in Figure 3.8 is thin enough that the first transmitted THz pulse overlaps in time with the subsequent reflected echoes. Further, we deal with the thick enough samples thereby this factor simply equals one.

From this point, there are two ways to proceed further. In the simplest case of low absorptive medium (i.e., $n \gg k$), we can assume that transmission coefficients are real and are defined

only by the real part of the refractive index, i.e., $\hat{n}_x = n_x$ in eq. (3.21). The extinction coefficient can be rewritten with the power absorption coefficient α_x as $\kappa_x = \alpha_x c / 2\omega$ and taking into account the eq. (3.21) we can write the ratio of the electric fields \hat{E}_{sam} and \hat{E}_{ref} from the eq. (3.19) in the following form:

$$\frac{\hat{E}_{sam}}{\hat{E}_{ref}} = \frac{4n_x}{(1+n_x)^2} e^{-\frac{\alpha_x d}{2}} e^{i(n_x-1)\omega d/c} = \frac{E_{sam}}{E_{inc}} e^{i(\phi_{sample}-\phi_{free})} \quad (3.22)$$

Thus, from the measured phase difference of the sample and reference pulses one can obtain the frequency dependent refractive index as (using $\omega = 2\pi f$) [59]:

$$n_x = \frac{\phi_{sample} - \phi_{free}}{\frac{2\pi f}{c} d} + 1 \quad (3.23)$$

Using this frequency dependent refractive index obtained via (3.23) one can now calculate the absorption coefficient in the sample as [59]:

$$\alpha_x = -\frac{2}{d} \ln \left(\frac{E_{sam}}{E_{inc}} \frac{(1+n_x)^2}{4n_x} \right) \quad (3.24)$$

In the case when the sample has appreciable THz absorption, i.e., the refractive index cannot be approximated only by its real part, the ratio \hat{E}_s/\hat{E}_r takes form:

$$\frac{\hat{E}_{sam}}{\hat{E}_{ref}} = \frac{4\hat{n}_x}{(1+\hat{n}_x)^2} e^{i(\hat{n}_x-1)\omega d/c}. \quad (3.25)$$

This is a transcendental equation with the complex refractive index acting as a variable. To obtain the refractive index, one has to minimize numerically the difference between expressions in the left-hand side of the (3.25) (which is the ratio of Fourier transforms of measured signals, i.e., experimental data) and the right-hand side. Nonetheless, a good starting point for the numerical solution can be the refractive index and the absorption coefficient (which essentially can be written as a complex refractive index) obtained using (3.23) and (3.24). We are not going to describe numerical algorithms employed for this purposes as there is plenty of close-end mathematical software aimed for this and demanding minimum programming skills [60], [61].

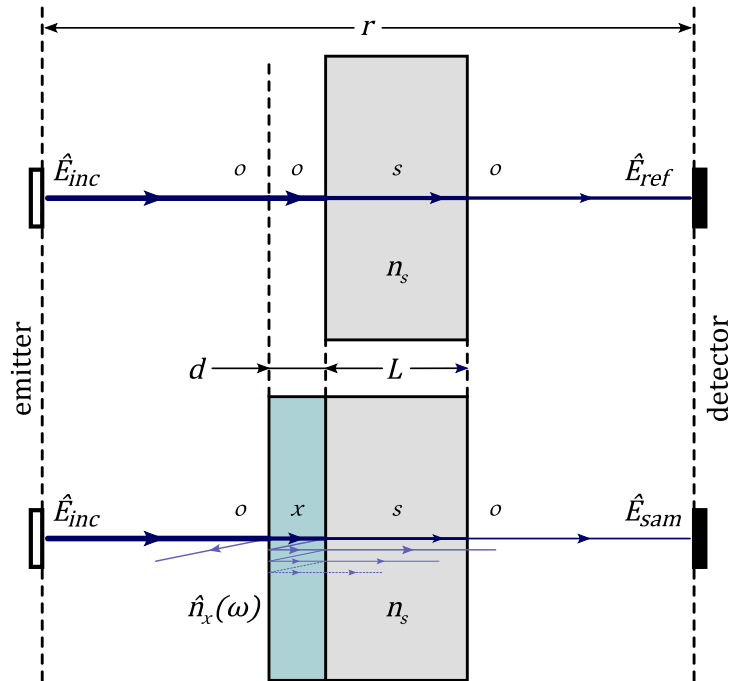


Figure 3.9: The layout of the propagation of the reference and the sample signals through air and a film on a substrate.

Thin film on a dielectric substrate

Here we come to the second major case of the samples. These are thin films on an insulating substrate. Thin in a sense that their thickness is much smaller than the wavelengths of any spectral component of the probing THz pulse. Nevertheless, there is not so much difference in the experiment, despite that one has to measure the reference signal on a blank substrate, i.e., the supporting substrate only, without a thin film sample on it. Firstly, we consider the general case of a sample of finite thickness d on a substrate. Then we introduce the thin film approximation to obtain the mathematical formulas for retrieving the optical properties of thin film samples on a substrate from the measured THz signals.

We start, as in the former case, with a linearly polarized THz pulse normally propagating through the sample and the reference substrate as it is shown in Figure 3.9. We use zero subscripts for the surrounding air, x for the sample and s for the supporting substrate.

Following the same procedure as in the first example, we write down the detected reference and sample signals, according to Figure 3.9 they are [58]:

$$\hat{E}_{ref} = \hat{E}_{inc} \cdot e^{i\omega(r-L)/c} \cdot t_{0s} \cdot e^{in_s\omega L/c} \cdot t_{s0} \quad (3.26)$$

$$\hat{E}_{sam} = \hat{E}_{inc} \cdot e^{i\omega(r-d-L)/c} \cdot \hat{t}_{0x} \cdot \widehat{MR}_x \cdot e^{i\hat{n}_x\omega d/c} \cdot \hat{t}_{xs} \cdot e^{in_s\omega L/c} \cdot t_{s0}$$

Thereby the ratio of the sample signal to the reference one reads as (using the expression (3.20) for the multiple reflections in the sample film):

$$\hat{T} = \frac{\hat{E}_{sam}}{\hat{E}_{ref}} = \frac{e^{-i\omega d/c}}{t_{0s}} \cdot \frac{e^{i\hat{n}_x\omega d/c} \cdot \hat{t}_{0x} \cdot \hat{t}_{xs}}{1 + \hat{r}_{0x} \cdot \hat{r}_{xs} \cdot e^{2i\hat{n}_x\omega d/c}} \quad (3.27)$$

Taking into account expressions for Fresnel coefficients (Eq. (3.21)) and Euler representation of the complex exponent, we can rewrite the latter formula as (the refractive index of air is taken as 1):

$$\hat{T} = \frac{\hat{n}_x(1 + n_s) \cdot e^{-i\omega d/c}}{\hat{n}_x(1 + n_s) \cdot \cos(\hat{n}_x\omega d/c) - i(\hat{n}_x^2 + n_s) \cdot \sin(\hat{n}_x\omega d/c)} \quad (3.28)$$

Now we apply the thin film approximation, i.e., the thickness of the material is smaller than the effective THz wavelength or $d/\lambda \ll 1$. Thereby we can simplify the latter expression as:

$$\hat{T} \cong \frac{\hat{n}_x(1 + n_s) \cdot 1}{\hat{n}_x(1 + n_s) \cdot 1 - i(\hat{n}_x^2 + n_s) \hat{n}_x\omega d/c} = \frac{1 + n_s}{1 + n_s - i(\hat{n}_x^2 + n_s) \omega d/c} \quad (3.29)$$

One can derive from this equation the analytical expression for the refractive index \hat{n}_x , but we are going to make one extra approximation which is the most relevant for the measured data in this work. We assume that our film is highly conductive, i.e., $|\hat{n}_x| \gg 1$ [43]. Thus, using $\hat{n}_x^2 + n_s \approx \hat{n}_x^2$ we can write:

$$\hat{T} = \frac{1 + n_s}{1 + n_s - i\hat{n}_x^2\omega d/c} \quad (3.30)$$

The last expression we can rewrite in terms of conductivity using $\hat{n}_x^2\omega/c = iZ_0\hat{\sigma}$ as:

$$\hat{T} = \frac{1 + n_s}{1 + n_s + Z_0\hat{\sigma}d} \quad (3.31)$$

Thereby the conductivity of the thin film of the thickness d on an insulating substrate with the refractive index n_s reads as:

$$\hat{\sigma} = \frac{1 + n_s}{Z_0d} \left(\frac{1}{\hat{T}} - 1 \right) \quad (3.32)$$

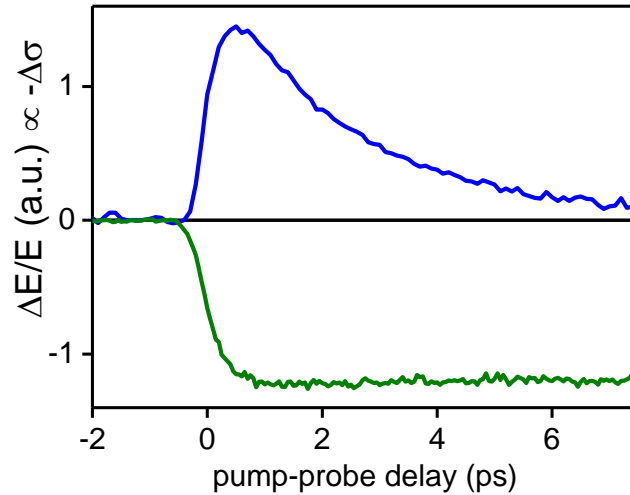


Figure 3.10: Relative change of the probing THz pulse maxima versus pump-probe delay time. Positive photoconductivity is typical for undoped semiconductors (green line) – pure Silicon. Negative photoconductivity is inherent for metal-like conductivity (blue line) – CVD graphene on a fused silica substrate.

here $Z_0 = (\epsilon_0 c)^{-1} \approx 377\Omega$ is the impedance of free space. This is the well known Tinkham equation [62] for a thin conductive film on a substrate.

3.2.2 Optical–pump terahertz–probe spectroscopy

THz time-domain spectroscopy described above studies the samples in equilibrium, but where this technique really reveals its potential is in its extended version that is called time-resolved THz spectroscopy (TRTS). In this experiment, an electromagnetic pulse sets the sample out of the thermal equilibrium, which is then probed with the THz pulse. In this work, we employ optical pulses to excite samples. Therefore, the method is often called optical-pump THz-probe (or OPTP) spectroscopy. In this technique, an optical pulse firstly excites a sample. Then the THz pulse probes the electrodynamic response of the sample with a certain delay time τ upon photoexcitation. The parameter τ is adjustable because of the motorized delay stage II (see Figure 3.7) used in the setup (this is where time-resolution comes from). Thereby one can study the evolution of the THz response of a sample as a function of the pump-probe delay. The THz pulse is usually much longer (1-2 ps) than the optical one (<100 fs) and it is sampled in time-domain as well. The latter brings yet another time parameter (called t , enabled by delay stage I, Figure 3.7) into consideration. Varying one parameter or another allows obtaining different information. We discuss the different cases in the following sections.

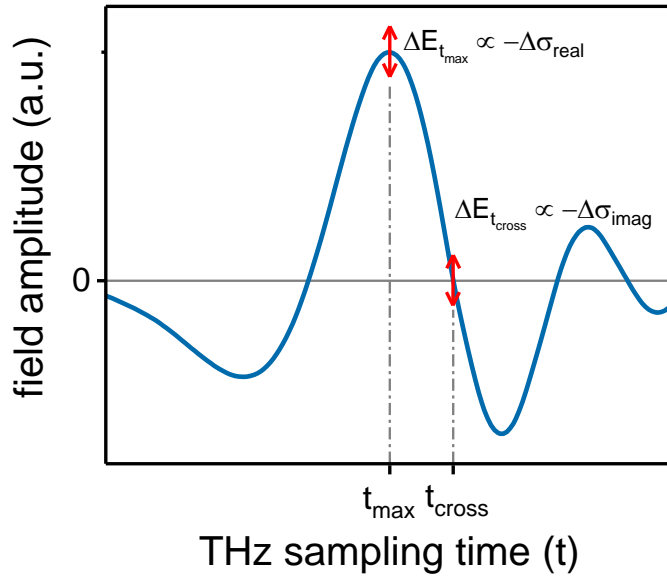


Figure 3.11: By fixing sampling time at the peak of the probing THz pulse, the recorded photoinduced change $\Delta E_{t_{max}}(\tau)$ will give information about the real part of the photoconductivity. When one sets the sampling time at the zero crossing after the peak, $\Delta E_{t_{cross}}(\tau)$ will be proportional to the time delay of the probing THz beam thus providing information about the imaginary part of the photoconductivity.

1D spectroscopy

In this thesis a 1D scan refers to the time-resolved experiment where one obtains a time evolution of the THz transmission (or absorption) as a function of the pump-probe delay time τ . To this end, one fixes the THz sampling time t and scans over pump-probe time τ . Fixing the THz sampling time at two different positions as it is shown in Figure 3.11 allows recording the time evolution of different components of the complex photoconductivity.

In the first, one fixes the sampling time at the maximum amplitude of the probing THz pulse ($t = t_{max}$, Figure 3.11). Next, to achieve a better signal to noise ratio, one measures and compares not the absolute values of the transmitted THz field but rather its change. It is done by using an optical chopper II in the pump beam (see Figure 3.7), while chopper I that modulates THz generation is stopped (or removed). Thus, one measures $\Delta E_{t_{max}}(\tau)$ which is, in the limit of small differential signals, related to the real part of the photoconductivity [63].

A typical 1D scan measured at the peak of probe THz pulse is shown in Figure 3.10. This figure shows two prominent examples of the pump-induced change in THz transmission. It

shows the responses of the high-resistivity silicon and doped CVD-grown graphene. The former has a positive sign (so-called positive photoconductivity) as a result of increased conductivity due to the creation of free charge carriers in the conduction and valence bands. In the latter case, as we will explain later, the photoexcitation changes the thermal distribution of the existent free carriers which leads to the induced THz transparency, i.e., the doped graphene in the photoexcited state is less conductive than the one in the equilibrium (also known as negative photoconductivity). The long-living photoconductivity signal of the silicon reflects the long lifetime of the photoexcited carriers as a result of the indirect band-gap nature of the material, i.e., it is a slow three-body process as the recombination of the carriers involves phonons carrying a necessary momentum. In contrast, graphene recovers its equilibrium within several picoseconds because of the strong coupling of the carriers to phonon modes.

Another way to perform 1D pump-probe scans is by fixing the THz sampling time at the point where the probe field crosses zero ($t = t_{cross}$, Figure 3.11). Given that, near the zero crossing, one can approximate the field as a linear function of time, the value of $\Delta E_{t_{cross}}(\tau)$ measured here is proportional to the delay of the probing THz waveform, and thus to the imaginary component of the conductivity [64].

2D spectroscopy

Measuring 1D dynamics described in the previous section sometimes is not enough to describe the whole response of the system upon photoexcitation. The extension of this method is a so-called 2D scanning, in which one measures not only time-resolved (averaged) THz transmission dynamics but also the full THz pulse thus allowing obtaining the full photoconductivity spectra at every pump-probe delay if it is necessary.

There are several ways to perform these kinds of experiments. Primarily it is defined by the 1D time dynamics. To elaborate on this, we will consider the most relevant cases.

The simplest case is the 2D spectroscopy of the silicon response upon photoexcitation (green line in Figure 3.10). The 1D dynamics shows little time dependence over the picosecond range as it is shown in Figure 3.12. Essentially, we can consider it as a constant. Then to measure the frequency response, one has to fix the pump-probe delay time τ (via delay stage II, Figure 3.7) away from the pump-pulse arrival time and measure the transmitted THz field by sweeping the sampling time t (via delay stage I, Figure 3.7). Similarly, as in the 1D case, one measures not just the transmitted THz pulses but the induced change of the THz pulse by using

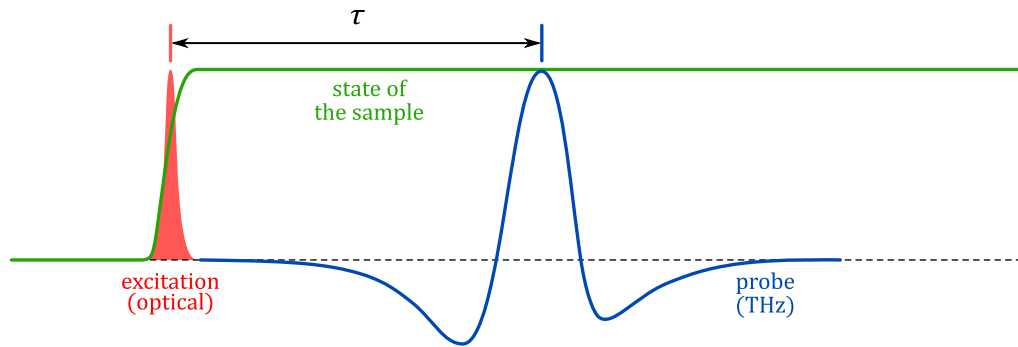


Figure 3.12: The state of the sample does not change on a time scale comparable with the temporal length of the probing THz pulse.

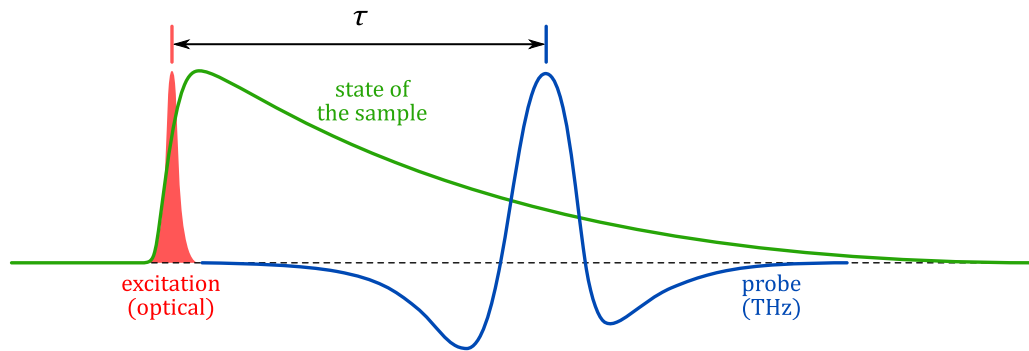


Figure 3.13: The state of the sample changes faster than the length of the probing pulse.

only the optical chopper II in the pump beam, while the chopper I is stopped or removed. This approach increases the signal to noise level and makes possible measuring the THz pulse modulation down to tenths of a percent.

As an example, the photoconductivity spectrum of a thin film on a substrate with a slow photoresponse can be calculated as [65], [66]:

$$\Delta\hat{\sigma}(\omega) = \frac{1 + n_s}{Z_0 d} \cdot \frac{\Delta\hat{E}_{sam}(\omega)}{\hat{E}_{ref}(\omega)} \quad (3.33)$$

Here $\Delta\hat{E}_{sam}(\omega)$ is the Fourier transform of the differential time signal and $\hat{E}_{ref}(\omega)$ is the Fourier transform of the THz probe pulse transmitted through the unexcited sample.

In the case when 1D dynamics evolve in a picosecond range, like for graphene (blue line in Figure 3.10), one cannot measure full response just simply fixing pump-probe delay time and scanning only the sampling beam. The reason for that is that THz pulse itself evolves within

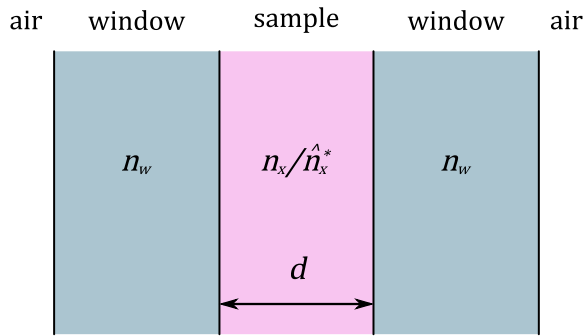


Figure 3.14: Schematic diagram of the optical cuvette with the suspension of photoactive entities (for instance, GNRs in 1,2,4-Trichlorobenzene). The optical pulse excites the sample uniformly

the range of several picoseconds (see Figure 3.13). Thereby the front part (before the maximum of the THz pulse) of the probing THz pulse travels through the sample in the equilibrium while the tail of the pulse at every time goes through the sample with non-constant photoresponse. The detected THz pulse with such a complex history of the sample makes the retrieving of the optical constants extremely complex. This difficulty can be circumvented experimentally as follows. One fixes the relative delay between the optical pump and EO sampling pulses. In the next, THz pulse is recorded by scanning both of the pump (delay stage II) and the sampling pulses (delay stage I) together with respect to the THz pulse. Thereby, the detected THz wave experiences the same pump-probe delay at every point with respect to the pump pulse [66]. We have used the latter approach for all frequency-resolved measurements in optically excited samples presented in this thesis. The conductivity spectrum can be derived following the same procedure and using, for instance, the thin-film formula (Eq. 3.33).

Suspension of photoactive particles in a dielectric liquid.

In this section, we will present the procedure for the photoconductivity spectrum extraction from the 2D experiment on a suspension of photoactive particles in a dielectric liquid. Generally, this procedure can be complicated due to non-uniform excitation profile. In this work, we performed experiments on suspensions of GNRs. To avoid these complications, we kept concentration at values where excitation profile could be treated as homogenous throughout the whole sample depth.

The schematic diagram of the sample is presented in Figure 3.14. The sample is the arrangement of layers with different refractive indices. The THz pulse propagates from the

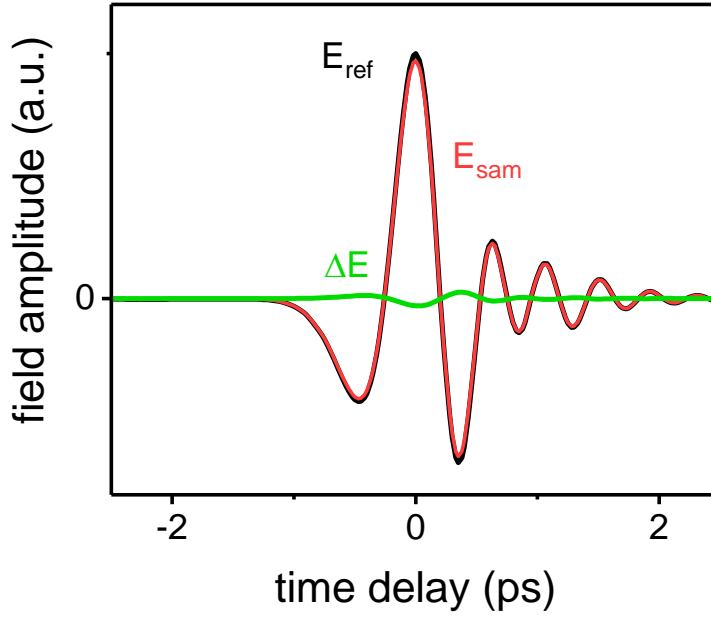


Figure 3.15: Example of the reference signal ($E_{ref}(t)$, black line) transmitted through a material in the equilibrium. The probe signal ($E_{sam}(t)$, red line) transmitted through the same material excited with the optical pulse. The differential signal (green), i.e., $\Delta E(t) = E_{ref}(t) - E_{sam}(t)$. In the OPTP experiment one usually records only $E_{ref}(t)$ and $\Delta E(t)$.

volume of air (refractive index is one) through the first optical window of the cuvette with a refractive index n_w , then the photoactive region of thickness d with the refractive index n_x in the unexcited state and with the refractive index \hat{n}_x^* when it is excited, then it propagates through another window and eventually again into the air. Thereby we can write the ratio of the sample signal to the reference one, i.e., THz probe signal transmitted through the excited and unexcited sample [66]:

$$\hat{T} = \frac{\hat{E}_{sam}}{\hat{E}_{ref}} = \frac{\hat{t}_{wx}^* \cdot \hat{t}_{xw}^*}{t_{wx} \cdot t_{xw}} e^{i(\hat{n}_x^* - n_x)\omega d/c} \quad (3.34)$$

In the unexcited state, it is assumed that the refractive index of sample comes solely from the solvent, thereby we use substitution $n = n_x$. Using equations for Fresnel coefficients (3.21), one can rewrite the latter expression as:

$$\hat{T} = \frac{\hat{E}_{sam}}{\hat{E}_{ref}} = \left(1 + \frac{\Delta\hat{n}}{n}\right) \left(1 + \frac{\Delta\hat{n}}{n_w + n}\right)^{-2} \left(1 + e^{\frac{i\Delta\hat{n}\omega d}{c}}\right) \quad (3.35)$$

Here we have defined $\Delta\hat{n} = \hat{n}_x^* - n_x = \hat{n}_x^* - n$. We expect that the contribution to the refractive index upon photoexcitation comes solely from the photo-carriers in the incursions (i.e., GNRs) while the solvent is photo-inert. In general, the latter expression is a transcendental equation and has to be solved numerically. In practice, we deal with substantially weak refractive index modulations, thus this expression can be simplified via Taylor expansion as

$$\begin{aligned}\hat{T} = \frac{\hat{E}_{sam}}{\hat{E}_{ref}} &\approx \left(1 + \frac{\Delta\hat{n}}{n}\right) \left(1 - 2\frac{\Delta\hat{n}}{n_w + n}\right) \left(1 + \frac{i\Delta\hat{n}\omega d}{c}\right) \approx \\ &\approx 1 + \frac{\Delta\hat{n}}{n} - 2\frac{\Delta\hat{n}}{n_w + n} + \frac{i\Delta\hat{n}\omega d}{c} = 1 + \Delta\hat{n} \left(\frac{n_w - n}{n_w + n} + \frac{i\omega d}{c}\right)\end{aligned}\quad (3.36)$$

In the experiment, one measures not the probe THz pulse transmitted through the excited sample but rather the differential time signal (see Figure 3.15). One does that for the reasons that the actual modulations caused by the photoexcitation could be so subtle that makes it impractical to extract any valuable information from the measured data. Hence, the latter expression transforms into:

$$\hat{T} = \frac{\hat{E}_{sam}}{\hat{E}_{ref}} = \frac{\hat{E}_{ref} + \Delta\hat{E}}{\hat{E}_{ref}} = 1 + \frac{\Delta\hat{E}}{\hat{E}_{ref}} \quad (3.37)$$

where $\Delta\hat{E}$ is the complex valued Fourier transform of the differential time signal. Eventually one can write a linear expression for the induced refractive index as

$$\Delta\hat{n}(\omega) = \left(\frac{n_w - n}{n_w + n} + \frac{i\omega d}{c}\right)^{-1} \frac{\Delta\hat{E}(\omega)}{\hat{E}_{ref}(\omega)} \quad (3.38)$$

This expression can be used now to obtain the complex-valued photoconductivity of the sample. Using expression (3.1) the photoconductivity can be found as a difference between conductivities in the excited and unexcited state:

$$\Delta\hat{\sigma}(\omega) = -(\varepsilon^* - \varepsilon)i\omega\varepsilon_0 = \left(n^2 - (n - \Delta\hat{n}(\omega))^2\right) \frac{i\omega}{Z_0 c} \quad (3.39)$$

Here we used the identity $\varepsilon_0 = 1/Z_0 c$.

Thus, one can extract the complex photoconductivity in a suspension from measured reference THz signal and the photoinduced modulation therein using knowledge of the refractive indices of the cuvette's windows and the solvent.

Chapter 4

Terahertz spectroscopy of graphene

The material presented in this chapter is a result of the combined works of the author with Søren Jensen, Zoltán Mics, Klaas-Jan Tielrooij that have been published in Refs. [67]–[69]. As a part of this work, the author performed 2D THz experiments on graphene as well as retrieved photoconductivities from the measured data. Søren Jensen and Zoltán Mics have performed 1D THz measurements and nonlinear THz studies respectively. Klaas-Jan Tielrooij and Zoltán Mics have done the modeling.

In this chapter, we show that the linear band structure in graphene plays a crucial role in its conductivity dynamics. We introduce a simple thermodynamic model, which can adequately describe the transient conductivity of graphene upon either optical excitation or during its interaction with a high-field THz pulse.

4.1 Terahertz conductivity of graphene

Here we start with describing the conductivity of graphene that appears as an output of THz TDS experiment. In this experiment, the propagating probing THz pulse interacts only with the carriers in graphene with energies around Fermi level – so-called free carrier absorption, thus providing information about conductivity in graphene in the THz frequency range.

We make a little digression here, as it is of importance to discuss graphene samples we studied in this work. One can list three major types of graphene that are usually defined by the production method.

The first one, and probably the historically most important one, is graphene produced using the scotch-tape method (or exfoliation) [2]. This type is the purest possible graphene that could be mechanically transferred to another substrate or even could be freestanding [70]. The first significant discoveries were made particularly on this kind of graphene [4]. The disadvantage

of the scotch-tape graphene, specifically for the THz experiments, is the size of the films, which are usually in the micrometer region or even less. Since the THz measurements are usually performed in the transmission mode where the THz beam is focused on a sample, the size of the material should exceed the focal spot size of the probing beam, which is usually of sub-mm range. Thereby that makes THz spectroscopy challenging if not completely impossible due to these limitations.

Another type is the epitaxial graphene that is obtainable by reducing the silicon on the surface of the silicon carbide [71]. This method produces already large-scale samples (as large as the source silicon carbide substrate), but still, the final product sometimes is a stack of graphene layers. These layers have different properties from layer to layer, as the property of any graphene layer is defined by its vicinity to the substrate, e.g., the chemical composition of a layer eventually reaches that of silicon carbide the closer the layer gets to the substrate [72]. This type of graphene is not transferable. Thus it always comes on the silicon carbide substrate. Despite having a large area, the epitaxial graphene appears to be not the best candidate for the THz experiment as one measures not the single layer of graphene but the stack of layers and the film comes with a photoactive substrate that also places a limitation for the OPTP experiments.

Finally, we come to the last major type, CVD (chemical vapor deposition) graphene that is synthesized from the gas phase on a target substrate [73]. This method provides a large area monolayer of graphene that is easily transferable to another substrate. The CVD graphene on the substrate is usually doped because of interaction with the substrate and the adsorption of the environmental gases [74]. The latter makes this kind of graphene extremely sensitive to the interaction with light that can lead to the carrier concentration change [75]. The carrier concentration could also be tuned in a gated sample where one tunes chemical potential by applying a static voltage between the gate and graphene [2].

In this work, all measurements have been performed on the CVD graphene (provided by the group of Prof. Müllen), since this method allows growing largescale films that are ideally suitable for the THz measurements. Our samples have been transferred on the photoinactive fused silica (or quartz) substrate.

Initially, the free carrier absorption in graphene (or intra-band response) has been measured using broadband Fourier-transform IR spectroscopy (FTIR) [46] in a back-gated sample. It has been proved that the optical conductivity of doped graphene in the THz frequency range indeed

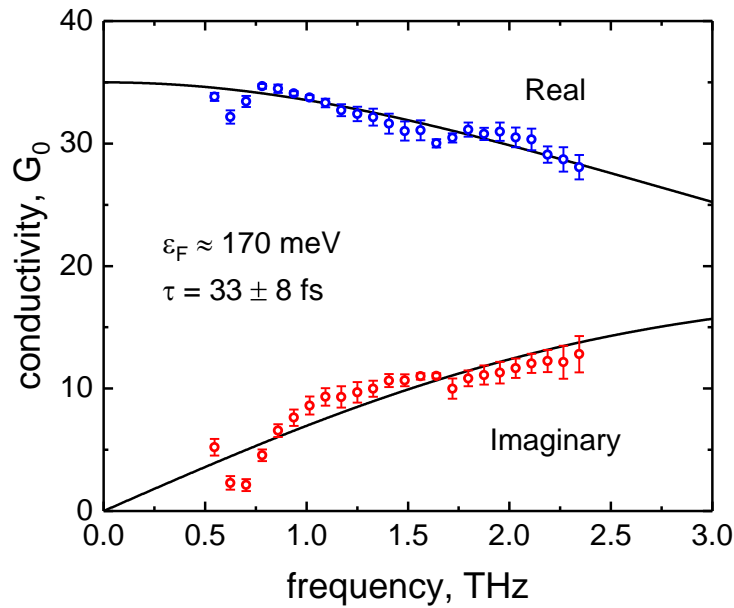


Figure 4.1: The complex-valued conductivity of CVD-grown graphene on the fused silica substrate measured in the units of $G_0 = e^2/4\hbar$. Blue points correspond to real conductivity and red ones to the imaginary one. Lines fit the Drude conductivity (Eq. (2.34)). The sample was covered with the poly(methyl methacrylate) or simply PMMA that normally used as a scaffold for the graphene transfer procedure. The PMMA, in this case, provided some protection from the environment and ‘aging’. Nevertheless, the data show several artifacts around 0.7 THz and 1.7 THz. The former is perhaps due to oscillatory modes in PMMA itself. The latter usually comes from the oscillatory mode in water that is either present in the environment or trapped under the PMMA layer.

follows the Drude form (Eq. (2.34)) together with its square root dependence on the carrier concentration.

Even though the FTIR spectroscopy is a powerful tool, which provides a broad spectral range, it lacks the phase sensitivity as typically only power transmission, or reflection spectra are recorded. In contrast, as it was already stated, the THz-TDS enables phase-resolved measurements of the complex-valued optical conductivity. The first such experiments, probing the free electron conductivity of large-area CVD graphene [76], [77], revealed little spectral dispersion of the conductivity in the range 0.3 – 1.7 THz. Following Eq. (2.34), one can say that this is caused by a very short electron momentum scattering time $\tau = 1/\gamma < 10$ fs, as a result of the influence of defects. Over time, however, the CVD technology has improved, yielding very high-quality samples with electron momentum scattering times on the order $\tau = 10 - 70$ fs [65], [78]–[80], and even as high as $\tau = 140$ fs [68], which corresponds to mean free paths of $\lambda = v_F\tau = 140$ nm. A typical THz conductivity spectrum of a doped CVD-

grown graphene is presented in Figure 4.1, showing an appreciable dispersion of the complex-valued conductivity because of relatively long scattering time $\tau = (33 \pm 8)$ fs. The value has been obtained by fitting the data to the Drude model Eq. (2.34).

The quality of the graphene film plays a foremost role in its conductivity properties, especially in CVD type graphene, since this graphene has inherent artifacts like cracks or wrinkles, which for instance appear during the transfer. Thereby the response can vary from theoretically predicted Drude behavior down to the Drude-Smith one [81], the latter is a signature of the persistent backscattering in the carrier movement.

4.2 Nonlinear terahertz conductivity of graphene — Thermodynamic model

In the THz-TDS experiment on graphene, one probes the linear intra-band response of graphene, and we have shown above that the Drude conductivity well approximates that response. Despite the low photon energy of the THz wave (approximately 4 meV), a THz pulse can carry an immense field strength thus allowing the study of highly nonlinear phenomena. With the advent of sources of intense THz pulses, these kinds of experiments became possible [82]. We avoid the descriptions of these techniques as there are no principle differences in the experimental setup compared to the one introduced in the previous chapter. Moreover, there are plenty of reviews covering this field [83]. The more important subject here is what observations we have obtained in the strong field THz-TDS experiment on graphene and the physical picture we have introduced to describe them.

In the works by Hwang et al. (Ref. [84]) and Paul et al. (Ref. [85]) the interaction of doped graphene with strong THz fields ($E_{THz} > 10$ kV/cm) has been shown to result in a significant ($> 15\%$) THz transmission enhancement. This is the consequence of a reduction of the carrier intra-band conductivity that is taking place in single-layer CVD graphene [85], [86] in the course of the interaction with the strong electric field of a THz pulse. The time-resolved dynamics of this conductivity reduction has been also explored using time resolved THz-pump/THz-probe spectroscopy [84]. Following ref. [84], a high-field THz pump pulse causes a decrease in the conductivity that occurs within approximately 1 ps (essentially the duration of the THz pulse). The induced reduction subsequently recovers within 2 – 3 ps. This conductivity reduction is believed to be a result of the heating of charge carriers by the strong

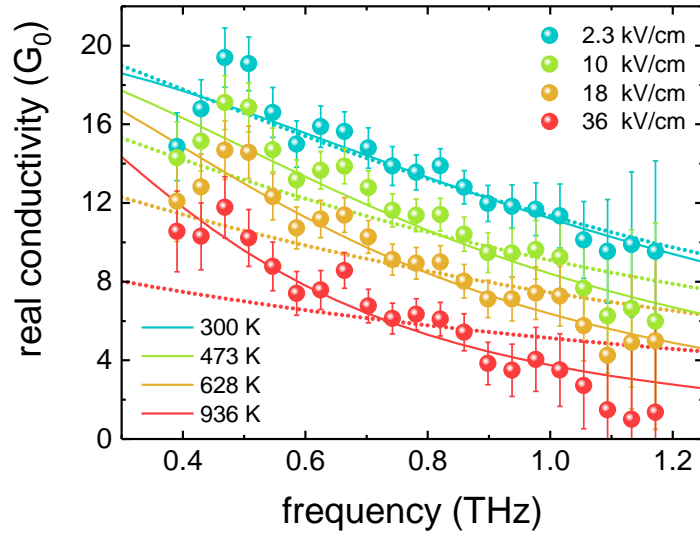


Figure 4.2: Frequency-dependent conductivity spectra of graphene, measured at selected peak THz field strengths in the range of 2.3–36 kV/cm (symbols). The data fit the equation (4.1) (solid lines) at the indicated in the figure temperatures in the assumption of electron momentum scattering only due to long-range Coulomb impurities. The dotted lines correspond to the calculation for the short-range disorder momentum scattering scenario. The error bars are the standard deviations in the measurements. Adapted with permission from *Nat. Commun.* 2015, 6, 7655 [68]. Copyright (2015) Nature Publishing Group.

THz pulses, which resembles that of conventional doped semiconductors [87], [88], which also originates from the intra-band electron heating in strong THz fields. The work by Tani *et al.* (Ref. [89]) supports this picture by observation of decreased optical density of near-IR pulse in CVD graphene excited by the intense THz pulse, which originates from an increased population of high-energy levels by hot electrons. In our lab, we have also observed the THz conductivity reduction in a single layer CVD graphene (see. Figure 4.2) with increasing THz field. In the following, we introduce a fairly simple model that nevertheless well describes the observed conductivity spectra.

We first outline the energy flow in the interaction between the electric field of a THz pulse and the free charge carriers in graphene. The primary energy transfer from the THz pulse to the electronic population in graphene occurs via the conductivity mechanism, as the real part of the conductivity (σ_1) of the material is directly proportional to its power absorption $\alpha = 4\pi\sigma_1\mu_1/nc$ [43]. The incident field E_{THz} acts on the free carriers at the states near the Fermi level and drives a THz current $j = \sigma \cdot E_{THz}$ that initially keeps the transferred energy.

The linear dispersion of electrons near Dirac points facilitates the efficient process of electron-electron scattering as the energy and momentum conservation can be easily fulfilled in the

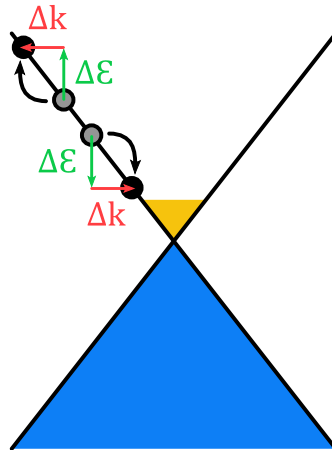


Figure 4.3: Dirac cone showing exchange of energy and momentum of two electrons in the conduction band.

event of scattering [68] (see Figure 4.3). This results in an efficient and fast exchange of energy and momentum within the entire electron population in graphene [90]. The current induced by THz pulse deposits its energy into the electronic system of graphene and sets it out of the equilibrium that is followed by the process of thermalization. Because of the efficient process of electron-electron interaction, thermalization occurs over less than 50 fs [91]–[93], which is much faster than the period of field oscillations in THz pulse (in the range of ~ 1 ps). Hence, the establishment of the thermalized population of carriers in graphene can be considered instantaneous on the picosecond timescale. Therefore, the energy of the THz field coupled to graphene via the conductivity mechanism is quasi-instantaneously converted into the internal energy of the thermalized electron population at elevated temperature T_{el} .

To avoid confusion, the thermalized electron population here refers to one described by the Fermi-Dirac distribution with a specific temperature and chemical potential. The electron distribution, in turn, may be out of thermal equilibrium with the crystal lattice of graphene. The process of establishing the thermal equilibrium between these two systems we refer to as a cooling.

The carrier cooling occurs via phonon emission on a significantly longer (several picoseconds) timescale [94] than the duration of the THz pulse. Thus, the electron system accumulates the internal energy during the interaction of the electric field of the THz pulse with graphene. As a result, the electron population in graphene on the THz timescale can be well described as

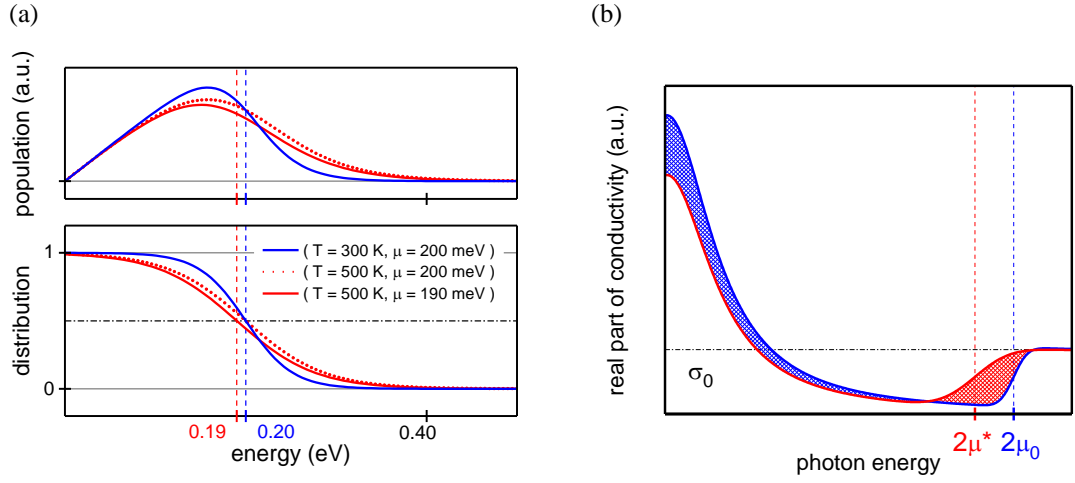


Figure 4.4: The increase of the carrier temperature leads to the decrease of the chemical potential because of constant carrier concentration. (a) Upper plot: comparison of the ‘heated up’ electron populations with the fixed chemical potential (dotted red line) and that satisfying the constant carrier concentration (solid red line), i.e., the area under the blue and red solid curves are equal. Bottom plot: the Fermi-Dirac distributions of the populations shown in the upper plot. (b) The illustration of the resulting decrease of the Drude weight in favor of the opening more inter-band transitions, i.e., conservation of the spectral weight.

thermalized electron gas in which any kind of supplied energy is simply adding to the population of electrons and the Fermi-Dirac distribution $f(\mu, T_{el}, \mathcal{E})$ with the instantaneous temperature T_{el} describing their population at all times. Thereby we can write the expression for the conductivity of graphene with a given temperature of electrons and corresponding chemical potential (by applying transition (2.7) to conductivity from the Boltzmann transport equation (2.31)) as

$$\hat{\sigma}(\omega) = \frac{e^2 v_F^2}{2} \int_0^\infty d\mathcal{E} \cdot g(\mathcal{E}) \cdot \mathcal{E} \cdot \frac{1}{1/\tau(\mathcal{E}) - i\omega} \cdot \left(-\frac{\partial f(\mu, T_{el}, \mathcal{E})}{\partial \mathcal{E}} \right) \quad (4.1)$$

here $\tau(\mathcal{E})$ is the energy-dependent carrier momentum scattering time.

Before the excitation by the THz pulse, the carriers in graphene are in the thermal equilibrium with the environment. Thus, the Fermi distribution at room temperature (T_0) describes the population of electrons in graphene. All experiments discussed in this work were performed at the room temperature unless it is otherwise stated. After the interaction with the THz pulse, the distribution of carriers changes as the carrier temperature elevates. The THz excitation of the carrier system is then accounted for by simply adding a portion of heat δQ (absorbed from the THz field) to the internal energy of the electron gas. One writes this as:

$$W_0 + \delta Q = \int_0^{\infty} d\mathcal{E} \cdot g(\mathcal{E}) \cdot \mathcal{E} \cdot f(\mu^*, T^*, \mathcal{E}) \quad (4.2)$$

where $W_0 = \int_0^{\infty} d\mathcal{E} \cdot g(\mathcal{E}) \cdot \mathcal{E} \cdot f(\mu_0, T_0, \mathcal{E})$ is the internal energy of the carrier system at room-temperature prior to the interaction with the THz field. This condition, in conjunction with the conservation of carrier density in the conduction band, i.e.,

$$N_0 = \int_0^{\infty} d\mathcal{E} \cdot g(\mathcal{E}) \cdot f(\mu_0, T_0, \mathcal{E}) = \int_0^{\infty} d\mathcal{E} \cdot g(\mathcal{E}) \cdot f(\mu^*, T^*, \mathcal{E}), \quad (4.3)$$

importantly implies that the chemical potential decreases with increasing carrier temperature and concomitant broadening of the Fermi-Dirac energy distribution of the carriers, as illustrated in the left of Figure 4.4. The downshift of the chemical potential with increasing electronic temperature results in an increase of the amount of optically active inter-band transitions with energies $\hbar\omega > 2\mu^*$ (see Figure 2.3) that were Pauli-blocked (since $\mu_0 > \mu^*$) at room temperature before the interaction with the THz pulse. Because the total spectral weight must remain constant [46], the increased number of the *inter-band* transitions leads to the decrease of the weight of *intra-band* absorption, which contributes to the THz conductivity of graphene, as illustrated in the right of Figure 4.4. Thus, the downshift in chemical potential at elevated electronic temperatures, and constant carrier density qualitatively explains the experimental observations of lower THz conductivity in graphene at stronger THz fields.

For a quantitative description of the measured THz conductivity spectra shown in Figure 4.2, we directly apply equation (4.1) within the constraint of carrier density conservation (4.3) (yielding the chemical potential μ at a given temperature as explained above), and use the electronic temperature T_{el} as a free fit parameter. At this point, not only the temperature-dependent electron distribution, but also the energy dependence of the momentum scattering time $\tau(\mathcal{E})$ should be considered.

As discussed in detail in [16] and references therein, the carrier scattering in graphene may occur according to two main energy-dependent scenarios. One scattering regime is long-range scattering at Coulomb impurities, where the carrier scattering time τ is proportional to its energy E , $\tau = \alpha E$. Another one is short-range scattering at disorder sites, which is characterized by the inverse dependence of scattering time on carrier energy, $\tau = \beta/E$. The former is the predominant scattering mechanism for a CVD-grown graphene, whereas the

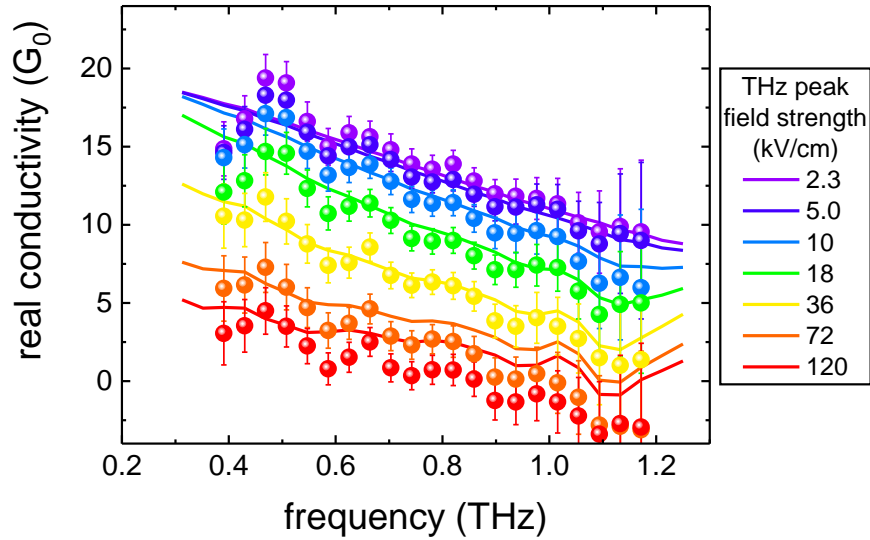


Figure 4.5: The measured conductivity spectra of graphene (symbols) at different peak field strengths, along with the corresponding modeling (lines) based on the time-dependent thermodynamic balance in graphene described in the text. The error bars are the standard deviations in the measurements. Adapted with permission from *Nat. Commun.* 2015, 6, 7655 [68]. Copyright (2015) Nature Publishing Group.

latter is predominant in (encapsulated or suspended) exfoliated graphene [16]. The proportionality constants, α and β , can be readily established experimentally as $\alpha = \tau_0/\mu_0$ and $\beta = \tau_0 \cdot \mu_0$ [68] from the linear characterization of graphene at room temperature (here τ_0 and μ_0 correspond to carrier scattering time and chemical potential at room temperature). Nevertheless, we note that the argument of conservation of the total spectral weight described above demonstrates that precise knowledge of energy dependence of momentum scattering time in graphene is not essential for predicting the observed reduction of strong-field THz conductivity in graphene.

The direct application of (4.1) (in the scenario of long-range Coulomb scattering) is in quantitative agreement with the measured conductivities for the field strengths up to ~ 40 kV/cm, with the carrier temperature has been taken as a free fitting parameter [68]. In this case, peak electron temperatures of ~ 1000 K were associated with THz field strength of ~ 40 kV/cm. We note that this temperature is close to the typical Fermi temperature of graphene sample used in the experiment [68].

For the stronger fields, however, the quasi-static, weakly perturbative description given by (4.1) is no longer appropriate, and a full time-dependent treatment of conductive response of

graphene is necessary. We have employed a split-step time-domain approach [68], similar to the one used in nonlinear optics [95] that takes into account the dynamics of the electron heating (instantaneous) and its cooling (retarded [92], [93]) throughout the interaction of the THz field with graphene (see Appendix 4.A).

As a result, the entirety of experimental data, taken at all field strengths 2.3 – 120 kV/cm, and in the entire frequency range up to 1.2 THz, has been reproduced without using any adjustable parameters, as shown in Figure 4.5 [68].

As one can see in Figure 4.5, for the frequencies above > 1 THz, and THz peak fields of ~ 100 kV/cm, the conductivity of graphene almost entirely vanishes, while the calculations evidence the peak electron temperatures exceeding 7000 K for the strongest fields used. A comparison between experiments and the theory reveals that, on the timescale of graphene — THz interaction of 1.5 – 2.0 ps, about 15% of absorbed THz energy is retained as electronic heat, lowering the chemical potential and reducing the intra-band conductivity of graphene, whereas the rest of the absorbed THz energy is spent on the emission of phonons [68].

4.3 Photoconductivity of graphene — thermodynamic model

In the previous section, the intra-band excitation of carriers in doped (CVD) graphene with intense THz pulses has been shown to lead to a reduction of intra-band graphene conductivity. A similar effect has been observed for doped graphene after inter-band excitation with ultra-short optical pulses [47], [65], [67], [79], [80], [86], [94], [96] using optical pump – THz probe spectroscopy. In a typical semiconductor [1] the photoconductivity is positive, i.e., it becomes more conductive upon an optical excitation that creates extra free carriers in the conduction and valence bands. The photoconductivity of doped graphene is negative, i.e., the conductivity of graphene reduces as a consequence of the photo-excitation [65], [67]. See for instance Figure 3.10 showing the negative photoconductivity dynamics (i.e., evolution in time) of graphene and the positive one of silicon. The reason for this is similar to the case of THz excitation of graphene that we have discussed above in the text. It is the effective redistribution of energy from photo-excited electrons and holes to initially unexcited free (intra-band) electron population, leading to its heating [94].

In work by Jensen et al [67], we have studied the ultrafast carrier-energy relaxation in CVD graphene using OPTP spectroscopy. We have used two types of samples. The first sample is

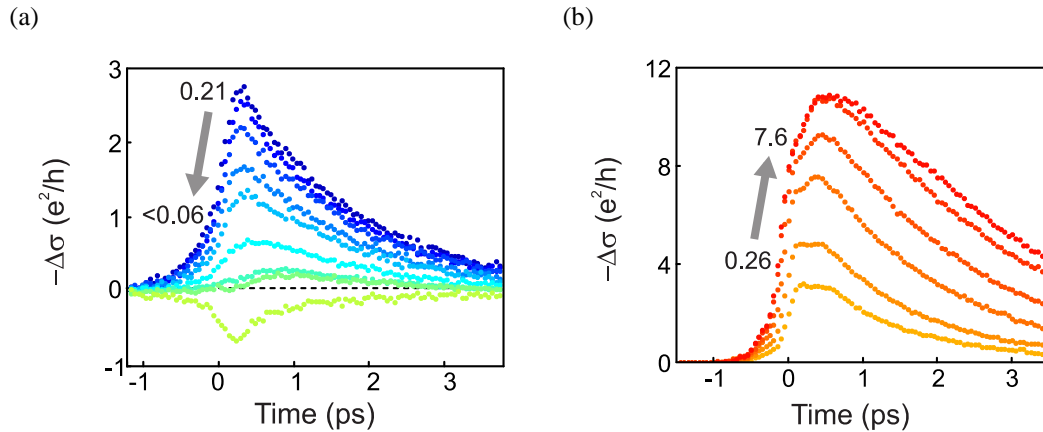


Figure 4.6: Photoconductivity dynamics dependence on Fermi level and fluence. (a) The photoconductivity for different Fermi level (sample with controllable Fermi level). The photoconductivity is negative for all traces, except for the one closest to the Dirac point, where it is positive. (b) The photoconductivity for excitation with 800 nm light at different excitation powers, corresponding to absorbed photon densities from 0.26 to 7.6×10^{12} photons/cm² (sample with fixed Fermi level). The photoconductivity is negative and increases for increasing excitation power. Adapted with permission from *Nano Lett.* 2014, 14, 5839–5845 [67]. Copyright (2014) American Chemical Society.

a CVD graphene with an area of 1 cm² transferred onto a substrate that consists of slightly doped silicon, covered by a 300 nm thick insulating layer of SiO₂. The silicon serves as a backgate allowing the control of the carrier concentration in the graphene sheet, i.e., Fermi level from 0.3 eV down to ~ 0.06 eV. The second sample consists of a CVD grown graphene with an area of a square inch transferred onto quartz with fixed Fermi level of < 0.15 eV.

At first, we have studied the photoconductivity dynamics (1D OPTP experiment) in the sample with controllable chemical potential as a function of carrier concentration, and in the sample with fixed chemical potential as a function of the fluence of exciting optical pulse [67]. The observed dynamics are similar to the one introduced in Figure 3.10 in both samples and show negative photoconductivity. The observed maximal amplitude of the negative photoconductivity in the first sample decreases with the decreasing chemical potential and in the second sample (with fixed Fermi level), it increases with increasing optical excitation fluence (see Figure 4.6 (b)).

We note, that in the first sample with very low chemical potential (~ 0.06 eV) photoconductivity dynamics changes from negative to positive as it is shown in Figure 4.6 (a). This is typical behavior for the intrinsic graphene with the chemical potential near the Dirac point. In the intrinsic graphene, the electrons and holes, created by the optical excitation in the

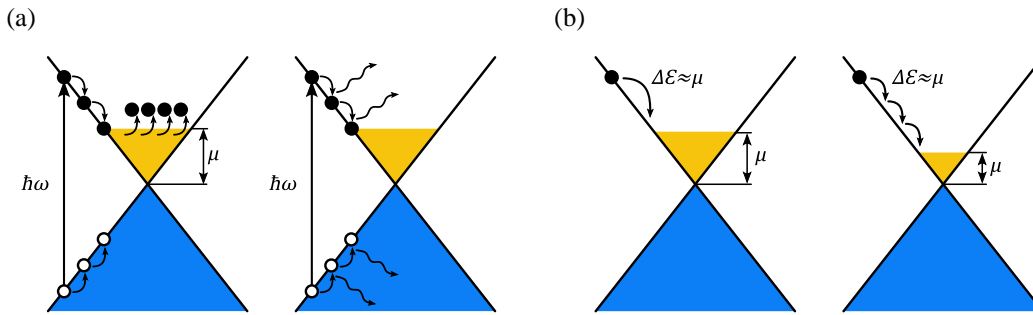


Figure 4.7: (a) The diagram of possible energy dissipation channels of photo-excited carriers in doped graphene that occur either via carrier-carrier interaction or by emitting optical phonons. (b) The comparison of carrier-carrier scattering processes for two different chemical potentials. The relaxation time increases for the case of lower chemical potential μ since more scattering events are required for the carriers to complete their energy relaxation cascade.

conduction and the valence bands, increase the total amount of conductive carriers, thus leading to the increased conductivity – positive photoconductivity. While in the doped graphene, the same electron-hole pairs transfer their energy to the electron population in the conduction band, thus leading to the state with an elevated electron temperature wherein the total amount of carriers in the conduction band is conserved. As we have already pointed out this state has reduced conductivity – negative photoconductivity.

The peak negative photoconductivity in Figure 4.6 corresponds to a state with elevated carrier temperature. The system reaches this state as follows. The absorbed photon creates initial electrons and holes in the conduction and the valence band correspondingly. This unbalanced state of carrier population reaches quasi-equilibrium via two main processes: (i) carrier-carrier scattering and (ii) optical phonon emission (see Figure 4.7 (a)). The equilibration takes place during the first few hundred femtoseconds after photoexcitation, that is, during the rise of the conductivity change. Figure 4.8 shows the normalized photoconductivity signals for this time window. The rise dynamics exhibit a peculiar effect: upon decreasing the chemical potential (i.e., the intrinsic carrier density) or increasing the optical excitation fluence (i.e., the density of primary excited carriers), the signal reaches its maximum at increasingly later times.

The slowing down of the energy dissipation process of photoexcited carriers with decreasing chemical potential is consistent with energy dissipation via intraband carrier-carrier scattering (see Figure 4.7 (b)). Photoexcited carriers relax by exchanging energy with an intrinsic population of the carriers in the conduction band that eventually leads to the increase of its temperature. Levitov has shown in his work [97] that the probability of a single carrier-carrier scattering event is the highest when the exchange energy (between a photoexcited carrier and

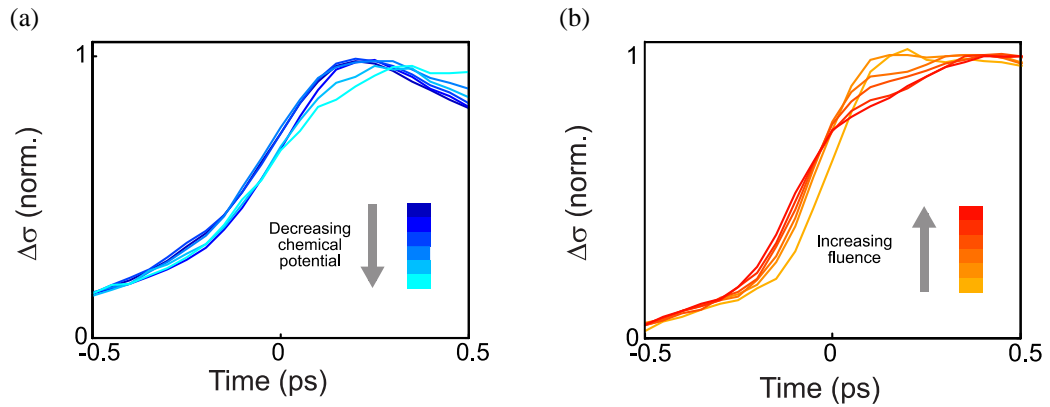


Figure 4.8: (a) The photoconductivity normalized to the peak of the signal (sample with controllable Fermi level), showing that decreasing the Fermi level leads to slower rise dynamics. (b) The photoconductivity normalized to the peak of the signal (sample with fixed Fermi level), showing that increasing the excitation power leads to slower rise dynamics. Adapted with permission from *Nano Lett.* 2014, 14, 5839–5845 [67]. Copyright (2014) American Chemical Society.

a carrier of the intrinsic population in the conduction band) amounts to the value of chemical potential μ . This results from the competition between the available phase space that increases with exchange energy and the coulomb interaction that decreases with the recoil momentum [97]. Thereby, if μ decreases then more scattering events are required for the photoexcited carriers to complete their energy dissipation cascade. This results in an increased relaxation time. Other channels of energy dissipation are expected to start contributing to the overall relaxation process of carriers if the energy dissipation via carrier–carrier scattering would slow down that much that its rate becomes comparable to the rate of other dissipation channels. This would lead to a decrease in the fraction of energy that is transferred to the electron system.

To quantify the fraction of absorbed energy that leads to carrier heating, i.e., heating efficiency, we compare THz photoconductivity data with the results of the thermodynamic model that we have introduced in the previous section.

To calculate the hot carrier temperature, we use the same concept that before photoexcitation there is a known amount of internal energy in the carrier system:

$$W_0 = \int_0^{\infty} d\varepsilon \cdot g(\varepsilon) \cdot \varepsilon \cdot f(\mu_0, T_0, \varepsilon) \quad (4.4)$$

and a known number of carriers in the conduction band:

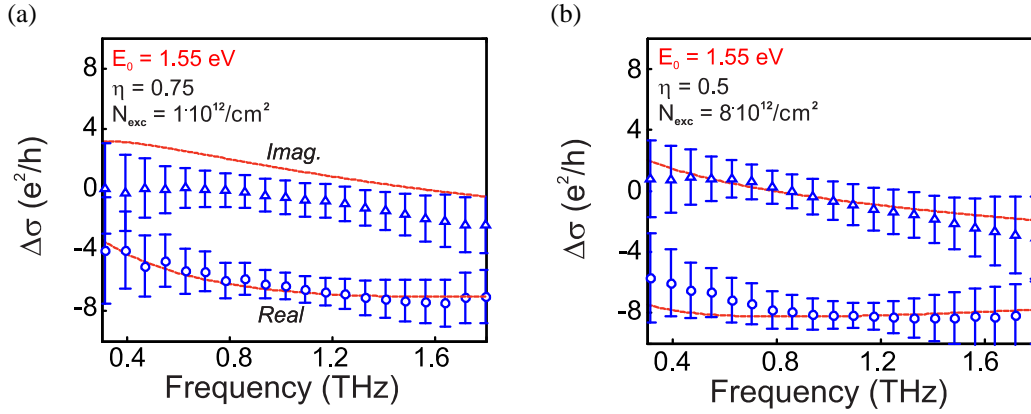


Figure 4.9: Comparison of experimental and theoretical photoconductivity. (a) The complex photoconductivity of the sample with fixed Fermi energy as a function of frequency for an excitation fluence corresponding to $N_{\text{exc}} = 1 \times 10^{12}$ carriers/cm², together with the model result with a carrier heating efficiency of $\eta = 0.75$. (b) The complex photoconductivity of the sample with fixed Fermi energy as a function of frequency for an excitation fluence corresponding to $N_{\text{exc}} = 8 \times 10^{12}$ carriers/cm², together with the model result with a carrier heating efficiency of $\eta = 0.5$. This shows that in this regime other energy relaxation channels contribute to the ultrafast energy relaxation. Adapted with permission from *Nano Lett.* 2014, 14, 5839–5845 [67]. Copyright (2014) American Chemical Society.

$$N_0 = \int_0^{\infty} d\varepsilon \cdot g(\varepsilon) \cdot f(\mu_0, T_0, \varepsilon) \quad (4.5)$$

Because of optical excitation, an amount of energy $\mathcal{E}_{\text{abs}}^{\text{opt}}$ is absorbed in the graphene and a fraction η of this energy ends up in the electronic system through intraband carrier–carrier scattering. After intraband heating is complete, the system is then described by the following set of equations:

$$W^* = W_0 + \eta \mathcal{E}_{\text{abs}}^{\text{opt}} = \int_0^{\infty} d\varepsilon \cdot g(\varepsilon) \cdot \varepsilon \cdot f(\mu^*, T^*, \varepsilon) \quad (4.6)$$

$$N^* = N_0 = \int_0^{\infty} d\varepsilon \cdot g(\varepsilon) \cdot f(\mu^*, T^*, \varepsilon)$$

Here μ^* and T^* are the chemical potential and the carrier temperature in the hot state, respectively. The solution of the equations (4.6) shows that the carrier temperature increases and the chemical potential decreases upon photoexcitation, essentially repeating the results we have obtained in the experiment with high field THz pulses. The photoinduced increase of carrier temperature and the associated decrease in chemical potential have been also explicitly

confirmed by mapping the carrier distribution using time- and angle-resolved photoemission spectroscopy (ARPES) in work by Gierz I. et al. [92].

The hot carrier distribution, with μ^* and T^* calculated using the carrier heating model, directly leads to negative THz photoconductivity (see the previous section). Using the general expression for the general complex conductivity in graphene (4.1), we then can calculate frequency resolved photoconductivity as a difference between conductivities of graphene in the ‘hot’ state and the ‘cold’ state, that is, $\Delta\hat{\sigma}(\omega) = \hat{\sigma}(\omega, \mu^*, T^*) - \hat{\sigma}(\omega, \mu_0, T_0)$. The former corresponds to the state at the peak of photoconductivity dynamics when the carrier system of graphene reaches quasi-equilibrium and the Fermi distribution with μ^* and T^* (obtained from (4.6)) describes its state. The latter state corresponds to graphene, prior to the optical excitation, at the room temperature of T_0 and chemical potential μ_0 . For the conductivity calculations, we use a similar assumption of the scattering time dependence on the energy as we did in the previous section, namely, we assume that scattering time is determined by charged impurity scattering and increases linearly with the energy \mathcal{E} , that is $\tau(\mathcal{E}) = \alpha \cdot \mathcal{E}$ [16], [98]. To estimate the value of the proportionality constant α , we firstly evaluate the carrier scattering time τ_0 at the room temperature by fitting the Drude model (Eq. (2.34)) to the experimental data for the background THz conductivity of graphene obtained using THz-TDS. Then one simply calculates α by dividing the scattering time τ_0 by the chemical potential μ_0 ($\alpha = \tau_0/\mu_0$). The latter we estimate using Raman spectroscopy as $\mu_0 = 0.155 \text{ eV}$ [99]. We thus estimate a scattering time proportionality constant in the sample with the fixed chemical potential to be $\alpha = 200 \text{ fs/eV}$.

We compare the predictions for the frequency-resolved photoconductivity $\Delta\hat{\sigma}(\omega)$ with the experimental results for the sample with fixed Fermi energy. In Figure 4.9(a), we show this comparison for an excitation fluence of $\sim 12 \mu\text{J}/\text{cm}^2$ (a pump wavelength of 800 nm), which correspond to the $N_{exc} = 1 \times 10^{12}$ absorbed photons per cm^2 , and find good agreement with a heating efficiency of $\eta = 0.75$. The small discrepancies between data and model can be ascribed to artifacts that arise from the temporal change of the photoconductivity during the interaction with the THz pulse, [28] although we largely avoid these by moving the optical pump delay line simultaneously with the THz probe delay line (see section 3.2.2).

In Figure 4.9(b), we provide a similar comparison in the *high fluence* regime with $N_{exc} = 8 \times 10^{12}$ absorbed photons per cm^2 that corresponds to the excitation fluence of $\sim 100 \mu\text{J}/\text{cm}^2$. Here we find that we can only describe the data with a significantly reduced carrier heating

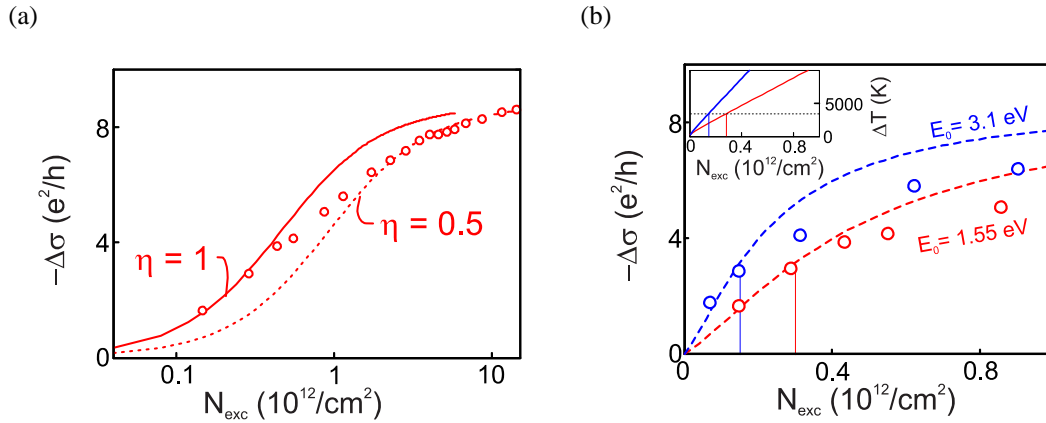


Figure 4.10: Carrier heating efficiency–dependence on fluence. (a) The peak photoconductivity of the sample with fixed Fermi energy for a large range of excitation powers and an excitation wavelength of 800 nm together with the model with $\eta = 1$ (solid line) and heating efficiency of $\eta = 0.5$ (dotted line). (b) The peak photoconductivity of the sample with fixed Fermi energy as a function of excitation power (N_{exc}) for excitation with 800 nm light and 400 nm light. The dashed lines correspond to the model with the same parameters as in a, using $\eta = 1$. The model describes the data well up to $N_{\text{exc}} = 0.3 \times 10^{12}$ carriers/cm² for 800 nm excitation and up to $N_{\text{exc}} = 0.15 \times 10^{12}$ carriers/cm² for 400 nm excitation. The inset shows the carrier temperature that is reached after excitation and thermalization by carrier–carrier scattering, reaching ~ 4000 K before heating becomes less efficient, for both excitation wavelengths. Adapted with permission from *Nano Lett.* 2014, 14, 5839–5845 [67]. Copyright (2014) American Chemical Society.

efficiency of $\eta \approx 0.5$ while keeping the chemical potential μ_0 and scattering time proportionality constant α the same as in the low fluence regime. Together, these results show that at sufficiently low fluence, a larger fraction of the absorbed energy ends up in the electron system, that is, the ultrafast energy relaxation occurs through efficient carrier–carrier scattering. However, upon increasing the fluence (i.e., the carrier temperature), the relative amount of energy transferred to the electron system decreases, which means that carrier–carrier scattering becomes less efficient and other relaxation processes start to contribute.

The overall agreement between data and model shows that the observed negative THz photoconductivity of intrinsically doped graphene [47], [65], [74], [79], [94], [96] can be fully reproduced by considering intraband carrier heating, which reduces the averaged conductivity of the intrinsic carriers, for example energy relaxation via the emission of acoustic phonons..

To determine in more detail how the carrier heating efficiency depends on the excitation fluence, we study the peak photoconductivity of the sample with fixed Fermi energy for a large range of excitation powers for both 800 and 400 nm excitation. We show the

photoconductivity at the peak (when the ultrafast energy relaxation is complete) in Figure 4.10a,b, together with the results of the carrier heating model for the same parameters as in Figure 4.7a and a frequency of 0.7 THz. For low fluences (up to $\sim 4 \mu\text{J}/\text{cm}^2$, corresponding to $N_{exc} \sim 0.3 \times 10^{12}$ absorbed photons/ cm^2 , 800 nm excitation, $\sim 2\%$ absorption) the experimental data are in agreement with the heating model with a fixed heating efficiency of $\eta = 1$. Interestingly, at fluences above $\sim 4 \mu\text{J}/\text{cm}^2$ the experimental photoconductivity starts saturating and the model is only in agreement for a heating efficiency that gradually decreases to $\sim 50\%$ for the highest fluences applied here (Figure 4.10a). These observations suggest that once a certain carrier temperature (~ 4000 K, see inset Figure 4.10b) is reached, the heating efficiency decreases. Interestingly, the experimental data for excitation with 400 nm light start deviating from the model (with efficiency $\eta = 1$) at $N_{exc} \sim 0.15 \times 10^{12}$ absorbed photons/ cm^2 (Figure 4.10b), instead of $\sim 0.3 \times 10^{12}$ absorbed photons/ cm^2 in the case of excitation with 800 nm light. This is because each 400 nm photon has twice the energy of a 800 nm photon. Thus, in both cases, the carrier heating efficiency starts decreasing around the same carrier temperature.

Comparing the data and the heating model leads to the following physical picture of the ultrafast energy relaxation in graphene: until a certain carrier temperature is reached (~ 4000 K), the ultrafast energy relaxation is dominated by carrier–carrier scattering, which leads to efficient and fast (~ 100 fs) carrier heating. Once this carrier temperature is reached, the relaxation slows down and the carrier heating efficiency decreases, as ultrafast energy relaxation occurs through additional pathways involving optical phonon emission [100]. The reduction in heating efficiency that follows from the macroscopic heating model can be explained using the microscopic picture of intraband carrier–carrier scattering [94], [97]. At increased electron temperatures, the quasi-equilibrium chemical potential decreases, which means that the electronic heat capacity decreases. It furthermore implies that the amount of energy that is exchanged in intraband carrier–carrier scattering events ($\sim \mu$) decreases. Therefore, the energy relaxation of a photoexcited carrier requires an increasing number of intraband carrier–carrier scattering cascade steps. Thus, for an increasing carrier temperature, energy relaxation through intraband carrier heating slows down.

4.4 Conclusions

In this chapter, we have covered the THz spectroscopy of graphene and presented a simple thermodynamic picture that qualitatively and quantitatively describes the nonlinear THz conductivity and photoconductivity of doped CVD graphene. Within this picture, the energy of a THz [68] or an optical [67] signal is efficiently and quasi-instantaneously converted into the thermal energy of the entire graphene carrier population, which acts as thermalized fermion gas (within the sub-picosecond timescale) in or out of equilibrium with the lattice. The condition of energy and particle number conservation leads to the decrease of the chemical potential of graphene with increasing electron temperature, reducing its intra-band, THz conductivity.

4.A Appendix: Numerical propagation of terahertz pulse through graphene

Zoltán Mics has developed the approach presented in this section. The numerical propagation of the incident THz pulse through graphene on the substrate provides the transmitted waveform $E_{trans}^{calc}(t)$, from the known reference waveform $E_{ref}^{exp}(t)$. One obtains the latter performing TDS experiment on the substrate without graphene (see Section 3.2.1). Then, by performing Fourier transform on those waveforms, one obtains the nonlinear conductivity using the Tinkham formula, i.e.,

$$\hat{\sigma}(\omega) = \frac{1 + n_s}{Z_0} \left(\frac{\hat{E}_{ref}^{exp}(\omega)}{\hat{E}_{trans}^{calc}(\omega)} - 1 \right) \quad (4.7)$$

In the following, we will introduce an algorithm to calculate $E_{trans}^{calc}(t)$ numerically.

Given the fact, that graphene film is very thin and conductive, the complex-valued transmission function of the graphene layer is [62], [68]:

$$\hat{t}(\omega) = \frac{2}{1 + n_s + Z_0 \hat{\sigma}(\omega)} \quad (4.8)$$

The transmitted waveform is the convolution of the response function of the sample and the reference waveform:

$$E_{trans}(t) = \frac{(1 + n_s)^2}{4n_s} \int_0^{\infty} T(t') E_{ref}(t - t') dt' \quad (4.9)$$

where $T(t)$ is the inverse Fourier transform of the complex transmission function $\hat{t}(\omega)$ (4.8). Note that $\hat{t}(\omega)$ depends on $\hat{\sigma}(\omega)$ that is subjected to change over the course of interaction of incident THz waveform and graphene due to the absorbed heat δQ by the carriers from the THz pulse. The heat (i.e., the internal energy of electrons) also evolves during the THz-pulse/graphene interaction process. To calculate this function, the balance between instant heating and slow heat dissipation has to be accounted. To this end, we evaluate the following convolution:

$$\begin{aligned} \delta Q(t) = & \int_0^{\infty} R(t') \cdot \left(E_{ref}^2(t - t') - n_s E_{samp}^2(t - t') \right. \\ & \left. - [E_{samp}(t - t') - E_{ref}(t - t')]^2 \right) dt' \end{aligned} \quad (4.10)$$

where $R(t)$ describes the dynamics of the heat dissipation from the carriers and the expression in the parentheses is the absorbed THz energy as a difference between the energy of the incident THz waveform and that of the reflected and transmitted one.

Based on the carrier cooling characterization in work by Gierz [92], we adopt a phenomenological expression of the excess heat dissipation from the carrier system as

$$R(t) = 0.54 \cdot \exp\left(-\frac{t}{0.1}\right) + 0.46 \cdot \exp\left(-\frac{t}{0.92}\right) \quad (4.11)$$

Here t is a time in picoseconds. We note that these cooling dynamics likely correspond to a combination of hot electrons coupling to graphene optical phonons (the sub-picosecond component) and impurity-assisted super-collision cooling via acoustic phonons of graphene [101]–[103], and/or energy flow to the substrate [104] (the picosecond component).

To solve the system of equations (4.9) and (4.10) we yet have to find the expression for $T(t)$. The explicit use of Boltzmann conductivity (4.1) in the expression for $\hat{t}(\omega)$ makes the inverse Fourier transform incredibly difficult, given that change of the chemical potential and the scattering time evolves in time with the absorbed heat. Thereby we parameterize the conductivity (4.1) with the analytical expression (Drude formula) that is a function of absorbed heat Q :

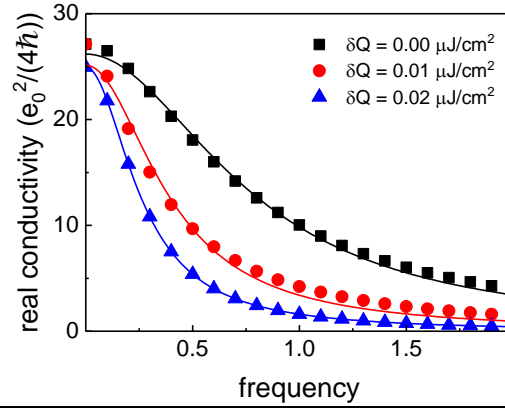


Figure 4.11: The calculated conductivity spectra of a heated carrier system using (4.1) fitted by an empirical effective Drude model (4.12). The numerically calculated hot carrier conductivity perfectly follows the Drude model. δQ is the amount of heat deposited in the carrier population.

$$\sigma(\omega, Q) = \frac{\sigma_{DC}(\delta Q)}{1 - i\omega \cdot \tau_{eff}(\delta Q)} \quad (4.12)$$

To find expressions for $\sigma_{DC}(\delta Q)$ and $\tau_{eff}(\delta Q)$ we calculate several conductivities for a variety of absorbed portions of heat δQ using equations (4.1) – (4.3) (in the assumption of long-range Coulomb scattering, i.e., $\tau(\mathcal{E}) = \alpha \cdot \mathcal{E}$) and fit obtained results with Drude formula. These results are presented in the Figure 4.11. We note that conductivity $\sigma_{DC}(\delta Q)$ at the zero frequency has very weak dependence (Figure 4.11) on the heat that is straightforward to prove analytically by calculating σ_{DC} from the expression (4.1) by setting $\omega = 0$:

$$\sigma_{DC} = \frac{e^2 v_F^2}{2} \int_0^{\infty} d\mathcal{E} \cdot g(\mathcal{E}) \cdot \mathcal{E} \cdot \tau(\mathcal{E}) \cdot \left(-\frac{\partial f(\mu, T_{el}, \mathcal{E})}{\partial \mathcal{E}} \right) = e^2 v_F^2 \alpha N_0 = const \quad (4.13)$$

Here we used integration by parts and the fact that the density of states and the scattering time are both proportional to the energy \mathcal{E} .

For the dependence of the scattering time on the added heat, we found empirically from our simulations that the effective scattering time of the hot carriers depends linearly on the amount of heat δQ added to the system.

$$\tau_{eff}(Q) = \tau_0 + \delta Q \cdot 20000 \left[\frac{\text{fs} \cdot \text{cm}^2}{\mu\text{J}} \right] \quad (4.14)$$

By substituting the obtained parametrized Drude expression into the complex transmission function, we finally obtain the expression for the time-dependent response function of graphene as:

$$T(t) = \frac{2}{n_s + 1} \delta(t) - \frac{2Z_0\sigma_{DC}}{(n_s + 1)^2\tau_{eff}(t)} \exp\left(-\frac{Z_0\sigma_{DC} + n_s + 1}{n_s + 1} \cdot \frac{t}{\tau_{eff}(t)}\right) \quad (4.15)$$

Where $\delta(t)$ is the Dirac delta function and $\tau_{eff}(t)$ depends on time via $\delta Q(t)$.

Now, to calculate $E_{trans}^{calc}(t)$, we split the time interval of $E_{ref}^{exp}(t)$ by the time step dt . Then we evaluate $E_{trans}^{calc}(t)$ at every point t_i of this time interval following the next iterative steps:

1. At the very start ($t_i = 0$) we set $\delta Q_i = \delta Q(t_i)$ to zero.
2. Using the value of δQ_i we calculate the time dependent response function $T(t)$ (4.15).
3. We calculate $E_{trans}^{calc}(t)$ using the convolution (4.9) in the interval $(t_i, t_i + dt)$
4. We calculate average $\delta Q(t)$ for $t \in (t_i, t_i + dt)$ from expression (4.10)

By repeating steps 2 to 4, one can gradually calculate both $E_{trans}^{calc}(t)$ and $\delta Q(t)$. We used typically $dt = 0.5$ fs for the time step.

Chapter 5

Terahertz spectroscopy of mesostructured graphene — GraFold printing

The material presented in this chapter is a result of the combined work of several institutions that have been published in Ref. [105].

In CVD graphene owing to its atomically thin nature, folds occur spontaneously [106], [107]. They have sub-lithographic widths and macroscopic lengths, and can locally affect the electronic structure of graphene. For instance, owing to the symmetry breaking in the honeycomb lattice of graphene, folding can enhance the spin-orbit coupling in the vicinity of the fold thus leading to pseudomagnetic fields [108], [109]. Bending of the lattice in the fold also results in the re-hybridization of the sp^2 bonds (that are forming the structure of graphene) leading to the local formation of sp^3 bonds, which enables the covalent chemistry on the usually unreactive graphene surface [110], [111]. A controlled folding thus could allow the employment of these kinds of effects for technological advantage.

In this chapter, we introduce the controlled graphene folding process that induces periodic well-aligned folds on the surface of the CVD graphene. The group of Prof. G. Duesberg in the Trinity College (Dublin) has developed this method, so-called GraFold printing. We also show how these folds impact the carrier transport in graphene using THz spectroscopy.

5.1 Description of the sample — GraFold printing

The samples have been made in Trinity College Dublin by Toby Hallam. In this section, we will describe the procedure of the sample preparation as well as some characterization that has been done prior to the THz experiments in Mainz. The team of Trinity College has obtained the results presented in this section.

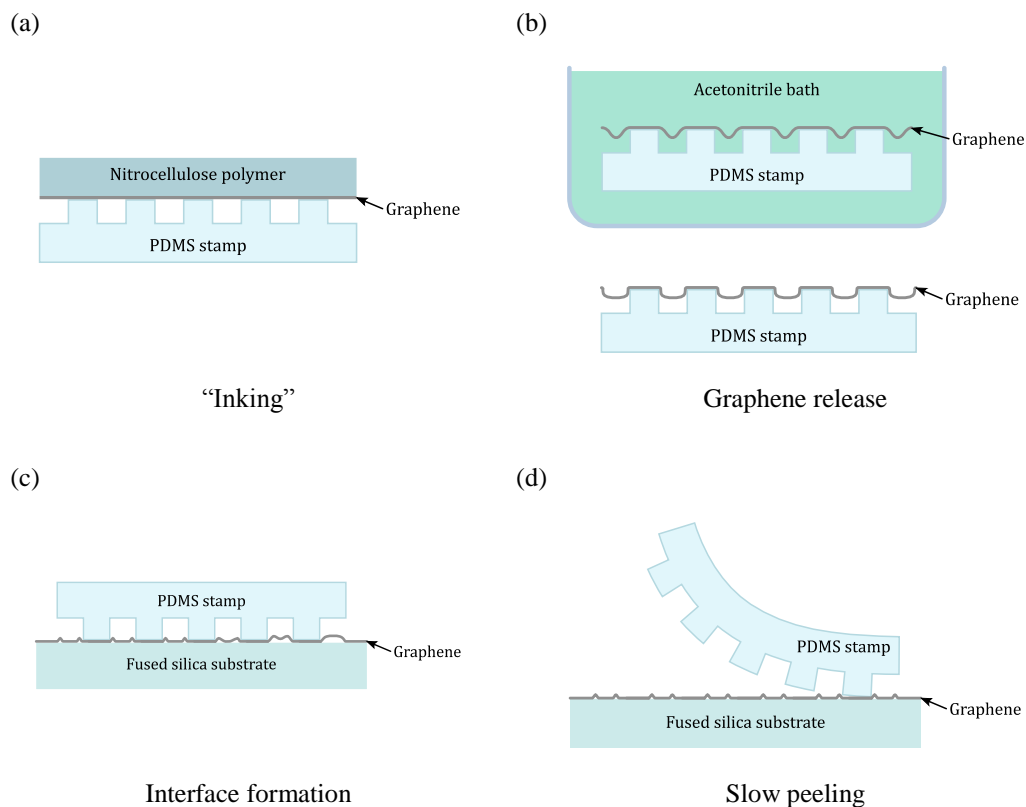


Figure 5.1: Schematic representation of the GraFold concept. (a) A polymer supported graphene film is draped across a relief patterned stamp. (b) The polymer layer is dissolved. (c) The stamp is placed onto the substrate, and PDMS is separated from graphene by slow peeling. (d) The collapse of graphene loops creates free-standing folds.

GraFold is a transfer/printing process where the excess of graphene film produces the folds. One achieves that by using polydimethylsiloxane (PDMS) stamp with a periodic pattern that modulates the graphene tension and adhesion throughout the stamp.

The CVD graphene, once it has formed on the surface of the copper plate (the standard choice for the chemical growth of graphene [112], [113]), could be transferred onto any target substrate using a layer of a polymer (for instance PMMA – polymethyl methacrylate). One performs this by spin-coating of the polymer layer on top of graphene and subsequently etching off the copper plate. At this stage, one covers the required substrate with this polymer-graphene bilayer and dissolves the polymer with an appropriate solvent thus leaving a graphene film on the substrate [114].

In GraFold approach, at first, the polymer-graphene bilayer is placed on the top of the PDMS stamp (Figure 5.1a). One calls this step the *inking* of the stamp. At this point, the polymer layer supports the graphene film in a rigid planar form. Once it is dissolved, the graphene can relax

into the grooves of the PDMS stamp and partially adhere to the sidewalls as it is schematically shown in (Figure 5.1b). The subsequent drying process enhances this adhesion process [105].

The *inked* (with graphene) stamp is then transferred onto the destination substrate Figure 5.1c, at this stage, conformal contact is achieved between the stamp, graphene, and the substrate. Following this, one slowly peels the stamp away thus leaving the graphene film with mechanically patterned folds (Figure 5.1d). One performs the peeling of the stamp in the direction parallel to the fold features to reduce the amount of tears (in Figure 5.1d it is shown otherwise for the sake of simplicity and clarity). For similar reasons, the peeling is performed at a rate of 2 – 5 $\mu\text{m/s}$ [105]. Defects presented in graphene, such as grain boundaries, lead to the tearing in graphene during the removal of the PDMS stamp.

The graphene films produced by the GraFold printing show a periodic line structure (Figure 5.2a). These lines persist over the whole surface of the film and replicate the patterned landscape of the stamp. One can observe the graphene and these features on 300 nm SiO_2 with a 100 \times confocal optical microscope since this is a high-contrast configuration for graphene observation. The folded graphene film deposited on a metal substrate is invisible due to the absence of the optical interference effect thus indicating its cleanliness [115]. The optical images also reveal the presence of some tearing in the graphene film. These tears are because of large forces on the graphene during solvent drying and subsequent transfer [116]. Extensive tearing is unavoidable during the printing of continuous films. To reduce this one introduces controlled boundaries into the graphene by etching of the graphene into squares before the *inking* stage.

Scanning electron microscopy (SEM) in Figure 5.2b shows the more detailed structure of the folds, revealing that they have some flaws in their structure. In addition, it shows some tearing of the graphene films similar to the optical microscopy image.

Atomic force microscopy (AFM) reveals (see Figure 5.2c) that the height of the folds is around 20 nm. It also shows that some bubbles are present in areas between the folds. This indicates that the graphene does not sit perfectly flat on the substrate, which is typically taking place in transferred CVD graphene [117].

The high angle annular dark field (HAADF) scanning transmission electron microscope (STEM) imaging [118], [119] has been employed to obtain the cross-sectional picture of the structure of folds (Figure 5.2d). It reveals the shape of printed folds, pointing out that a radius

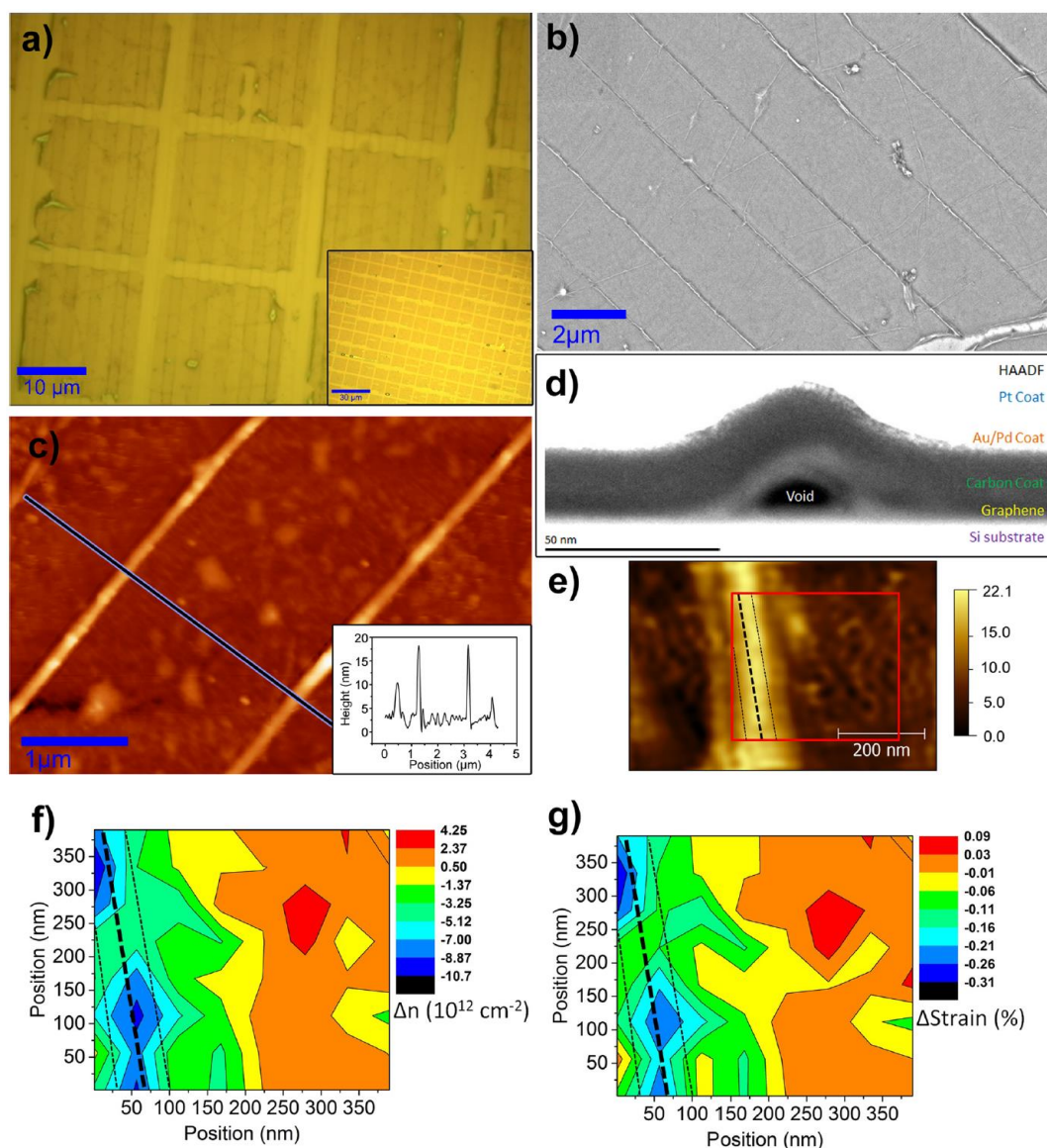


Figure 5.2: Microscopic characterization of the folded graphene film. (a) Optical micrograph of the folded graphene film. The inset shows a large-scale image of the film indicating the low level of tearing. (b) SEM of a folded graphene film. (c) AFM of a folded graphene film. The topography of the region under the blue line is shown in the inset. (d) The cross-sectional HAADF STEM of graphene fold. (e) AFM image of the single fold. The region studied with TERS is marked with the solid red line. (f) Contour map for graphene doping variation extracted from TERS data, assuming hole doping. (g) Contour map for graphene strain variation extracted from TERS data. The dashed black lines in e, f, and g indicate the region of the fold. Reprinted with permission from *Nano Lett.* 2015, 15, 857–863 [105]. Copyright (2015) American Chemical Society.

of curvature of the fold is approximately equal to its height, i.e., 20 nm. The radius of curvature is thus too big to induce a bandgap opening like it takes place in carbon nanotubes [29].

In addition to the structure, the information about strain and doping level has been obtained with near-field tip-enhanced Raman spectroscopy (TERS) [120]–[122]. This technique allows hyperspectral Raman imaging with a subwavelength resolution [123], [124]. The extracted images of local doping and strain variation are shown in Figure 5.2f and g, where the black dashed lines indicate the fold presented in Figure 5.2e. Figure 5.2f shows that the area of the fold has reduced doping density compared to the flat part near the fold. The difference between the doping density at the tip of the fold and that on SiO₂ amounts to 10^{13} cm^{-2} , which is consistent with the typical value of *p*-type doping of graphene transferred onto SiO₂ substrates [125]. One can explain the reduced doping in the fold by the fact the graphene in the fold is not in contact with the substrate [126]. This also confirms the STEM findings that are indicating the absence of intercalated material under the fold, which would otherwise dope graphene in the region of the fold (Figure 5.2d). From the low doping of the graphene in the fold, one thus can conclude that the GraFold printing provides an alternative approach of producing locally suspended graphene.

Figure 5.2g shows the extracted strain for the same region as in Figure 5.2e-f. The compressive strain variation in the fold region is up to +0.3%. A crude estimation of the total residual strain in the area surrounding the fold shows ca. 0.1% compressive strain. Even smaller strain values have been revealed over different flat regions of the same sample via confocal Raman spectroscopy measurements. This is in contrast with the reported compressive strain in transferred CVD graphene where the entire film is under strain [117], [127]. For printed graphene, the draping graphene on the flexible PDMS stamp before transferring to the substrate releases the intrinsic compressive strain.

5.2 Terahertz spectroscopy of GraFold samples

To study the influence of the GraFold printed folds on carrier transport in graphene, we first use THz-TDS. The measurement of the transmission through the GraFold sample of THz pulses linearly polarized parallel or perpendicular to the folds gives the estimation of the conductivity along these two orthogonal directions. The THz polarization is predetermined in the setup by the polarization of the generating laser pulse, and any change in this alignment usually causes a substantial change in the detected signals and thus alternate the experimental conditions. To make things simple and avoid this, we thus keep the polarization of the probing

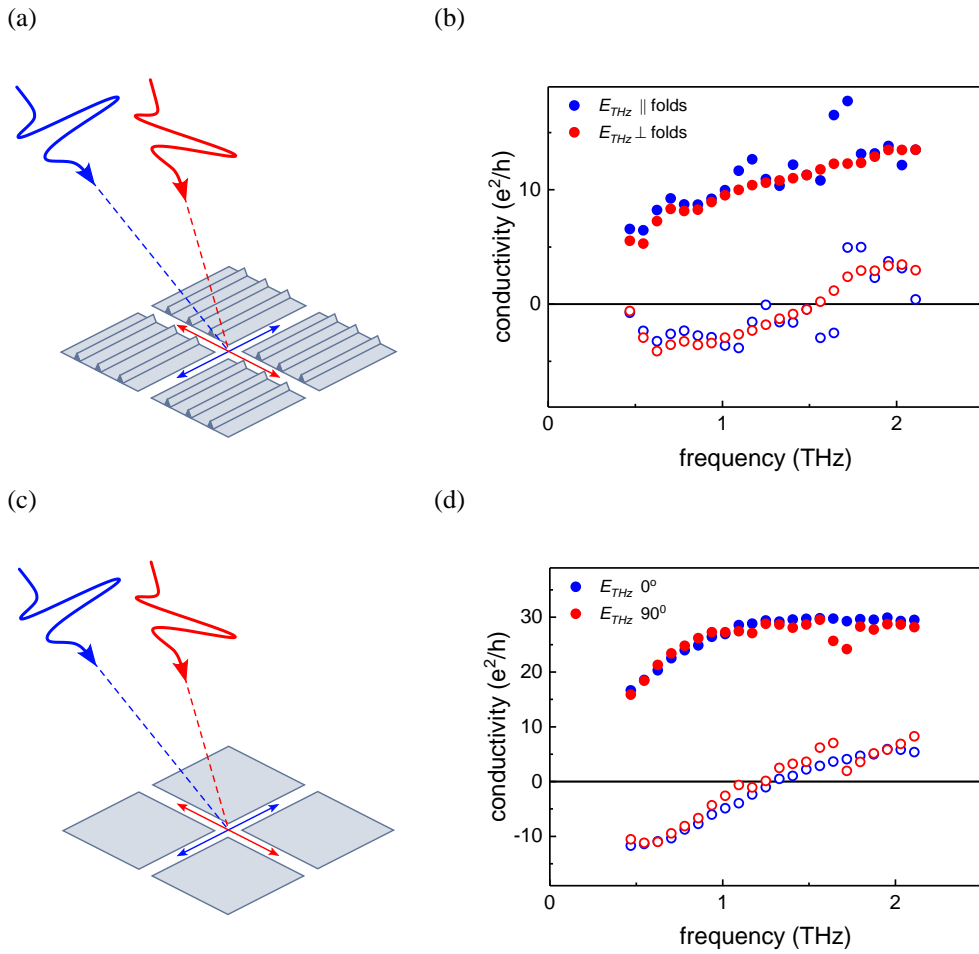


Figure 5.3. (a) The schematic layout of THz-TDS experiment on the GraFold sample (Figure 5.2a). Two probe polarization has been used, i.e., the blue one is along the folds' direction, and the red one is perpendicular to it. (b) The results of the experiments shown in a. (c) The schematic layout of THz-TDS experiment on the sample without folds (no GraFold printing) but with the similar etching, that graphene receives before GraFold printing. (d) The results of the experiments shown in c. The solid and hollow dots in b and d correspond to the real and the imaginary THz conductivities, respectively.

THz pulse untouched but instead rotate the sample relative to the direction of the probe pulse polarization. The illustration of these experiments is shown in Figure 5.3a (the pulses shown there are not to scale with the GraFold squares). In the experiment, we also use the wire grid THz polarizer to ensure the purity of the polarization of the probing THz pulse.

The resulting THz conductivities show similar behavior regardless of the probe polarization (Figure 5.3b). We also have performed similar experiments on the samples that are without GraFold printed folds as it is shown in Figure 5.3c, although this fold-free graphene has received a similar etching before the transfer onto the SiO_2 substrate. Thus, this control sample also consists of $20 \times 20 \mu\text{m}$ graphene square islands separated from each other by $2 \mu\text{m}$ gaps.

The resulting conductivities for the folds-free sample (Figure 5.3d) shows indistinguishable results for the two probe orientations and qualitatively similar to the results in GraFold. It is worth pointing out here, that due to a sub-mm wavelength nature of THz radiation, the focal point of the focused THz beam on the sample is thus on the order of 1 mm. This is much larger than any micro or sub-microscopic features of our GraFold sample (Figure 5.2a and b). Hence, in this experiment one measures the conductivity averaged over the $\sim 1\text{mm}^2$ area. The obtained conductivity spectra substantially differ from the Drude model. That importantly implies that the carriers in both samples experience substantial backscattering. Given the size of the squares being much larger than mean free path of the electrons, they unlikely affect the obtained carrier conductivity spectra. One can simply explain this on the example of ballistic transport. The average distance L that carrier could possibly cover in ideal graphene driven by the electromagnetic wave of 1 THz frequency is therefore equal to $v_F \cdot T/2$ (here T is the period of the wave, i.e., 1 ps), which evaluates to ~ 500 nm. Thus, we assume that the obtained spectral shape is due to the poorer quality of the CVD graphene used, where such a spectral shape implies the presence of the substantial amount of defects, i.e., crystal grain boundaries [81]. The overall reduction of the conductivity amplitude that amounts to ~ 10 units of e^2/h in GraFold sample comparing to the ~ 30 units of e^2/h in only etched graphene (Figure 5.3b, d) could be explained by the tearing during the GraFold process (Figure 5.2a). Despite the fact that the etching substantially reduces the tearing, the latter is not completely avoidable. Thereby the total amount of graphene in GraFold printed sample is less than in the etched fold-free sample, which leads to the observed reduction of the conductivity, since the probing pulse interacts with the lesser amount of the material. In total, we conclude that folds or GraFold printing process do not have a strong impact on the background THz conductivity.

To study the impact of folds further, we have performed OTP experiment. In this experiments, the sub-100 fs laser pulses (with a wavelength of 800 nm, which corresponds to 1.55 eV photon energy) excite the GraFold sample. Then we measure the time-dependent relative change of the peak field of the transmitted THz probe pulses at the peak of photoexcitation in two situations, as illustrated in Figure 5.4a.

The observed 1D dynamics (Figure 5.4b) follows the same evolution as that observed in the intact (without etching and folds) monolayer CVD graphene [128] as we have already shown in the previous chapter [67]. The rise dynamics correspond to the initial equilibration of the photogenerated carriers (that occurs on a timescale of photoexcitation, i.e., ~ 100 fs [100]).

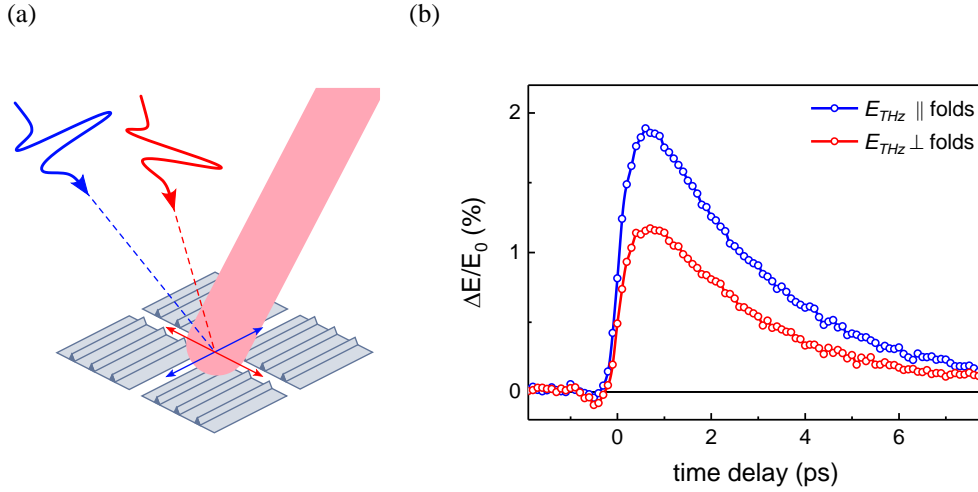


Figure 5.4. (a) The schematic layout of OPTP experiment on the GraFold sample (Figure 5.2a). Two probe polarizations have been used, i.e., the blue one is along the folds' direction, and the red one is perpendicular to it. The THz pulses probe the photoconductivity in the sample upon the excitation with an optical pulse (shown in purple). All sizes of the THz pulses and optical beam are not up to the scale of sample's features (b) The results of the experiments shown in a. The 1D dynamics shows the relative change of the peak THz amplitude as a function of pump-probe time delay.

At the peak of the dynamics, the carriers are in the heated up state, which results in the observed THz bleaching (Figure 5.4b). The latter corresponds to the reduced THz conductivity compared to the unexcited state ($-\Delta\sigma \propto \Delta E/E_0$). The relaxation of $-\Delta\sigma$ on the time scale of ca. 10 ps reflects the dynamics of electron gas cooling, which occurs via phonon emission [128]. As can be seen in Figure 5.4b, the THz bleaching measured parallel to the direction of fold exceeds the one measured perpendicular to it.

We have also measured the dependence of the peak photoconductivity as a function of optical pump fluence for both cases Figure 5.5a. Within the employed range of excitations, we observe equal dependence for both cases. The ratio of the peak photoconductivities (parallel to the perpendicular) has no dependence on the incident excitation density Figure 5.5b, and it is equal to ~ 1.55 . As no optical pump absorption anisotropy was found in our sample, which could lead to the asymmetry in the density of the photoexcited charges, the observed anisotropy of photoconductivity can only be related to the anisotropy of carrier mobility in the direction parallel and perpendicular to the folds, i.e., of $\mu_{\parallel}/\mu_{\perp} = 1.55$. TERS measurements (Figure 5.2f) reveal the difference in local doping densities on the order of 10^{13} cm^{-2} between the folds and surrounding areas, which must result in substantial local potential fluctuations in the direction perpendicular to the folds. Therefore, the most likely cause for the observed carrier

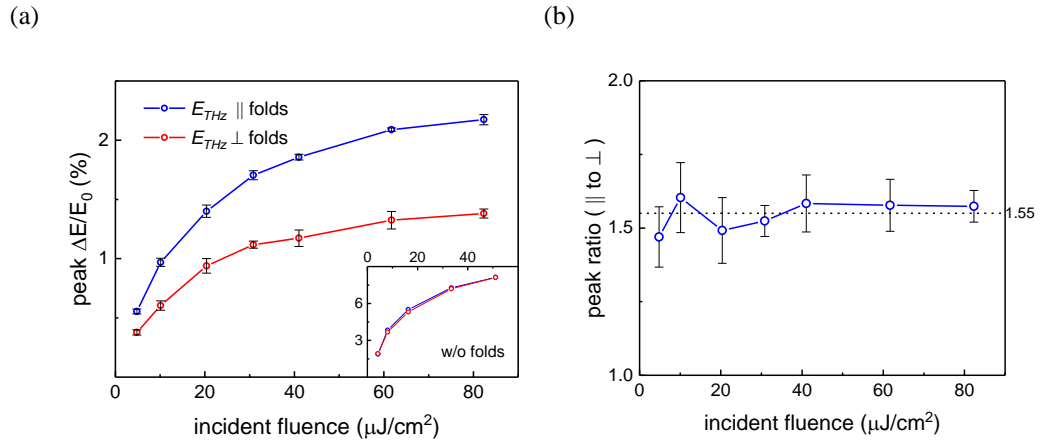


Figure 5.5. (a) The peak of 1D dynamics from Figure 5.4b as a function of incident excitation density. The inset shows the similar plot for the fold-free sample. Blue and red colors correspond to the two probe polarization directions, explained in the text and Figure 5.4a. (b) The ratio of the peak 1D dynamics parallel to fold to the one perpendicular to them as a function of the incident fluence. The dashed line shows the mean value of the peak ratio for all fluences.

mobility anisotropy is a highly anisotropic potential landscape for the carriers moving perpendicular and parallel to the folds. We note that in our samples the 100 nm folds of lightly doped graphene are separated by 2 μm stripes of highly doped one (Figure 5.2b,e), and hence the folds comprise only about 5% of the area of the THz-probed sample. In this respect, it is quite remarkable that such a low filling fraction of 1D folds (in a sense that their length infinitely larger than their width) results in a conductivity anisotropy as high as 1.55: 1, clearly indicating the potential of GraFold for optoelectronics applications where ultrafast directional charge transport may be required, such as in mechanically printed electronic circuits.

5.3 Conclusions

In this chapter, we have studied the periodically folded graphene using so-called GraFold printing method. The introduced folds have the semicircular form. Near folds, graphene shows reduced p -doping and a small amount of compressive strain. Using OPTP spectroscopy, we show that the periodic folding of graphene introduces significant charge transport anisotropy in the photo-excited state exhibiting ~ 1.55 times higher suppression of the background conductivity in the direction parallel to folds. Meanwhile, the folded graphene shows no explicit anisotropy in the background conductivity.

Chapter 6

Terahertz spectroscopy of graphene nanoribbons

The material presented in this chapter is a result of the combined work of the author with Yunbin Hu, Uliana Beser and Akimitsu Narita from the group of Klaus Müllen, who have kindly provided us with the GNR samples. Silvio Osella from the Centre of New Technologies, the University of Warsaw in Poland and David Beljonne from the Laboratory for Chemistry of Novel Materials, the University of Mons in Belgium have provided the Density functional theory (DFT) and Deformation potential (DP) calculations. The author has performed all THz measurements, as well as retrieved and analyzed THz conductivities. The results presented in this chapter have been the basis for the publication *J. Am. Chem. Soc.* 2017, 139, 7982–7988 [129]. The published data are presented here with permission from the American Chemical Society. Copyright (2017).

As it was mentioned previously in section 1.2, the chemical synthesis of GNRs by a bottom-up approach [12], [39], [40] provides the unique control over the variety of structural properties of the GNRs that is usually not possible by top-down methods such as lithography. The width and lattice orientation, in particular, could still be tuned in the top-down approaches since the former is defined by the technical limits of a particular method of fabrication and the latter by the lattice orientation of the initial graphene film [130]. Meanwhile, the physically smooth and clean edge structure is challenging to achieve by top-down methods. As we have already stated in section 1.2, the edge plays a crucial role in the electronic properties of GNR. Thereby in this sense, the bottom-up methods have the apparent advantage since the synthesized GNRs have well-defined edge structure [40]. The perspective of having such an ability to control the structure of the GNR brings the very relevant question of how exactly the structural properties of the GNRs influence their conductive properties.

The conductivity properties of the various GNRs have been the subject of intense study [66], [131]–[133]. The contact-based measurements in such nanosystems are naturally challenging [35], [134]–[137]. Thereby THz spectroscopy is a particularly attractive method of investigating the charge transport in GNRs [1] since it allows retrieving the conductivity of materials of interest without physical contacts. The recorded THz conductivity spectra and their interpretation provide access to fine details of carrier transport. Moreover, the conduction mechanism such as free versus bound charge, quasi-free charge localized on potential long-range corrugations and so forth [138] also could be determined.

In this chapter, we are investigating how the structure of GNRs and in particular their edge structure affects the carrier transport. To this end, we employ OPTP spectroscopy (section 2.2.2).

6.1 Graphene nanoribbons samples

The lattice structures of studied GNRs are shown in Figure 6.1. All these GNRs have been prepared by a solution-based bottom-up protocol that provides GNRs of hundreds of nanometers long [39], [40]. The nomenclature of structures is as follows. The letter C in the CGNR stands for cove – the peculiar part of the edge structure that is highlighted with red color in Figure 5.1a. The front number (e.g., 6CGNR) counts the amount of the whole zigzag chains aligned along the axis of the ribbon [139] (see Figure 6.1a). The *p*-AGNR is an armchair GNR where *p* stands for para – the name of the implemented connectivity of monomers (building blocks of the GNR) that are highlighted with bright red in Figure 6.1c. We note that 4CGNR shown in Figure 6.1d has not been studied in this work, although it has been studied and published previously in refs [66], [140]. These results have been considered here.

Further, one can notice dodecyl chains ($C_{12}H_{25}$, marked with R in Figure 6.1) attached to the periphery of GNRs. Their purpose is dictated by the synthesis method that in particular takes place in a liquid. In first and foremost one introduces them into a precursor of the GNR to sterically hinder [141] undesired conformations and thus secure the formation of strait GNRs [40]. Chains also enhance the dispersibility of the resulting GNRs [142] in a solvent. These polymeric chains could be attached to different sites of the precursor resulting in the formation of the similar structure of a backbone of the GNR, although with different locations of these chains at the periphery of the GNR. As one can see that in particular in Figure 6.1a and b,

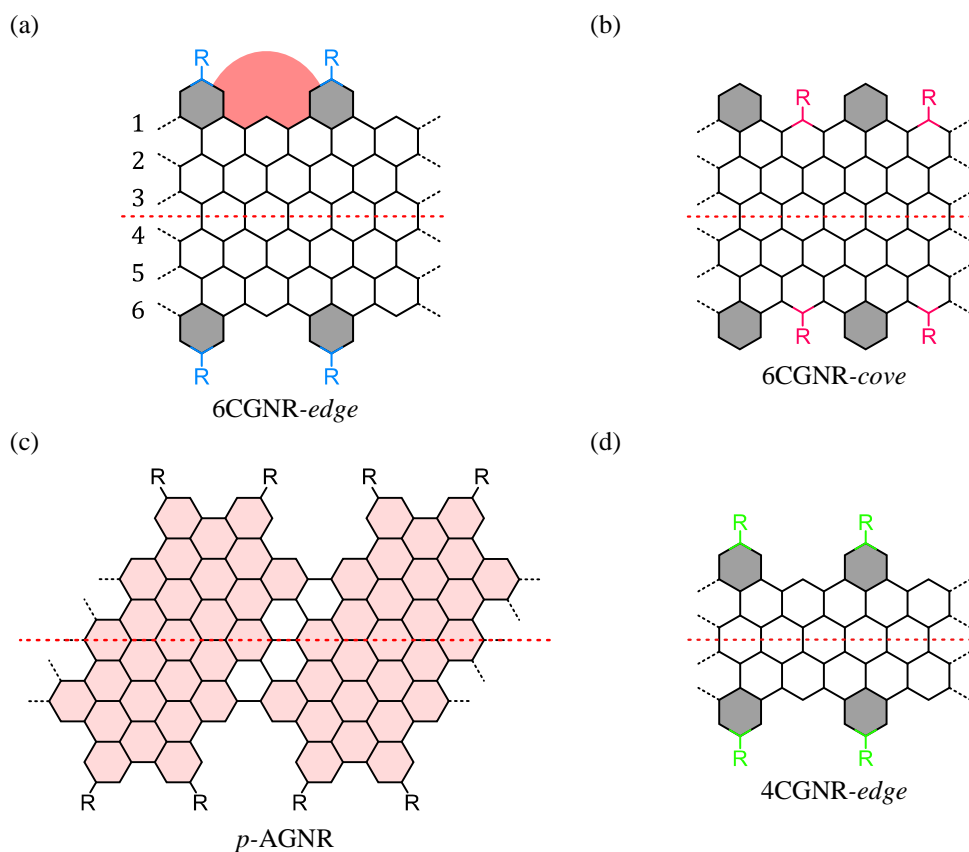


Figure 6.1: Chemical structure of the investigated GNRs (a-c), as well as the one, studied previously (d) [66]. (a) 6CGNR-edge, with dodecyl ($C_{12}H_{15}$) chains on the outer benzene rings (shaded with gray), blue color. (b) 6CGNR-cove with chains on the inner benzene rings, red color. (c) *p*-AGNR terminated by the same dodecyl chains. (d) 4CGNR-edge investigated in work [66] by Jensen et al. Dodecyl chains are marked with R. Adapted with permission from *J. Am. Chem. Soc.* 2017, 139, 7982–7988 [129]. Copyright (2017) American Chemical Society.

where the aforementioned dodecyl chains are bonded at the outermost or innermost sites of the 6CGNR structure. We thereby distinguish them as *edge* and *cove* sites, respectively. The precise position of the dodecyl chains, in Figure 6.1a and b, affects the structure of 6CGNR. In the case, when they sit in the cove sites (see Figure 6.1b, we call it 6CGNR-*cove*), they cause out-of-plane bending of neighboring protruding benzene rings (shaded with gray in Figure 6.1, the actual bending of the structure is not shown). In the opposite, when the chains are attached to the protruding rings (Figure 6.1a, we call it 6CGNR-*edge*) of the edge structure, the 6CGNRs retain their planar geometry. This structural distortion of the 6CGNR-*cove* causes the bandgap lowering in comparison to the 6CGNR-*edge*, the details of this are published in work by Hu et al. [143]. The impact of the precise location of the alkyl chains on the band

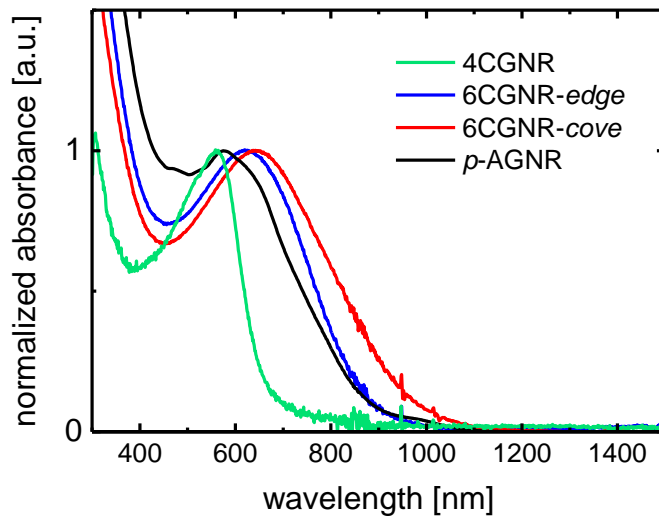


Figure 6.2: The absorbance of the investigated GNR samples dispersed in TCB solvent. The data have been normalized to the exciton resonance maxima of the GNRs. Adapted with permission from *J. Am. Chem. Soc.* 2017, 139, 7982–7988 [129]. Copyright (2017) American Chemical Society.

structure is also evident from the optical density measurements shown in Figure 6.2, where the absorption spectra of these two types of 6CGNRs structures (blue and red) are compared.

To perform optical and THz measurements, all GNRs have been dispersed in a solvent, which in this case is 1,2,3-trichlorobenzene (TCB). TCB is transparent at optical and the most important THz frequencies, thus making THz measurements possible. All dispersions have been sonicated for ~15 min., centrifuged and filtered to achieve the bundle free suspension of freely floating GNRs in the volume of the solvent. The resulting suspensions have been poured into the optical cuvettes. The optical cuvette consists of 1 mm thick quartz windows separated by a 1 mm thick gap that is filled with the suspension (see for example Figure 3.14).

The optical density spectra of the three suspensions of GNRs (6CGNR-*edge*, 6CGNR-*cove*, and *p*-AGNR, see Figure 6.2), reveal that the optical bandgaps of all samples are in the spectral range between 900 and 1000 nm (that corresponds to the photon energy range of 1.20-1.40 eV). An optical transition of excitonic origin dominates the optical spectra of all GNR samples.

6.2 Terahertz conductivity of graphene nanoribbons.

We assume that all presented GNRs are intrinsic semiconductors, i.e., there are no free charges in neither the conduction nor the valence band. The probability of the thermal electrons (holes)

to occupy the conduction (valence) band is also low given that bandgaps (~ 1 eV) are much bigger than the thermal energy (~ 0.03 eV). Thereby to study the conductivity we employ OPTP spectroscopy where one creates free carriers by optical excitation and probe their conductivity with a THz pulse.

To photoexcite GNR samples, we employ ultrashort (~ 40 fs) optical pulses with 3.1 eV photon energy (400 nm wavelength) that we obtain from the 1.55 eV laser pulses by doubling photon energy in a nonlinear crystal (BBO). The photon energy of the optical pump exceeds the bandgap of all presented GNRs (Figure 6.2). Therefore, the photoexcitation generates electrons and holes with energies above the conduction band minima and below the valence band maxima. The formation of excitons out of these ‘hot’ electron-hole pairs is also not excluded. Nevertheless, the recombination of ‘hot’ excitons can also lead to the free carrier formation at short delay times [144]. Of note, in these measurements, one cannot distinguish between the conductivity contributions from electrons and holes, so the sum of both contributions is measured at once [1]. In the OPTP experiments, we measure both 1D and 2D scans.

In 1D spectroscopy experiment, we record the time evolution of real and imaginary conductivity of samples that follow the photo-excitation. To this end, as it has been introduced in the section 2.2.2, one measures the relative change of the field amplitude at the peak [63] and the first zero crossing after the peak [64] of the probing THz pulse. The measured transient dynamics of real and imaginary photoconductivity in all three types of GNRs are shown in Figure 6.3 as a function of the time delay between optical excitation and probing THz pulse. After the initial ~ 0.5 ps long rise, the photoconductivity demonstrates fast, ~ 1 ps long decay followed by a slower one. At the latter stage, the imaginary part of the conductivity remains large relative to the real one in all GNR samples.

The negative imaginary conductivity together with the vanishingly small real one indicates that at later times upon the optical excitation the conductivity response is dominated by bound charges, such as excitons, rather than by free carriers [43]. One can expect the efficient exciton formation in these systems given the one-dimensional nature of GNRs and weak screening due to the low dielectric constant of the environment. Thereby, we conclude that in the first moments after optical excitation at the peak of 1D scans there are mostly mobile electrons and holes in the conduction and the valence band. The similar 1D dynamics have been reported in narrower [66] and broader [39] GNRs.

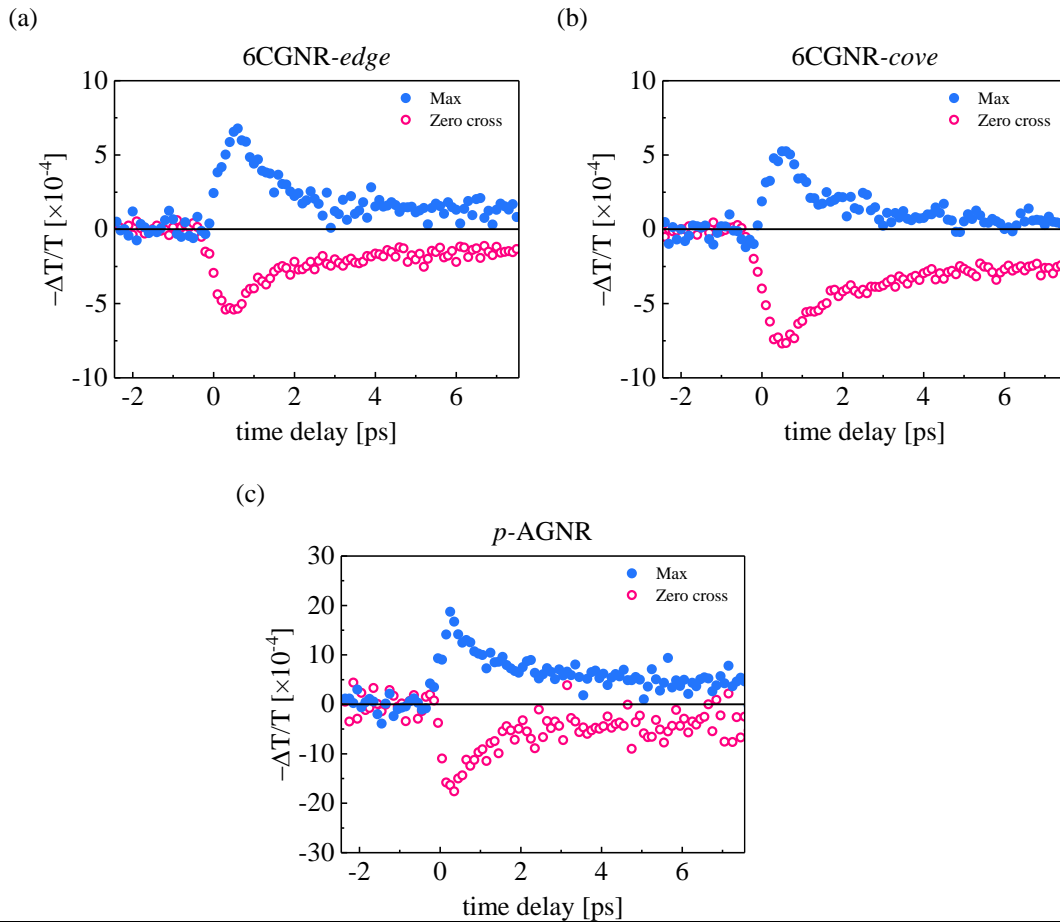


Figure 6.3: THz photoconductivity of GNRs dispersed in 1,2,4-trichlorobenzene, photoexcited by optical pulses (400 nm wavelength) with a sheet excitation density of $\sim 10^{19}$ photons/m² (c). Plots showing the dependence of the relative change in peak THz field transmitted through the sample on the pump–probe delay for 6CGNR-*edge*, -*cove*, and *p*-AGNR, respectively. The solid blue circles correspond to the change at the peak field of the THz pulse (representing the dynamics in real conductivity), and the red hollow circles show the change in the crossing point of the THz field (representing a change in the imaginary part of the conductivity). Adapted with permission from *J. Am. Chem. Soc.* 2017, 139, 7982–7988 [129]. Copyright (2017) American Chemical Society.

To study the impact of optical intensity on the conductivity dynamics in GNRs samples, they have been optically excited at photon densities ranging from 0.1×10^{19} photon/m² to 2.3×10^{19} photon/m². These are essentially the limiting values of optical intensity attainable in our setup (at 400 nm wavelength). Then the relative change at the peak of the THz pulse has been recorded at the pump-probe time delay corresponding to the maximum signal in the 1D scans (~ 0.5 ps, Figure 6.3). We have found that at high excitation densities ($> \sim 1.5 \times 10^{19}$ photon/m²) the magnitude of this relative change for all three samples deviates from the linear dependency observed at the lower fluences (see Figure 6.4).

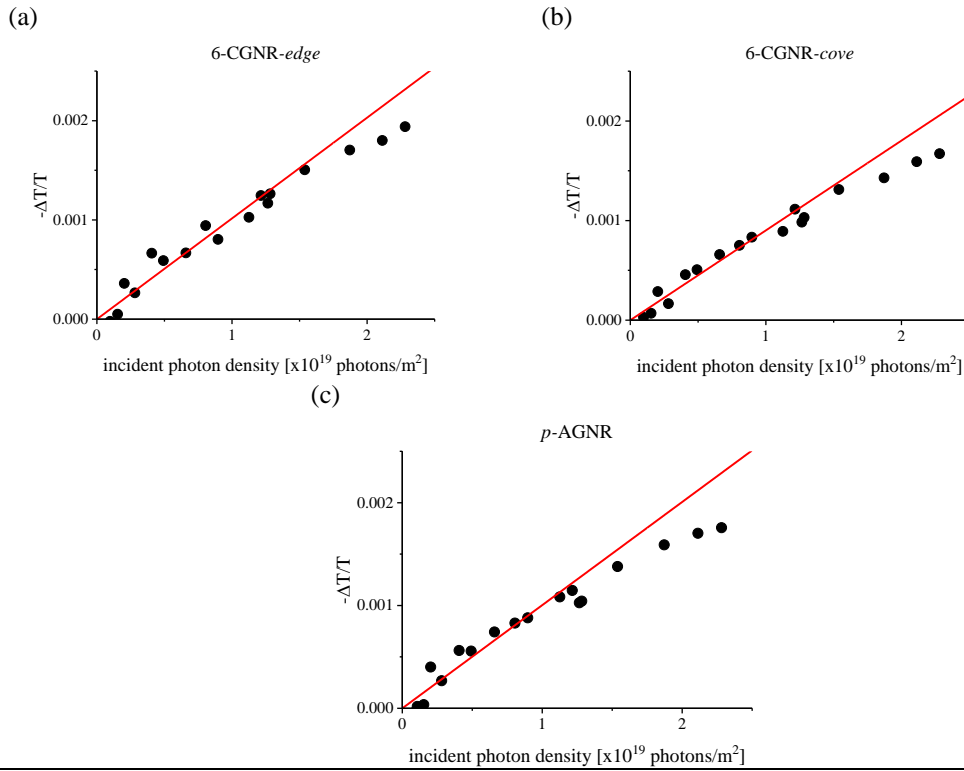


Figure 6.4: The maximum relative change of the THz transmission upon photo-excitation in three GNR samples as a function of the incident photon density. In all three samples, it deviates from the linear trend at higher pump intensities.

One can explain such behavior either by absorption saturation in the nanoribbons or by the increased carrier density at higher incident fluences facilitating more efficient binding of electrons and holes into excitons that do not contribute to the THz absorption [145]. In both scenarios, the per-photon efficiency of converting absorbed photons into mobile, free carriers is reduced at elevated excitation densities compared to lower excitation densities. In our experiments, we have therefore kept the pump intensities at values corresponding to the linear excitation regime.

To shed light on the nature of carrier transport in GNRs, we have measured the frequency-resolved complex-valued conductivity spectra (2D spectroscopy, see section 2.2.2), at the maxima of the 1D dynamics, i.e., approximately 0.5 ps after optical excitation. The AC photoconductivity $\Delta\sigma(\omega)$ that is obtained in this experiment is a characteristic measure of the transport properties of charges on the nanoscale. To illustrate this, let's consider a ballistic propagation of an electron at room temperature having the thermal velocity $\sim 10^5$ m/s, which

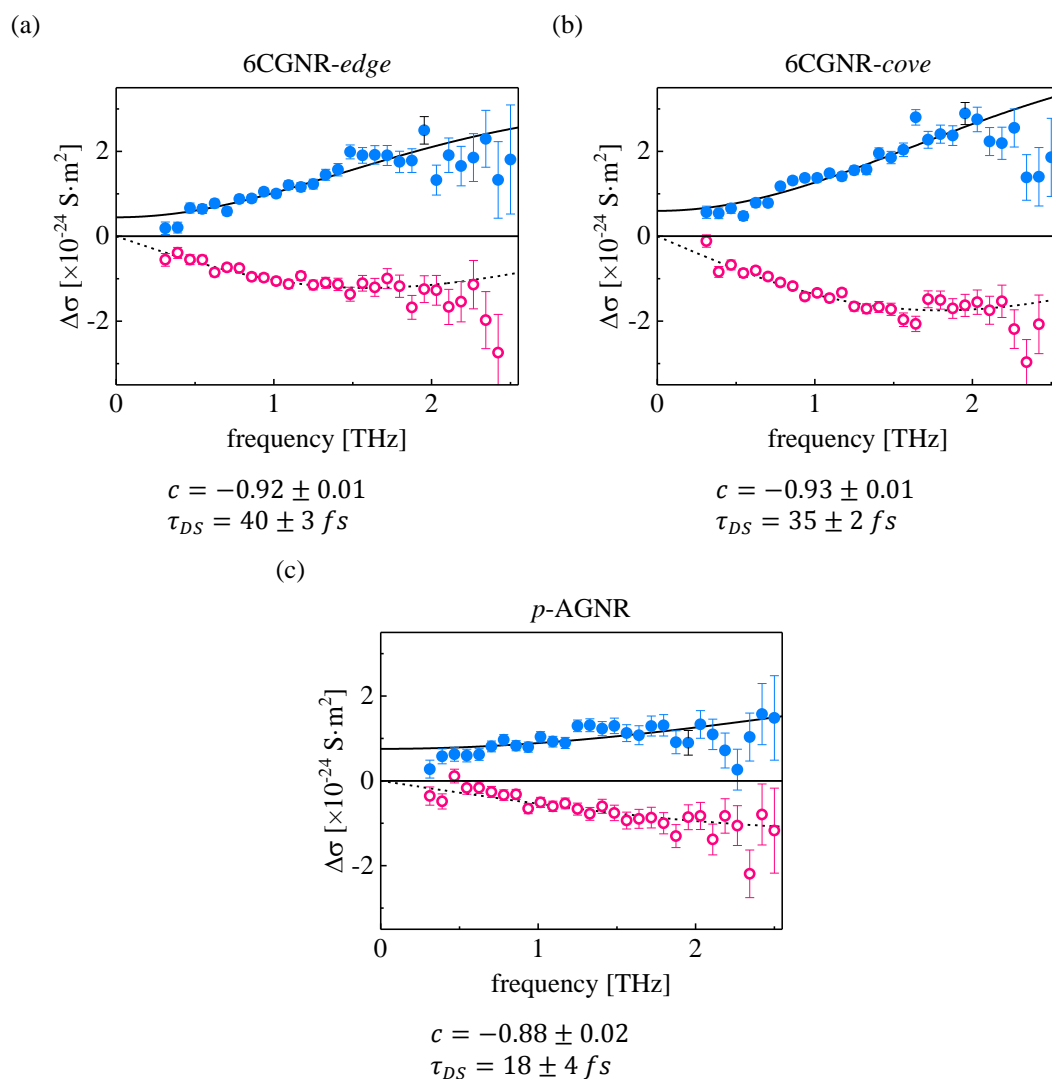


Figure 6.5: The complex frequency-resolved conductivity measured 0.5 ps after photoexcitation, i.e., at the peak of the photoconductivity (Figure 6.3). The conductivity is scaled to the density N of absorbed photons. The lines show the results of the Drude–Smith model, with parameters shown in the respective panels. Adapted with permission from *J. Am. Chem. Soc.* 2017, 139, 7982–7988 [129]. Copyright (2017) American Chemical Society.

is a fair assumption for these materials. The moving distance of such a charge propelled by the electric field cycle of ca. 1 ps duration (like in the probing THz pulse) amounts to a length of ~ 100 nm [1]. As such, the conductivity is probed on length scales shorter than the actual length of the nanoribbons studied here (100s of nm), so we can neglect the effects of the ends of the ribbons on the measured conductivity.

The retrieved conductivity spectra for all GNR types are characterized by positive real and negative imaginary parts, both increasing in absolute magnitude towards higher THz

frequencies, as one can see in Figure 6.5. This behavior qualitatively resembles the conductivity that is typical for many nanometer-sized semiconductors, including narrower GNRs, carbon nanotubes [66] and also semiconducting polymers [146].

These conductivity spectra can be well described by the Drude-Smith (DS) model [49] introduced in section 1.2. This conductivity model is a fair assumption in our case as other models, such as the Lorentz oscillator model [138], cannot reproduce such a large real conductivity amplitude as compared to the imaginary one. Further, the hopping model [138] seems also less applicable to GNRs, as their structure is uniform with minimum defects and given the fact that the sample represents a dispersion of freely floating GNRs with minimum interconnections. To fit the spectra we have used the expression for the DS conductivity in its reduced form where the only first term in the summation (see Eq. 2.35) is non-zero, that is:

$$\hat{\sigma}_{DS}(\omega) = \frac{\varepsilon_0 \omega_p^2 \tau_{DS}}{1 - i\omega \tau_{DS}} \left(1 + \frac{c}{1 - i\omega \tau_{DS}} \right) \quad (6.1)$$

here ε_0 is the vacuum permittivity, ω_p is the plasma frequency, the square of which is proportional to the carrier concentration, τ_{DS} is the average carrier momentum scattering time, and the parameter c describes the correlation between carrier momentum before and after a scattering event (section 1.2). Fitting frequency-resolved conductivity spectra of all GNRs samples to the DS model produces the localization parameter c of -0.92 ± 0.01 (-0.93 ± 0.01) for 6CGNRs-*edge* (-*cove*) and -0.88 ± 0.02 for *p*-AGNRs samples. A very similar c parameter value has been reported for narrower 4CGNRs [66].

Following ref. [66], the retrieved values of the localization parameter c are in reasonable agreement with the ones expected for a randomly oriented 1D conductors in a non-conducting solution. Indeed, the linearly polarized THz field accelerates charges in nanoribbons along its backbone axis. Thus when GNR is parallel to the THz field, the response would be characterized by the DS model where $c = 0$. In the opposite case, of perpendicular orientation, this value is -1 . Averaging on all possible orientations of the GNRs in the suspension one obtains the expected average value of parameter c that amounts to $-\pi/4 = -0.78$ [66].

The assumption of an infinite 1D conductor can be applied for the current samples as well, where the length of the GNRs (100s of nm) is much longer than the length scale of the average carrier propagation driven by the THz field. Given the length of the GNRs in the presented sample that are 100s of nm, the assumption of the randomly oriented 1D conductors can also be applied.

We note that the measured spectra demonstrate the conductivity of the sample as a ‘whole’, as an overall response of many GNRs floating in the body of solvent. Nevertheless, the fitting of the DS model to the conductivity spectra allows retrieving of the crucially important parameter characterizing the microscopic transport in the GNR, i.e., the carrier momentum scattering time τ_{DS} (see Eq. 6.1). This time constant is a measure of the intrinsic conductivity of the GNRs and related to the carrier mobility $\mu = e\tau_{DS}/m$. Applying the DS model to the data, we obtain the momentum scattering times τ_{DS} equal to 40 ± 3 fs and 35 ± 2 fs for the 6CGNR-*edge* and -*cove* samples, respectively, and 18 ± 4 fs for the *p*-AGNRs.

Within the experimental error, one can argue that both *c* parameters (~ -0.92) and the scattering times (~ 37 fs) are similar for the 6CGNRs-*edge* and -*cove*. This importantly implies that the conductivity in these two nanoribbons is largely unaffected by the location of the alkyl chains and the concomitant distortion of the peripheral benzene rings. For the narrower 4CGNR with the larger bandgap, a shorter scattering time of 30 fs has been previously reported [66]. However, for the *p*-AGNR ribbons, the scattering time is substantially reduced reaching only the half of that of the 6CGNRs. One thus can observe the following trend in the obtained scattering times: $\tau_{DS}^{6CGNR} > \tau_{DS}^{4CGNR} > \tau_{DS}^{pAGNR}$.

6.3 Electronic structure and transport calculations

To study the origin of the variation in the measured momentum scattering times in different GNR structures, electronic structure and transport calculations have been performed.

The electronic structure of GNRs, including 4CGNR, has been calculated at the Density Functional Theory (DFT) level using the screened exchange hybrid exchange-correlation functional HSE06 and the standard 6-31G* basis set [147]. It worth noting that in these calculations, the alkyl side chains have been substituted with hydrogen atoms. We assume that these chains do not contribute to the frontier crystal orbitals. Although, they have a minor impact on the electronic band structure in 6CGNR-*edge* and 6CGNR-*cove*, as one can see that in their optical density spectra (Figure 6.2) and ref. [143]. Thereby, the calculations do not distinguish these two particular GNRs structures. The experimental THz responses of those two GNRs, which, within error, are indistinguishable, justifies this approximation.

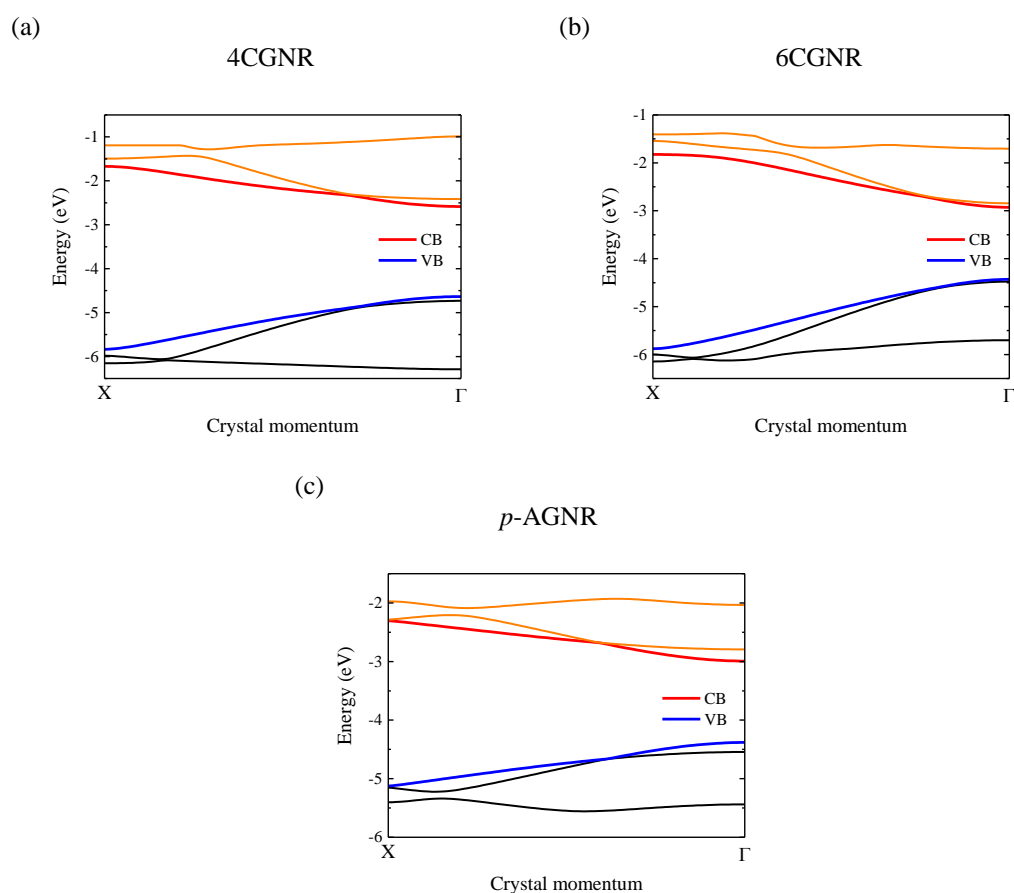


Figure 6.6: Electronic structure of the studied GNRs. Band structure showing the frontier crystal orbitals (red and blue lines). Adapted with permission from *J. Am. Chem. Soc.* 2017, 139, 7982–7988 [129]. Copyright (2017) American Chemical Society.

Calculations were performed for *p*-AGNR ribbons, the 6CGNRs, and its narrower analog 4CGNR.

The band structure diagram of the three ribbons is displayed in Figure 6.6. The corresponding wavefunctions of the band edge state at the Γ point which are equivalent to the frontier crystal orbitals are plotted in Figure 6.7. The frontier crystal orbital that is also referred to as the frontier molecular orbital corresponds to two states of the highest occupied molecular orbital (HOMO) for the hole and the lowest unoccupied molecular orbital (LUMO) for the electron. With regard to the band structure, these two states equivalent to the hole state at the valence band maximum (VBM) and the electron state at the conduction band minimum (CBM).

The most prominent result that one can conclude from Figure 6.6 is the close similarity between the electronic band structure of the 6CGNR and *p*-AGNR. These two systems possess a very similar band gap and the common squared dependence of energy versus momentum at

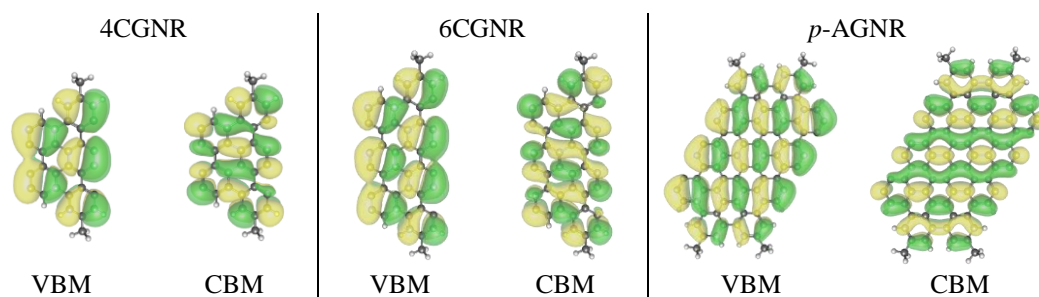


Figure 6.7: Plots of the wave functions at valence band maximum (VBM) and conduction band minimum (CBM), i.e., at the Γ point. Adapted with permission from *J. Am. Chem. Soc.* 2017, 139, 7982–7988 [129]. Copyright (2017) American Chemical Society.

the band edges. Despite that the CGNRs share the same crystal direction as pure ZGNRs, the former has the band structure contradicting to the one expected for the latter that displays flat, localized, edge states at the Fermi level [139] (see Figure 1.5 in section 1.2).

This distinct difference between zigzag and cove GNRs can be explained with regard to Clar's rule, a well-known approach in chemistry [148], [149]. In organic chemistry, one can define the so-called benzenoid aromatic ring as a resonance between two hexagonal rings with alternating single and double bonds (Figure 6.8a), which results from the delocalization of π electrons over the ring [150], [151]. For such a structure, known also as Clar's sextet, all the bonds sticking out of the hexagon are single bonds and, as a consequence, two benzenoid rings cannot be adjacent [152]. The Clar's rule states that for any given benzenoid structure, the representation with a maximum number of Clar sextets, called the Clar's formula, is the most representative and stable one [149], [153]. The electronic structure of such structure is then the result of a superposition of all possible Clar's formulas. Hence, the 6CGNRs have a single Clar's representation without any unpaired electron (see Figure 6.8b). In contrast, the corresponding representation of 6ZGNRs (6CGNR without protruding rings) involves unpaired electrons confined at the ribbon edges (see Figure 6.8c). Importantly, the number and relative position of the protruding benzo-rings in CGNRs has a profound impact on their electronic structure and may lead to the ZGNR-like one [154].

Following to earlier theoretical works on semiconducting CNTs [155], [156], the charge carrier mobility and scattering times in presented GNRs have been modeled using the deformation potential (DP) theory [157]. Where, it has been assumed that the scattering of charges is primarily due to acoustic phonons, similarly to CNTs [155]. The local deformations induced by these acoustic phonons are similar to the homogeneously deformed crystal [156],

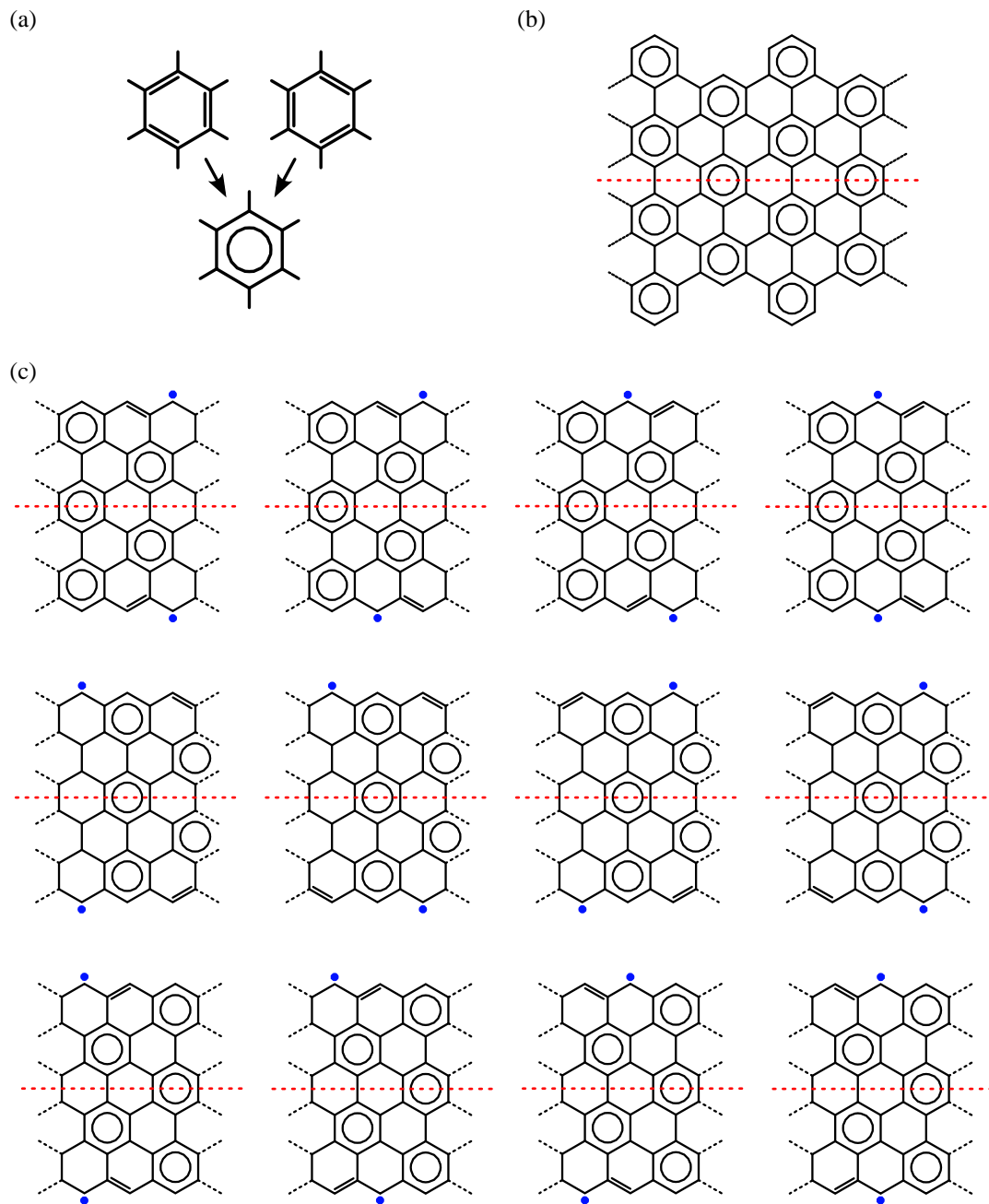


Figure 6.8: (a) The Clar's sextet represents the delocalization of six π electrons as a combination of two complementary hexagonal configurations featuring different single and double bonds. (b) Clar's formula of 6CGNR showing the configuration without any localized double bonds. (c) The possible Clar's formulas for 6ZGNR showing localized double bonds and unpaired electrons (blue dots) located at the edge of the ribbon.

[158]. In the effective mass approximation, the charge carrier mobility μ according to the DP theory thus reads as:

$$\mu = \frac{e\tau_{DP}}{m^*} = \frac{e\hbar^2 C}{\sqrt{2\pi k_B T} |m^*|^{3/2} E_1^2} \quad (6.2)$$

where e is the elementary charge, τ_{DP} the scattering time, m^* the effective mass, C the elastic constant, and E_1 the DP constant. To obtain C and E_1 , the lattice vector of the GNR is stretched or compressed along the longitudinal axis (see Figure 6.1). By fitting the total energy with respect to the lattice change, C can be derived from:

$$\frac{\Delta\mathcal{E}_{tot}}{a_0} = \frac{C}{2} \left(\frac{\Delta a}{a_0}\right)^2$$

Here, a_0 is the lattice constant at equilibrium, and Δa and $\Delta\mathcal{E}_{tot}$ are changes in the lattice constant and the total energy. The DP constant is defined as

$$E_1 = \Delta\mathcal{E}_{BE} \left(\frac{\Delta a}{a_0}\right)^{-1}$$

where $\Delta\mathcal{E}_{BE}$ is the energy change of the corresponding band extremum, i.e., at VBM for holes and CBM for electrons, due to Δa . The effective mass can be calculated from the second derivative around the VBM (CBM) for the hole (electron) as

$$\frac{1}{m^*} = \frac{1}{\hbar} \cdot \frac{\partial^2 \mathcal{E}(k)}{\partial k^2}$$

Here, $\mathcal{E}(k)$ is the energy dispersion of VB and CB. It is worth noting that the effective mass approximation is applied only for the cases of a parabola-like dispersion. In cases of very weak flat-band dispersion like in ZGNR (Figure 2.5b) or linear one similar to graphene (Figure 2.2), one has to appeal for Boltzmann transport equation coupled with the DP theory [154], [159], [160]. Nevertheless, in the case of parabolic bands, the DP theory using the effective mass approximation and the Boltzmann transport equation provide similar results [156].

Table 6.1 summarizes the relevant quantities obtained from the calculations, including the scattering times τ_{DP} . Irrespective of the charge carrier, we find lower τ_{DP} values for the p -AGNR, which can be associated with lower elastic constant, C , and larger electron-phonon coupling, E_1 , to longitudinal acoustic distortions. For all ribbons investigated, the electron scattering times are significantly larger than the corresponding hole values, which can be explained by the weaker coupling of the electrons to the phonons.

Table 6.1. Major results of DFT study and carrier transport calculations.

GNR	E_g eV	carriers	E_1 eV	C $\text{eV}\cdot\text{\AA}^{-1}$	m^* m_e	μ $\text{cm}^2\cdot\text{V}^{-1}\cdot\text{s}^{-1}$	scattering time τ_{BTE} fs
4CGNR	2.056	h	5.60	202.1	0.228	472	61
		e	0.84		0.246	18700	2615
6CGNR	1.508	h	6.28	299.6	0.154	994	87
		e	0.91		0.163	43800	4060
<i>p</i> -AGNR	1.388	h	8.80	65.14	0.0847	542	26
		e	1.40		0.0838	21800	1040

One could, in turn, understand this enhanced coupling of holes to the phonons in these structures by inspecting the electron and hole wave functions shown in Figure 5.6. At the VBM (the hole state) of all GNRs, the crystal orbitals have nodal planes running perpendicular to the ribbon axis, and thus it is vertically localized perpendicular to the stretching direction. In contrast, the CBMs (the electron state) of the ribbons show a bonding pattern delocalized along the stretching axis. It is argued that the band-edge shift due to ribbon stretching comes from the site energy instead of the hopping integral [156]. It is thus expected that the localized hole state is scattered more strongly by the acoustic phonon than the electron state as a result of the larger shift in the VBM (and hence higher E_1) than in CBM.

These theoretical calculations reveal several interesting aspects of charge carrier transport in presented GNRs. Firstly, derived from the DP theory scattering times for holes reproduce the experimentally observed trend: $\tau_{DS}^{6CGNR} > \tau_{DS}^{4CGNR} > \tau_{DS}^{pAGNR}$. Further, results reaffirm the absence of the direct correlation between bandgap and mobility. Even though, one can expect that the mobility should monotonously increase towards that of graphene for progressively smaller bandgaps. This is not the case for the presented GNRs. Particularly, in the case of *p*-AGNR, which have the smaller band gap than one in 4CGNR, the effective masses of electrons and holes are almost one order smaller than in the rest of structures, indeed approaching the zero mass of graphene. However, the resulting mobility is more than compensated by a reduction of the scattering times, due to stronger coupling to the acoustic phonons. Thus, the overall mobility is even smaller than in 4CGNR with the bigger bandgap.

In addition, the scattering times calculated with the DP theory are substantially larger than those retrieved from the THz experiments. One can explain this with the fact that calculations only account the effects of acoustic phonons on the motion of charges. This difference between

the modeled and measured scattering times has to be because of extra factors affecting charge transport that have not been accounted for in theory. That could be, for instance, alkyl side chains and (or) mechanical distortions of floating GNRs in the suspension, such as kinks.

The scattering time (τ_{DS}) inferred from the experimentally measured conductivities utilizing the Drude–Smith model is generally defined by the relation between the typical sizes of confining boundaries and the mean free propagation length of the carriers [161]. In GNRs, such boundaries could be manifested as potential barriers that occur as the result of extensive bending and buckling of the lattice, for instance, at the kinks of the backbone [162]. In the ideal Drude model ($c = 0$), the boundaries are absent, and charge carriers undergo momentum-randomizing scattering events due to collisions with the lattice. Therefore, in this case, the scattering time τ_{DS} coincides with the average momentum scattering time of the carriers in the bulk material [161]. One can expect such Drude-like conductivity behavior to occur in GNRs, in the case of carriers that are moving along the axis of an infinite, straight and structurally perfect nanoribbon in a vacuum. In this respect, the scattering time is expected to equal the one obtained with the DP theory (τ_{DP}). In our experiments, the GNRs are finite, flexible polymer chains floating in a dipolar molecular liquid thus they inevitably tend to bend, twist and entangle/aggregate with each other. Thereby, the carrier motion will be affected by the presence of these complex mechanical deformations in GNRs. The localization parameter c in DS model in our THz experiments largely reflects the random orientation of the ribbons. Although, the retrieved from the fitting c parameters for all structures are smaller than the value of -0.78 [66] expected from the randomized orientation of GNRs only. This discrepancy could be explained by the presence of extra factors leading to the stronger localization of carriers. That could be the potential corrugation induced by the aforementioned mechanical distortions.

To estimate the distance between these potential corrugations, we adopt a simple model that relates the measured DS scattering time to the one calculated with the DP theory. Here we assume the charge carrier that, after traveling over the distance l along the ribbon, scatters on a potential barrier (for instance, induced by a kink in the ribbon). The mean scattering time for such a charge is equal to:

$$\langle t \rangle = \frac{\int_0^{l/v_{therm}} t \cdot p(t) \cdot dt}{\int_0^{l/v_{therm}} p(t) \cdot dt} = \tau_{DP} \left(1 - \frac{l}{l_{free}} \cdot \frac{1}{\exp\left(\frac{l}{l_{free}}\right) - 1} \right)$$

Table 6.2. DP and DS carrier scattering times and the estimated distance between corrugations.

GNR structure	carriers	τ_{DP} fs	τ_{DS} fs	a nm
4CGNR	h	61	30	15
	e	2615		12
6CGNR	h	87	35-40	22
	e	4060		18
<i>p</i> -AGNR	h	26	18	17
	e	1040		12

where $p(t) = \exp(-t/\tau_{DP})$ is proportional to the probability density that the carrier scatters at time t . Here $v_{therm} = \sqrt{2k_B T/m^*}$ is the thermal velocity of the carriers with the effective mass m^* – taken from DFT calculations, and $l_{free} = v_{therm} \cdot \tau_{DP}$ is carrier mean free path. By assuming that this average time $\langle t \rangle$ equal to τ_{DS} we thus can estimate the mean value of the distance $\langle l \rangle$ between consecutive scattering potentials on a GNR by solving the following equation:

$$\tau_{DP} \left(1 - \frac{\langle l \rangle}{l_{free}} \cdot \frac{1}{\exp\left(\frac{\langle l \rangle}{l_{free}}\right) - 1} \right) = \tau_{DS} \quad (6.3)$$

The results are shown in Table 6.2 and reveal that $\langle l \rangle$ lies between 10 and 20 nm for all GNR structures. Comparing the 4CGNR to the 6CGNR, it seems that increasing the width of the nanoribbons leads to the increase of $\langle l \rangle$. This indicates that bends and buckles in the nanoribbon, which are expected to be reduced for the wider 6CGNRs, play a substantial role in the electronic motion in the GNRs.

6.3 Conclusions

The THz photoconductive properties of GNRs with different edge structures and position of alkyl chains appear to be qualitatively similar and can be well reproduced within the Drude-Smith conductivity model of quasi-free carriers with preferential backscattering. The carrier scattering times derived from this model imply that the alkyl functionalization of the edges has little impact on the transport properties of GNRs, while the effect of varying the edge structure of GNR is substantial.

Based on the studies presented in this chapter and the one published previously (4CGNR) [66], we have pointed out a clear trend: $\tau_{DS}^{6CGNR} > \tau_{DS}^{4CGNR} > \tau_{DS}^{pAGNR}$. Theoretical DFT calculations of the band structures together with transport calculation using the DP method show the same trend, yet with substantially increased values for carrier scattering time.

A simple model has been used to account for GNRs' corrugation as a possible origin of reduced scattering time as measured in the experiments. This model produces an effective mean free path of carriers in dispersed GNRs on the order of tens of nanometers that corresponds to the average distance between corrugations.

The results presented here show that the simple alkyl chains at the edge of GNRs have a minimal impact on the transport properties of the ribbons. However, the possible substantial change in the carrier transport is not excluded in the structures with complex functional groups [163] such as with a significant dipole moment or in the structures without the functionalization whatsoever. In particular, the comparison with the latter one is hindered due to the difficulty of preparation of a dispersed solution of such bare GNRs. Moreover, the synthesis of such GNRs is performed on the surface [164] and sometimes produces the network of interconnected GNRs.

Chapter 7

Summary and outlook

In this thesis, we have investigated charge carriers dynamics in three graphene-based systems. THz spectroscopy has been a primary tool to study these phenomena as it provides means for probing transport in broad frequency range without contacts. We investigated the following systems.

In a large-area monolayer of CVD graphene, we have shown that one can describe the ultrafast electron transport using a simple picture of a time-dependent thermodynamic balance maintained within the electronic population. Given the extremely efficient electron-electron interaction in graphene, the energy of a THz pulse or an optical signal is efficiently and instantaneously (on a sub-ps timescale) transferred into the internal energy of the carrier population. The condition of the energy and particle number conservation thus leads to the decrease of the chemical potential of graphene thereby reducing its intra-band conductivity. We have also shown that the efficiency of this process is strongly correlated with the carrier concentration and the excitation intensity.

In graphene with mechanically induced periodic folds (using the GraFold technique), we have shown that the folds have minimal impact on the background THz conductivity. At the same time, we have observed a significant charge transport anisotropy in the hot transport (optically excited state). That exhibits 1.55 times stronger suppression of the hot transport in the direction parallel to the folds. We nevertheless have not provided a profound understanding of the mechanism behind this first experiment on folded graphene. An initial explanation is that in photo-excited state this sample exhibit the anisotropic potential landscape that leads to the observed anisotropy of the photoconductivity. In the future, one can shed more light on this unique material by performing further experiments on the samples with an increased fold density, with different fold sizes and the larger graphene films.

In graphene nanoribbons, we have observed that carrier transport well described by the Drude-Smith model of the carriers with preferential backscattering. We have demonstrated that derived from this model scattering times of the carriers have a non-trivial correlation with the edge structure of the GNR. The DFT and DP transport calculation corroborated the experimental result although they provide larger values of the scattering times. We have accounted for this discrepancy by the presence of mechanical distortions in GNRs species that are freely floating in the liquid. Using a simple scattering model, we could evaluate the average distance between two neighboring kinks. We have also found a negligible influence of the simple alkyl chains on the carrier transport. As a future perspective, one can develop a deeper understanding of the ultrafast THz transport of GNRs by performing experiments on a broader variety of GNR structures. One of the possible directions could also be the developing of the samples with a more organized structure. As an example of it, one could imagine a network of perfectly aligned GNRs. Thereby in such configuration, the THz spectroscopy could provide a better evaluation of the conductivity in the experiment where the probing field polarization is aligned along the ribbons. Thus, one could avoid unwanted corrugations and the use of phenomenological models. One practically could achieve that in CVD grown ribbons on the surface.

Bibliography

- [1] R. Ulbricht, E. Hendry, J. Shan, T. F. Heinz, and M. Bonn, "Carrier dynamics in semiconductors studied with time-resolved terahertz spectroscopy," *Rev. Mod. Phys.*, vol. 83, no. 2, pp. 543–586, Jun. 2011.
- [2] K. S. Novoselov *et al.*, "Electric field effect in atomically thin carbon films," *Science*, vol. 306, no. 5696, pp. 666–9, Oct. 2004.
- [3] K. S. Novoselov *et al.*, "Two-dimensional atomic crystals," *Proc. Natl. Acad. Sci.*, vol. 102, no. 30, pp. 10451–10453, Jul. 2005.
- [4] A. K. Geim and K. S. Novoselov, "The rise of graphene," *Nat. Mater.*, vol. 6, no. 3, pp. 183–91, Mar. 2007.
- [5] A. H. C. Neto and K. Novoselov, "New directions in science and technology: two-dimensional crystals," *Reports on Progress in Physics*, vol. 74, no. 8, p. 082501, 01-Aug-2011.
- [6] R. R. Nair *et al.*, "Fine structure constant defines visual transparency of graphene.," *Science*, vol. 320, no. 5881, p. 1308, Jun. 2008.
- [7] K. S. Novoselov *et al.*, "Two-dimensional gas of massless Dirac fermions in graphene.," *Nature*, vol. 438, no. 7065, pp. 197–200, Nov. 2005.
- [8] G. Fiori *et al.*, "Electronics based on two-dimensional materials," *Nat. Nanotechnol.*, vol. 9, no. 10, pp. 768–779, Oct. 2014.
- [9] F. Bonaccorso, Z. Sun, T. Hasan, and A. C. Ferrari, "Graphene photonics and optoelectronics," *Nat. Photonics*, vol. 4, no. 9, pp. 611–622, Aug. 2010.
- [10] S. A. Mikhailov and K. Ziegler, "Nonlinear electromagnetic response of graphene: frequency multiplication and the self-consistent-field effects," *J. Phys. Condens. Matter*, vol. 20, no. 38, p. 384204, Sep. 2008.
- [11] S. A. Mikhailov, "Non-linear graphene optics for terahertz applications," *Microelectronics J.*, vol. 40, no. 4–5, pp. 712–715, Apr. 2009.

- [12] A. Narita, X.-Y. Wang, X. Feng, and K. Müllen, “New advances in nanographene chemistry,” *Chem. Soc. Rev.*, vol. 44, no. 18, pp. 6616–6643, 2015.
- [13] F. D’Angelo, Z. Mics, M. Bonn, and D. Turchinovich, “Ultra-broadband THz time-domain spectroscopy of common polymers using THz air photonics,” *Opt. Express*, vol. 22, no. 10, p. 12475, May 2014.
- [14] A. H. Castro Neto, N. M. R. Peres, K. S. Novoselov, and A. K. Geim, “The electronic properties of graphene,” *Rev. Mod. Phys.*, vol. 81, no. 1, pp. 109–162, Jan. 2009.
- [15] N. M. R. Peres, “Colloquium : The transport properties of graphene: An introduction,” *Rev. Mod. Phys.*, vol. 82, no. 3, pp. 2673–2700, Sep. 2010.
- [16] S. Das Sarma, S. Adam, E. H. Hwang, and E. Rossi, “Electronic transport in two-dimensional graphene,” *Rev. Mod. Phys.*, vol. 83, no. 2, pp. 407–470, May 2011.
- [17] M. I. Katsnelson, *Graphene*. Cambridge: Cambridge University Press, 2012.
- [18] P. R. Wallace, “The Band Theory of Graphite,” *Phys. Rev.*, vol. 71, no. 9, pp. 622–634, May 1947.
- [19] N. W. Ashcroft and N. D. Mermin, *Solid state physics*. Cengage Learning, 1976.
- [20] L. D. Landau and E. M. Lifshitz, *Quantum Mechanics*, 3rd ed. Butterworth-Heinemann, 1981.
- [21] L. D. Landau and E. M. Lifshitz, *The Classical Theory of Fields*, 4th ed. Butterworth-Heinemann, 1987.
- [22] A. C. Ferrari *et al.*, “Science and technology roadmap for graphene, related two-dimensional crystals, and hybrid systems,” *Nanoscale*, vol. 7, no. 11, pp. 4598–4810, 2015.
- [23] L. Banszerus *et al.*, “Ultrahigh-mobility graphene devices from chemical vapor deposition on reusable copper,” *Sci. Adv.*, vol. 1, no. 6, pp. e1500222–e1500222, Jul. 2015.
- [24] K. F. Mak, M. Y. Sfeir, Y. Wu, C. H. Lui, J. A. Misewich, and T. F. Heinz, “Measurement of the optical conductivity of graphene,” *Phys. Rev. Lett.*, vol. 101, no. 19, p. 196405, Nov. 2008.

-
- [25] K. F. Mak, J. Shan, and T. F. Heinz, "Seeing Many-Body Effects in Single- and Few-Layer Graphene: Observation of Two-Dimensional Saddle-Point Excitons," *Phys. Rev. Lett.*, vol. 106, no. 4, p. 046401, Jan. 2011.
- [26] P. Avouris, Z. Chen, and V. Perebeinos, "Carbon-based electronics," *Nat. Nanotechnol.*, vol. 2, no. 10, pp. 605–615, Oct. 2007.
- [27] F. Schwierz, "Graphene transistors," *Nat. Nanotechnol.*, vol. 5, no. 7, pp. 487–496, Jul. 2010.
- [28] F. Schwierz, "Graphene transistors: Status, prospects, and problems," *Proc. IEEE*, vol. 101, no. 7, pp. 1567–1584, Jul. 2013.
- [29] S. Reich, C. Thomsen, and J. Maultzsch, *Carbon Nanotubes*. John Wiley & Sons, 2004.
- [30] M. Terrones *et al.*, "Graphene and graphite nanoribbons: Morphology, properties, synthesis, defects and applications," *Nano Today*, vol. 5, no. 4, pp. 351–372, Aug. 2010.
- [31] S. Iijima, "Helical microtubules of graphitic carbon," *Nature*, vol. 354, no. 6348, pp. 56–58, Nov. 1991.
- [32] L. V. Radushkevich and V. M. Lukyanovich, "The structure of carbon forming in thermal decomposition of carbon monoxide on an iron catalyst," *J. Phys. Chem. Russ.*, vol. 26, no. 1, pp. 88–95, 1952.
- [33] K. Nakada, M. Fujita, G. Dresselhaus, and M. S. Dresselhaus, "Edge state in graphene ribbons: Nanometer size effect and edge shape dependence," *Phys. Rev. B*, vol. 54, no. 24, pp. 17954–17961, Dec. 1996.
- [34] B. Bartolo, Ed., *Collective Excitations in Solids*. Boston, MA: Springer US, 1983.
- [35] M. Y. Han, B. Özyilmaz, Y. Zhang, and P. Kim, "Energy Band-Gap Engineering of Graphene Nanoribbons," *Phys. Rev. Lett.*, vol. 98, no. 20, p. 206805, May 2007.
- [36] A. N. Abbas *et al.*, "Patterning, Characterization, and Chemical Sensing Applications of Graphene Nanoribbon Arrays Down to 5 nm Using Helium Ion Beam Lithography," *ACS Nano*, vol. 8, no. 2, pp. 1538–1546, Feb. 2014.
- [37] L. Jiao, L. Zhang, X. Wang, G. Diankov, and H. Dai, "Narrow graphene nanoribbons

- from carbon nanotubes,” *Nature*, vol. 458, no. 7240, pp. 877–880, Apr. 2009.
- [38] D. V. Kosynkin *et al.*, “Longitudinal unzipping of carbon nanotubes to form graphene nanoribbons,” *Nature*, vol. 458, no. 7240, pp. 872–876, Apr. 2009.
- [39] A. Narita *et al.*, “Bottom-Up Synthesis of Liquid-Phase-Processable Graphene Nanoribbons with Near-Infrared Absorption,” *ACS Nano*, vol. 8, no. 11, pp. 11622–11630, Nov. 2014.
- [40] A. Narita *et al.*, “Synthesis of structurally well-defined and liquid-phase-processable graphene nanoribbons,” *Nat. Chem.*, vol. 6, no. 2, pp. 126–132, Dec. 2014.
- [41] P. Drude, “Zur Elektronentheorie der Metalle,” *Ann. Phys.*, vol. 306, no. 3, pp. 566–613, 1900.
- [42] P. Drude, “Zur Elektronentheorie der Metalle; II. Teil. Galvanomagnetische und thermomagnetische Effecte,” *Ann. Phys.*, vol. 308, no. 11, pp. 369–402, 1900.
- [43] M. Dressel and G. Grüner, *Electrodynamics of Solids: Optical Properties of Electrons in Matter*. Cambridge University Press, 2002.
- [44] J. Sólyom, Ed., *Fundamentals of the Physics of Solids*. Berlin, Heidelberg: Springer Berlin Heidelberg, 2009.
- [45] A. Sommerfeld, “Zur Elektronentheorie der Metalle auf Grund der Fermischen Statistik,” *Zeitschrift für Phys.*, vol. 47, no. 1–2, pp. 1–32, Jan. 1928.
- [46] J. Horng *et al.*, “Drude conductivity of Dirac fermions in graphene,” *Phys. Rev. B*, vol. 83, no. 16, p. 165113, Apr. 2011.
- [47] A. J. Frenzel, C. H. Lui, Y. C. Shin, J. Kong, and N. Gedik, “Semiconducting-to-metallic photoconductivity crossover and temperature-dependent drude weight in graphene,” *Phys. Rev. Lett.*, vol. 113, no. 5, p. 056602, Jul. 2014.
- [48] M. Wagner *et al.*, “Ultrafast and nanoscale plasmonic phenomena in exfoliated graphene revealed by infrared pump-probe nanoscopy,” *Nano Lett.*, vol. 14, no. 2, pp. 894–900, Feb. 2014.
- [49] N. Smith, “Classical generalization of the Drude formula for the optical conductivity,” *Phys. Rev. B*, vol. 64, no. 15, p. 155106, Sep. 2001.

-
- [50] M. Tonouchi, "Cutting-edge terahertz technology," *Nat. Photonics*, vol. 1, no. 2, pp. 97–105, 2007.
- [51] T. Seifert *et al.*, "Efficient metallic spintronic emitters of ultrabroadband terahertz radiation," *Nat. Photonics*, vol. 10, no. 7, pp. 483–488, Jul. 2016.
- [52] R. W. Boyd, *Nonlinear optics*, 3rd ed. Academic Press, 2008.
- [53] Y.-S. Lee, *Principles of Terahertz Science and Technology*. Springer, 2009.
- [54] D. T. F. Marple, "Refractive Index of ZnSe, ZnTe, and CdTe," *J. Appl. Phys.*, vol. 35, no. 3, pp. 539–542, Mar. 1964.
- [55] A. Cingolani, M. Ferrara, and M. Lugarà, "Dispersion of the linear electrooptic coefficient and of the non-linear susceptibility in ZnTe," *Solid State Commun.*, vol. 38, no. 9, pp. 819–821, Jun. 1981.
- [56] A. Gerrard and J. Burch, *Introduction to Matrix Methods in Optics*. Wiley, 1975.
- [57] G. Gallot, J. Zhang, R. W. McGowan, T.-I. Jeon, and D. Grischkowsky, "Measurements of the THz absorption and dispersion of ZnTe and their relevance to the electro-optic detection of THz radiation," *Appl. Phys. Lett.*, vol. 74, no. 23, pp. 3450–3452, Jun. 1999.
- [58] D. Turchinovich, "Study of ultrafast polarization and carrier dynamics in semiconductor nanostructures : a THz spectroscopy approach," The University of Freiburg, 2004.
- [59] P. U. Jepsen, D. G. Cooke, and M. Koch, "Terahertz spectroscopy and imaging - Modern techniques and applications," *Laser Photon. Rev.*, vol. 5, no. 1, pp. 124–166, Jan. 2011.
- [60] P. Kattan, *MATLAB for Beginners: A Gentle Approach*. Lulu Press, 2008.
- [61] S. Hassani, *Mathematical Methods Using Mathematica®*. New York, NY: Springer New York, 2003.
- [62] R. E. Glover and M. Tinkham, "Conductivity of Superconducting Films for Photon Energies between 0.3 and 40kTc," *Phys. Rev.*, vol. 108, no. 2, pp. 243–256, Oct. 1957.

- [63] K. P. H. Lui and F. A. Hegmann, "Ultrafast carrier relaxation in radiation-damaged silicon on sapphire studied by optical-pump–terahertz-probe experiments," *Appl. Phys. Lett.*, vol. 78, no. 22, pp. 3478–3480, May 2001.
- [64] F. Wang, J. Shan, M. A. Islam, I. P. Herman, M. Bonn, and T. F. Heinz, "Exciton polarizability in semiconductor nanocrystals," *Nat. Mater.*, vol. 5, no. 11, pp. 861–864, Nov. 2006.
- [65] G. Jnawali, Y. Rao, H. Yan, and T. F. Heinz, "Observation of a transient decrease in terahertz conductivity of single-layer graphene induced by ultrafast optical excitation," *Nano Lett.*, vol. 13, no. 2, pp. 524–30, Feb. 2013.
- [66] S. A. Jensen *et al.*, "Ultrafast photoconductivity of graphene nanoribbons and carbon nanotubes," *Nano Lett.*, vol. 13, no. 12, pp. 5925–5930, Dec. 2013.
- [67] S. A. Jensen *et al.*, "Competing ultrafast energy relaxation pathways in photoexcited graphene," *Nano Lett.*, vol. 14, no. 10, pp. 5839–45, Oct. 2014.
- [68] Z. Mics *et al.*, "Thermodynamic picture of ultrafast charge transport in graphene," *Nat. Commun.*, vol. 6, no. May, p. 7655, Jul. 2015.
- [69] I. Ivanov, M. Bonn, Z. Mics, and D. Turchinovich, "Perspective on terahertz spectroscopy of graphene," *EPL (Europhysics Lett.)*, vol. 111, no. 6, p. 67001, Sep. 2015.
- [70] M. H. Gass, U. Bangert, A. L. Bleloch, P. Wang, R. R. Nair, and A. K. Geim, "Free-standing graphene at atomic resolution," *Nat. Nanotechnol.*, vol. 3, no. 11, pp. 676–681, Nov. 2008.
- [71] C. Berger *et al.*, "Ultrathin Epitaxial Graphite: 2D Electron Gas Properties and a Route toward Graphene-based Nanoelectronics," *J. Phys. Chem. B*, vol. 108, no. 52, pp. 19912–19916, Dec. 2004.
- [72] F. Varchon *et al.*, "Electronic Structure of Epitaxial Graphene Layers on SiC: Effect of the Substrate," *Phys. Rev. Lett.*, vol. 99, no. 12, p. 126805, Sep. 2007.
- [73] X. Li *et al.*, "Large-Area Synthesis of High-Quality and Uniform Graphene Films on Copper Foils," *Science (80-.)*, vol. 324, no. 5932, pp. 1312–1314, Jun. 2009.
- [74] C. J. Docherty *et al.*, "Extreme sensitivity of graphene photoconductivity to

- environmental gases,” *Nat. Commun.*, vol. 3, p. 1228, Jan. 2012.
- [75] H. I. Wang *et al.*, “Reversible Photochemical Control of Doping Levels in Supported Graphene,” *J. Phys. Chem. C*, vol. 121, no. 7, pp. 4083–4091, Feb. 2017.
- [76] J. L. Tomaino *et al.*, “Terahertz imaging and spectroscopy of large-area single-layer graphene,” *Opt. Express*, vol. 19, no. 1, p. 141, Jan. 2011.
- [77] I. Maeng, S. Lim, S. J. Chae, Y. H. Lee, H. Choi, and J.-H. Son, “Gate-controlled nonlinear conductivity of Dirac fermion in graphene field-effect transistors measured by terahertz time-domain spectroscopy,” *Nano Lett.*, vol. 12, no. 2, pp. 551–5, Feb. 2012.
- [78] L. Ren *et al.*, “Terahertz and Infrared Spectroscopy of Gated Large-Area Graphene,” *Nano Lett.*, vol. 12, no. 7, pp. 3711–3715, Jul. 2012.
- [79] A. J. Frenzel *et al.*, “Observation of suppressed terahertz absorption in photoexcited graphene,” *Appl. Phys. Lett.*, vol. 102, no. 11, p. 113111, 2013.
- [80] J. N. Heyman, J. D. Stein, Z. S. Kaminski, A. R. Banman, A. M. Massari, and J. T. Robinson, “Carrier heating and negative photoconductivity in graphene,” *J. Appl. Phys.*, vol. 117, no. 1, p. 015101, Jan. 2015.
- [81] J. D. Buron *et al.*, “Electrically Continuous Graphene from Single Crystal Copper Verified by Terahertz Conductance Spectroscopy and Micro Four-Point Probe,” *Nano Lett.*, vol. 14, no. 11, pp. 6348–6355, Nov. 2014.
- [82] J. Hebling, G. Almasi, I. Kozma, and J. Kuhl, “Velocity matching by pulse front tilting for large area THz-pulse generation,” *Opt. Express*, vol. 10, no. 21, p. 1161, Oct. 2002.
- [83] M. C. Hoffmann and J. A. Fülöp, “Intense ultrashort terahertz pulses: generation and applications,” *J. Phys. D. Appl. Phys.*, vol. 44, no. 8, p. 083001, Mar. 2011.
- [84] H. Y. Hwang, N. C. Brandt, H. Farhat, A. L. Hsu, J. Kong, and K. A. Nelson, “Nonlinear THz Conductivity Dynamics in P-Type CVD-Grown Graphene,” *J. Phys. Chem. B*, vol. 117, no. 49, pp. 15819–15824, Dec. 2013.
- [85] M. J. Paul *et al.*, “High-field terahertz response of graphene,” *New J. Phys.*, vol. 15, no. 8, p. 085019, Aug. 2013.

- [86] H. A. Hafez *et al.*, “Nonlinear terahertz field-induced carrier dynamics in photoexcited epitaxial monolayer graphene,” *Phys. Rev. B*, vol. 91, no. 3, p. 035422, 2015.
- [87] M. C. Hoffmann and D. Turchinovich, “Semiconductor saturable absorbers for ultrafast terahertz signals,” *Appl. Phys. Lett.*, vol. 96, no. 15, p. 151110, Apr. 2010.
- [88] D. Turchinovich, J. M. Hvam, and M. C. Hoffmann, “Self-phase modulation of a single-cycle terahertz pulse by nonlinear free-carrier response in a semiconductor,” *Phys. Rev. B*, vol. 85, no. 20, p. 201304, May 2012.
- [89] S. Tani, F. Blanchard, and K. Tanaka, “Ultrafast carrier dynamics in graphene under a high electric field,” *Phys. Rev. Lett.*, vol. 109, no. 16, p. 166603, Oct. 2012.
- [90] V. N. Kotov, B. Uchoa, V. M. Pereira, F. Guinea, and a. H. Castro Neto, “Electron-electron interactions in graphene: Current status and perspectives,” *Rev. Mod. Phys.*, vol. 84, no. 3, pp. 1067–1125, 2012.
- [91] M. Breusing *et al.*, “Ultrafast nonequilibrium carrier dynamics in a single graphene layer,” *Phys. Rev. B*, vol. 83, no. 15, p. 153410, Apr. 2011.
- [92] I. Gierz *et al.*, “Snapshots of non-equilibrium Dirac carrier distributions in graphene,” *Nat. Mater.*, vol. 12, no. 12, pp. 1119–1124, Dec. 2013.
- [93] J. C. Johannsen *et al.*, “Direct view of hot carrier dynamics in graphene,” *Phys. Rev. Lett.*, vol. 111, no. 2, p. 027403, Jul. 2013.
- [94] K. J. Tielrooij *et al.*, “Photoexcitation cascade and multiple hot-carrier generation in graphene,” *Nat. Phys.*, vol. 9, no. 4, pp. 248–252, Feb. 2013.
- [95] X. Liu, J. Laegsgaard, and D. Turchinovich, “Self-stabilization of a mode-locked femtosecond fiber laser using a photonic bandgap fiber,” *Opt. Lett.*, vol. 35, no. 7, pp. 913–5, Apr. 2010.
- [96] S. F. Shi *et al.*, “Controlling graphene ultrafast hot carrier response from metal-like to semiconductor-like by electrostatic gating,” *Nano Lett.*, vol. 14, no. 3, pp. 1578–1582, Mar. 2014.
- [97] J. C. W. Song, K. J. Tielrooij, F. H. L. Koppens, and L. S. Levitov, “Photoexcited carrier dynamics and impact-excitation cascade in graphene,” *Phys. Rev. B*, vol. 87,

- no. 15, p. 155429, Apr. 2013.
- [98] T. Ando, "Screening effect and impurity scattering in monolayer graphene," *J. Phys. Soc. Japan*, vol. 75, no. 7, p. 074716, Jul. 2006.
- [99] H. Yan *et al.*, "Infrared Spectroscopy of Wafer-Scale Graphene," *ACS Nano*, vol. 5, no. 12, pp. 9854–9860, Dec. 2011.
- [100] C. H. Lui, K. F. Mak, J. Shan, and T. F. Heinz, "Ultrafast Photoluminescence from Graphene," *Phys. Rev. Lett.*, vol. 105, no. 12, p. 127404, Sep. 2010.
- [101] J. C. W. Song, M. Y. Reizer, and L. S. Levitov, "Disorder-Assisted Electron-Phonon Scattering and Cooling Pathways in Graphene," *Phys. Rev. Lett.*, vol. 109, no. 10, p. 106602, Sep. 2012.
- [102] A. C. Betz *et al.*, "Supercollision cooling in undoped graphene," *Nat. Phys.*, vol. 9, no. 2, pp. 109–112, Feb. 2013.
- [103] M. W. Graham, S.-F. Shi, D. C. Ralph, J. Park, and P. L. McEuen, "Photocurrent measurements of supercollision cooling in graphene," *Nat. Phys.*, vol. 9, no. 2, pp. 103–108, Feb. 2013.
- [104] M. Freitag, T. Low, and P. Avouris, "Increased Responsivity of Suspended Graphene Photodetectors," *Nano Lett.*, vol. 13, no. 4, pp. 1644–1648, Apr. 2013.
- [105] T. Hallam *et al.*, "Controlled Folding of Graphene: GraFold Printing," *Nano Lett.*, vol. 15, no. 2, pp. 857–863, Feb. 2015.
- [106] A. Fasolino, J. H. Los, and M. I. Katsnelson, "Intrinsic ripples in graphene," *Nat. Mater.*, vol. 6, no. 11, pp. 858–861, Nov. 2007.
- [107] N. Liu, Z. Pan, L. Fu, C. Zhang, B. Dai, and Z. Liu, "The origin of wrinkles on transferred graphene," *Nano Res.*, vol. 4, no. 10, pp. 996–1004, Oct. 2011.
- [108] N. Levy *et al.*, "Strain-Induced Pseudo-Magnetic Fields Greater Than 300 Tesla in Graphene Nanobubbles," *Science (80-.)*, vol. 329, no. 5991, pp. 544–547, Jul. 2010.
- [109] N. Abedpour, R. Asgari, and F. Guinea, "Strains and pseudomagnetic fields in circular graphene rings," *Phys. Rev. B*, vol. 84, no. 11, p. 115437, Sep. 2011.
- [110] Q. Wu *et al.*, "Selective surface functionalization at regions of high local curvature in

- graphene,” *Chem. Commun.*, vol. 49, no. 7, pp. 677–679, 2013.
- [111] J. T. Rasmussen, T. Gunst, P. Bøggild, A.-P. Jauho, and M. Brandbyge, “Electronic and transport properties of kinked graphene,” *Beilstein J. Nanotechnol.*, vol. 4, pp. 103–110, Feb. 2013.
- [112] C. J. Docherty and M. B. Johnston, “Terahertz Properties of Graphene,” *J. Infrared, Millimeter, Terahertz Waves*, vol. 33, no. 8, pp. 797–815, Jun. 2012.
- [113] S. Bae *et al.*, “Roll-to-roll production of 30-inch graphene films for transparent electrodes,” *Nat. Nanotechnol.*, vol. 5, no. 8, pp. 574–578, Aug. 2010.
- [114] X. Li *et al.*, “Transfer of Large-Area Graphene Films for High-Performance Transparent Conductive Electrodes,” *Nano Lett.*, vol. 9, no. 12, pp. 4359–4363, Dec. 2009.
- [115] P. Blake *et al.*, “Making graphene visible,” *Appl. Phys. Lett.*, vol. 91, no. 6, p. 063124, Aug. 2007.
- [116] T. Hallam, M. T. Cole, W. I. Milne, and G. S. Duesberg, “Field emission characteristics of contact printed graphene fins,” *Small*, vol. 10, no. 1, pp. 95–99, Jan. 2014.
- [117] T. Hallam, N. C. Berner, C. Yim, and G. S. Duesberg, “Strain, Bubbles, Dirt, and Folds: A Study of Graphene Polymer-Assisted Transfer,” *Adv. Mater. Interfaces*, vol. 1, no. 6, p. 1400115, Sep. 2014.
- [118] D. E. Jesson and S. J. Pennycook, “Incoherent Imaging of Crystals Using Thermally Scattered Electrons,” *Proc. R. Soc. A Math. Phys. Eng. Sci.*, vol. 449, no. 1936, pp. 273–293, May 1995.
- [119] S. J. Haigh *et al.*, “Cross-sectional imaging of individual layers and buried interfaces of graphene-based heterostructures and superlattices,” *Nat. Mater.*, vol. 11, no. 9, pp. 764–767, Sep. 2012.
- [120] T. M. G. Mohiuddin *et al.*, “Uniaxial strain in graphene by Raman spectroscopy: G peak splitting, Grüneisen parameters, and sample orientation,” *Phys. Rev. B*, vol. 79, no. 20, p. 205433, May 2009.
- [121] J. E. Lee, G. Ahn, J. Shim, Y. S. Lee, and S. Ryu, “Optical separation of mechanical

- strain from charge doping in graphene,” *Nat. Commun.*, vol. 3, no. 1, p. 1024, Jan. 2012.
- [122] M. Mohr, K. Papagelis, J. Maultzsch, and C. Thomsen, “Two-dimensional electronic and vibrational band structure of uniaxially strained graphene from ab initio calculations,” *Phys. Rev. B*, vol. 80, no. 20, p. 205410, Nov. 2009.
- [123] J. Stadler, T. Schmid, and R. Zenobi, “Nanoscale Chemical Imaging Using Top-Illumination Tip-Enhanced Raman Spectroscopy,” *Nano Lett.*, vol. 10, no. 11, pp. 4514–4520, Nov. 2010.
- [124] A. Hartschuh, “Tip-Enhanced Near-Field Optical Microscopy,” *Angew. Chemie Int. Ed.*, vol. 47, no. 43, pp. 8178–8191, Oct. 2008.
- [125] S. Berciaud, S. Ryu, L. E. Brus, and T. F. Heinz, “Probing the Intrinsic Properties of Exfoliated Graphene: Raman Spectroscopy of Free-Standing Monolayers,” *Nano Lett.*, vol. 9, no. 1, pp. 346–352, Jan. 2009.
- [126] S. Ryu *et al.*, “Atmospheric Oxygen Binding and Hole Doping in Deformed Graphene on a SiO₂ Substrate,” *Nano Lett.*, vol. 10, no. 12, pp. 4944–4951, Dec. 2010.
- [127] M. B. B. S. Larsen, D. M. A. Mackenzie, J. M. Caridad, P. Bøggild, and T. J. Booth, “Transfer induced compressive strain in graphene: Evidence from Raman spectroscopic mapping,” *Microelectron. Eng.*, vol. 121, pp. 113–117, Jun. 2014.
- [128] K. J. Tielrooij *et al.*, “Photoexcitation cascade and multiple hot-carrier generation in graphene,” *Nat. Phys.*, vol. 9, no. 4, pp. 248–252, Feb. 2013.
- [129] I. Ivanov *et al.*, “Role of Edge Engineering in Photoconductivity of Graphene Nanoribbons,” *J. Am. Chem. Soc.*, vol. 139, no. 23, pp. 7982–7988, Jun. 2017.
- [130] W. Xu and T.-W. Lee, “Recent progress in fabrication techniques of graphene nanoribbons,” *Mater. Horizons*, vol. 3, no. 3, pp. 186–207, 2016.
- [131] X. Li, X. Wang, L. Zhang, S. Lee, and H. Dai, “Chemically Derived, Ultrasoft Graphene Nanoribbon Semiconductors,” *Science (80-.)*, vol. 319, no. 5867, pp. 1229–1232, Feb. 2008.
- [132] A. Sinitskii, A. A. Fursina, D. V. Kosynkin, A. L. Higginbotham, D. Natelson, and J.

- M. Tour, "Electronic transport in monolayer graphene nanoribbons produced by chemical unzipping of carbon nanotubes," *Appl. Phys. Lett.*, vol. 95, no. 25, p. 253108, Dec. 2009.
- [133] D. V. Kosynkin, W. Lu, A. Sinitskii, G. Pera, Z. Sun, and J. M. Tour, "Highly Conductive Graphene Nanoribbons by Longitudinal Splitting of Carbon Nanotubes Using Potassium Vapor," *ACS Nano*, vol. 5, no. 2, pp. 968–974, Feb. 2011.
- [134] Z. Chen, Y.-M. Lin, M. J. Rooks, and P. Avouris, "Graphene nano-ribbon electronics," *Phys. E Low-dimensional Syst. Nanostructures*, vol. 40, no. 2, pp. 228–232, Dec. 2007.
- [135] P. B. Bennett *et al.*, "Bottom-up graphene nanoribbon field-effect transistors," *Appl. Phys. Lett.*, vol. 103, no. 25, p. 253114, Dec. 2013.
- [136] J. P. Llinas *et al.*, "Short-channel field-effect transistors with 9-atom and 13-atom wide graphene nanoribbons," *Nat. Commun.*, vol. 8, no. 1, p. 633, Dec. 2017.
- [137] A. Celis *et al.*, "Graphene nanoribbons: fabrication, properties and devices," *J. Phys. D. Appl. Phys.*, vol. 49, no. 14, p. 143001, Apr. 2016.
- [138] J. Lloyd-Hughes and T. I. Jeon, "A review of the terahertz conductivity of bulk and nano-materials," *Journal of Infrared, Millimeter, and Terahertz Waves*, vol. 33, no. 9, pp. 871–925, 31-May-2012.
- [139] S. Osella *et al.*, "Graphene Nanoribbons as Low Band Gap Donor Materials for Organic Photovoltaics: Quantum Chemical Aided Design," *ACS Nano*, vol. 6, no. 6, pp. 5539–5548, Jun. 2012.
- [140] G. Soavi *et al.*, "Exciton–exciton annihilation and biexciton stimulated emission in graphene nanoribbons," *Nat. Commun.*, vol. 7, no. 1, p. 11010, Apr. 2016.
- [141] F. C. Whitmore, "THE COMMON BASIS OF INTRAMOLECULAR REARRANGEMENTS I," *J. Am. Chem. Soc.*, vol. 54, no. 8, pp. 3274–3283, Aug. 1932.
- [142] M. Kastler, W. Pisula, D. Wasserfallen, T. Pakula, and K. Müllen, "Influence of Alkyl Substituents on the Solution- and Surface-Organization of Hexa- p eri - hexabenzocoronenes," *J. Am. Chem. Soc.*, vol. 127, no. 12, pp. 4286–4296, Mar. 2005.

- [143] Y. Hu *et al.*, “Bandgap Engineering of Graphene Nanoribbons by Control over Structural Distortion,” *J. Am. Chem. Soc.*, vol. 140, no. 25, pp. 7803–7809, Jun. 2018.
- [144] E. Hendry, J. M. Schins, L. P. Candeias, L. D. A. Siebbeles, and M. Bonn, “Efficiency of Exciton and Charge Carrier Photogeneration in a Semiconducting Polymer,” *Phys. Rev. Lett.*, vol. 92, no. 19, p. 196601, May 2004.
- [145] A. Hangleiter *et al.*, “Efficient formation of excitons in a dense electron-hole plasma at room temperature,” *Phys. Rev. B*, vol. 92, no. 24, p. 241305, Dec. 2015.
- [146] Z. Jin *et al.*, “Ultrafast Terahertz Photoconductivity of Photovoltaic Polymer–Fullerene Blends: A Comparative Study Correlated with Photovoltaic Device Performance,” *J. Phys. Chem. Lett.*, vol. 5, no. 21, pp. 3662–3668, Nov. 2014.
- [147] J. Heyd, G. E. Scuseria, and M. Ernzerhof, “Hybrid functionals based on a screened Coulomb potential,” *J. Chem. Phys.*, vol. 118, no. 18, pp. 8207–8215, May 2003.
- [148] E. Clar, *Polycyclic Hydrocarbons*. Berlin, Heidelberg: Springer Berlin Heidelberg, 1964.
- [149] E. Clar, *The Aromatic Sextet*. London, New York, Sydney, Toronto: John Wiley & Sons, 1972.
- [150] J. Wu, W. Pisula, and K. Müllen, “Graphenes as Potential Material for Electronics,” *Chem. Rev.*, vol. 107, no. 3, pp. 718–747, Mar. 2007.
- [151] M. D. Watson, A. Fechtenkötter, and K. Müllen, “Big Is Beautiful—‘Aromaticity’ Revisited from the Viewpoint of Macromolecular and Supramolecular Benzene Chemistry,” *Chem. Rev.*, vol. 101, no. 5, pp. 1267–1300, May 2001.
- [152] T. Wassmann, A. P. Seitsonen, A. M. Saitta, M. Lazzeri, and F. Mauri, “Structure, Stability, Edge States, and Aromaticity of Graphene Ribbons,” *Phys. Rev. Lett.*, vol. 101, no. 9, p. 096402, Aug. 2008.
- [153] T. Wassmann, A. P. Seitsonen, A. M. Saitta, M. Lazzeri, and F. Mauri, “Clar’s Theory, π -Electron Distribution, and Geometry of Graphene Nanoribbons,” *J. Am. Chem. Soc.*, vol. 132, no. 10, pp. 3440–3451, Mar. 2010.
- [154] L. Chen, L. Wang, and D. Beljonne, “Designing coved graphene nanoribbons with charge carrier mobility approaching that of graphene,” *Carbon N. Y.*, vol. 77, pp.

- 868–879, Oct. 2014.
- [155] V. Perebeinos, J. Tersoff, and P. Avouris, “Electron-Phonon Interaction and Transport in Semiconducting Carbon Nanotubes,” *Phys. Rev. Lett.*, vol. 94, no. 8, p. 086802, Mar. 2005.
- [156] M.-Q. Long, L. Tang, D. Wang, L. Wang, and Z. Shuai, “Theoretical Predictions of Size-Dependent Carrier Mobility and Polarity in Graphene,” *J. Am. Chem. Soc.*, vol. 131, no. 49, pp. 17728–17729, Dec. 2009.
- [157] J. Bardeen and W. Shockley, “Deformation Potentials and Mobilities in Non-Polar Crystals,” *Phys. Rev.*, vol. 80, no. 1, pp. 72–80, Oct. 1950.
- [158] Z. Shuai, L. Wang, and Q. Li, “Evaluation of Charge Mobility in Organic Materials: From Localized to Delocalized Descriptions at a First-Principles Level,” *Adv. Mater.*, vol. 23, no. 9, pp. 1145–1153, Mar. 2011.
- [159] H. Xu and T. Heinzl, “Impurity and edge roughness scattering in graphene nanoribbons: the Boltzmann approach,” *J. Phys. Condens. Matter*, vol. 24, no. 45, p. 455303, Nov. 2012.
- [160] V. K. Dugaev and M. I. Katsnelson, “Edge scattering of electrons in graphene: Boltzmann equation approach to the transport in graphene nanoribbons and nanodisks,” *Phys. Rev. B*, vol. 88, no. 23, p. 235432, Dec. 2013.
- [161] H. Němec, P. Kužel, and V. Sundström, “Far-infrared response of free charge carriers localized in semiconductor nanoparticles,” *Phys. Rev. B*, vol. 79, no. 11, p. 115309, Mar. 2009.
- [162] L. Yu, A. Ruzsinszky, and J. P. Perdew, “Bending Two-Dimensional Materials To Control Charge Localization and Fermi-Level Shift,” *Nano Lett.*, vol. 16, no. 4, pp. 2444–2449, Apr. 2016.
- [163] M. Slota *et al.*, “Magnetic edge states and coherent manipulation of graphene nanoribbons,” *Nature*, vol. 557, no. 7707, pp. 691–695, May 2018.
- [164] J. Cai *et al.*, “Atomically precise bottom-up fabrication of graphene nanoribbons,” *Nature*, vol. 466, no. 7305, pp. 470–473, Jul. 2010.
- [165] S. Gyungseon *et al.*, “CNTbands.” 2006.

- [166] L. Yang, M. P. Anantram, J. Han, and J. P. Lu, “Band-gap change of carbon nanotubes: Effect of small uniaxial and torsional strain,” *Phys. Rev. B*, vol. 60, no. 19, pp. 13874–13878, Nov. 1999.

Acknowledgments

I would like first and foremost to thank my research supervisor, Professor Dmitry Turchinovich, for the provided opportunity to make this work happen.

Great thanks to the director of Molecular Spectroscopy Department in Max Planck Institute of Polymer Research in Mainz, Professor Mischa Bonn, for the constant support and providing with such a beautiful workspace and atmosphere that reigns at the department.

I am also greatly thankful to Søren Jensen, Zoltán Mics, Wang Hai, Francesco D'Angelo and Klaas-Jan Tielrooij for invaluable knowledge and experience they have shared with me during my PhD. All the optics and spectroscopy I know now I have picked up from these great people.

This work would be impossible without samples, that I was happy to work on. I want to thank for that all the people from the department of Professor Klaus Müllen who have provided me with the graphene and graphene nanoribbons samples. In particular, I am grateful to Akimitsu Narita, and his brilliant coworkers who can create magnificent things with chemistry, they are genuinely wizards in my eyes. It was a real pleasure to work with Yunbin Hu, Daniel Jänsch and Uliana Beser.

I also would like to express my gratitude to people from Trinity College Dublin for providing us with their interesting graphene samples. My thanks go to Toby Hallam and Prof. Georg S. Duesberg.

I want to express my gratitude to my dear officemates that made my time in MPIP so delightful and genuinely fun. I thank Keno Krewer for giving the priceless feedback and critical opinions on every silly question I dared him to ask. I want to express my sincere gratitude to Hassan Hafez for bringing his inherent positiveness to my work besides his very insightful and helpful tips here and there. My thanks go to Maksim Grechko for those great talks about physics and spectroscopy from which I learned a lot, or at least I think I learned, that was great. I thank Marc-Jan van Zadel, Jonas Pfisterer, Jenée Cyran and Leonie Driessen for those long conversations we had on every possible topic. Thanks to Simon Bretschneider, Marco Ballabio, Eduard Unger, Yujen Wang and Kevin Machel for the awesome time outside the work and for your interest in the culture of my motherland that was the source of the countless amount of jokes we together laughed at.

Special thanks go of course to the secretary of Prof. Mischa Bonn, Laurie Gangloff who was and is our guardian angel at the department. I thank her for all the help she gave me in hard times. I cannot find all the words to express how thankful am I.

I thank my wife for the patience and support during this time.

Publications List

S. A. Jensen, Z. Mics, **I. Ivanov**, H. S. Varol, D. Turchinovich, F. H. L. Koppens, M. Bonn, and K. J. Tielrooij, *Competing ultrafast energy relaxation pathways in photoexcited graphene*, Nano Lett., vol. 14, no. 10, pp. 5839–45, Oct. 2014.

T. Hallam, A. Shakouri, E. Poliani, A. P. Rooney, **I. Ivanov**, A. Potie, H. K. Taylor, M. Bonn, D. Turchinovich, S. J. Haigh, J. Maultzsch, and G. S. Duesberg, *Controlled Folding of Graphene: GraFold Printing*, Nano Lett., vol. 15, no. 2, pp. 857–863, Feb. 2015.

Z. Mics, K.-J. Tielrooij, K. Parvez, S. A. Jensen, **I. Ivanov**, X. Feng, K. Müllen, M. Bonn, and D. Turchinovich, *Thermodynamic picture of ultrafast charge transport in graphene*, Nat. Commun., vol. 6, no. May, p. 7655, Jul. 2015.

I. Ivanov, M. Bonn, Z. Mics, and D. Turchinovich, *Perspective on terahertz spectroscopy of graphene*, EPL Europhysics Lett., vol. 111, no. 6, p. 67001, Sep. 2015.

I. Ivanov, Y. Hu, S. Osella, U. Beser, H. I. Wang, D. Beljonne, A. Narita, K. Müllen, D. Turchinovich, and M. Bonn, *Role of Edge Engineering in Photoconductivity of Graphene Nanoribbons*, J. Am. Chem. Soc., vol. 139, no. 23, pp. 7982–7988, Jun. 2017.

Publications that are not featured in this thesis:

Z. Chen, H. I. Wang, J. Teyssandier, K. S. Mali, T. Dumsloff, **I. Ivanov**, W. Zhang, P. Ruffieux, R. Fasel, H. J. Roder, D. Turchinovich, S. De Feyter, X. Feng, M. Klui, A. Narita, M. Bonn, and K. Müllen, *Chemical Vapor Deposition Synthesis and Terahertz Photoconductivity of Low-Band-Gap $N = 9$ Armchair Graphene Nanoribbons*, J. Am. Chem. Soc., vol. 139, no. 10, pp. 3635–3638, Mar. 2017.

D. Jansch, **I. Ivanov**, Y. Zagryarski, I. Duznovic, M. Baumgarten, D. Turchinovich, C. Li, M. Bonn, and K. Müllen, *Ultra-Narrow Low-Bandgap Graphene Nanoribbons from Bromoperylene-Synthesis and Terahertz-Spectroscopy*, Chem. - A Eur. J., vol. 23, no. 20, pp. 4870–4875, Apr. 2017.

S. A. Bretschneider, **I. Ivanov**, H. I. Wang, K. Miyata, X. Zhu, and M. Bonn, *Quantifying Polaron Formation and Charge Carrier Cooling in Lead-Iodide Perovskites*, Adv. Mater., p. 1707312, May 2018.

Curriculum Vitae

- 21.06.1986 born in Chekhov, Russia
- 1992 – 1997 Comprehensive school of Novyy Byt township, Novyy Byt township, Russia
- 1997 – 1999 Comprehensive school n.8, Chekhov, Russia
- 1999 – 2003 Lyceum n.4, Chekhov, Russia
- 2003 – 2009 Diploma in Physics, Moscow Engineering Physics Institute, Moscow, Russia
- 2009 – 2010 System Programmer, Federal State Unitary Enterprise Research Institute of
Operating Systems, Moscow, Russia
- 2010 – 2013 Junior Researcher, Federal State Unitary Enterprise All-Russia Research
Institute of Automatics, Moscow, Russia
- since 2013 Doctorate, Max Planck Institute for Polymer Research, Mainz, Germany

